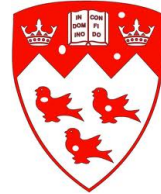


Towards optimal whispering gallery mode microcavity sensors: Novel techniques and analyses

Muhammad Imran Cheema



Department of Electrical & Computer Engineering
McGill University
Montreal, Canada

October 2013

A thesis submitted to McGill University in partial fulfillment of the requirements for the
degree of Doctor of Philosophy.

© 2013 Muhammad Imran Cheema

Abstract

The last two decades have seen tremendous progress towards the development of real time, label free and sensitive optical sensors. Researchers have demonstrated numerous techniques based on surface plasmon resonance, interferometers, waveguides, microcavities, optical fibers and photonic crystals. Among these different approaches, the large photon lifetime (quality factor of $10^6 - 10^9$) of whispering gallery mode (WGM) microcavities makes them a strong candidate for ultrasensitive sensing, as the circulating photons sample a sensing event many times. In a microcavity sensor, the sensing event can be correlated to various measurement parameters including the resonant wavelength and the quality factor. A variety of approaches have been introduced to measure these parameters but little attention has been previously paid to improve the overall signal to noise ratio or accuracy of the sensor.

The existing approaches suffer from various drawbacks; some of them do not allow for real time measurement, and their signal (change in the cavity parameters in response to the sensing event) is limited by many noise sources such as laser intensity noise and wavelength instability. Moreover, it is often assumed in the literature that optimum sensing performance is obtained by operating a microcavity at its highest possible quality factor. However, this does not consider the impact of the quality factor on the signal to noise ratio of the sensor. Finally, previous investigations have not explored the opportunity to combine measurements of two different microcavity parameters (i.e. resonant wavelength and quality factor) in order to obtain a more accurate estimation of a sensing event.

In this thesis our goal is to develop techniques and analyses towards optimal performance of WGM microcavity sensors. To achieve this goal, firstly, we demonstrate a novel measurement approach for the microcavity sensors based upon phase shift-cavity ring down spectroscopy. We show that it is possible to simultaneously measure the resonant wavelength and the quality factor of a microcavity as a function of the sensing event, in real time and with high noise immunity. Secondly, we develop an accurate electromagnetic model to calculate the resonant wavelength and the quality factor for any axisymmetric microcavity geometry. The model is utilized to determine the microcavity parameters for obtaining the maximum signal of the sensor. Thirdly, we conduct a comprehensive noise analysis for those microcavity sensors that measure changes in the resonant wavelength and the quality factor to probe a sensing event. The signal and noise analysis shows that

there is an optimal size and quality factor for a microcavity at which the maximum signal to noise ratio (SNR) is obtained, and that a highest quality factor may not result in the highest SNR. Finally, we develop a model and demonstrate that a combination of the resonant wavelength and the quality factor measurements of a microcavity sensor provide a more accurate sensing approach. The model is also extended to develop a sensing metric to compare the performance of wide range of sensors.

Significantly, except for the electromagnetic model which applies to any axisymmetric WGM microcavity, all the techniques and the analyses developed in this thesis are independent of the WGM microcavity geometry. Moreover, the electromagnetic model, the signal and the noise analysis, and the work on combining the multiple sensing parameters are also applicable to the previously demonstrated approaches. Furthermore, the current work is relevant to various sensing applications, ranging from liquid to gaseous phase. We believe that the present thesis is a step forward towards optimal performance for WGM microcavity sensors.

Sommaire

Des progrès importants ont été observés les deux dernières décennies sur le développement de capteurs optiques sans étiquette, sensible et en temps réel. Les chercheurs ont démontré plusieurs techniques basées sur la résonance plasmonique de surface, les interféromètres, les guides d'ondes, les microcavités, la fibre optique and les cristaux photoniques. Parmi ces différentes approches, la longue durée de vie du photon (facteur de qualité de $10^6 - 10^9$) des microcavités en mode de chuchotement en galerie (WGM) font de celles-ci d'excellentes candidates pour la détection ultrasensible puisque les photons circulant dans la cavité échantillonnent le même évènement plusieurs fois. Dans un capteur à microcavité, l'évènement de détection peut être corrélé à plusieurs paramètres de mesures incluant la longueur d'onde de résonance et le facteur de qualité. Des approches variées ont été présentées pour mesurer ces paramètres mais l'amélioration du rapport signal sur bruit et la précision des capteurs ont peu d'attention jusqu'à maintenant.

Les approches existantes possèdent plusieurs inconvénients; certaines ne permettent pas de mesures en temps réel et leur signal (changement des paramètres de la cavité en réponse à l'évènement de détection) est limité par les multiples sources de bruit tels que l'intensité et l'instabilité de la longueur d'onde du laser. De plus, il n'a jamais été démontré que l'information à propos d'un évènement de détection puisse être déterminée plus précisément en utilisant une combinaison des multiples paramètres d'une microcavité, tels que la longueur d'onde de résonance et le facteur de qualité. En outre, il est souvent pris pour acquis dans la littérature que la performance optimale de détection est obtenue en opérant une microcavité à son facteur de qualité le plus élevé. Cependant, cette démarche ne prend pas compte de l'impact du facteur de qualité sur le rapport signal sur bruit du capteur.

Dans cette thèse, notre objectif est de développer des techniques et des analyses pour une performance optimale des capteurs à microcavité WGM. Pour atteindre cet objectif, nous démontrons tout d'abord une nouvelle approche de mesure pour les capteurs basés sur la spectroscopie d'absorption par déphasage et mesure du temps de vie des photons piégés dans une cavité optique. Nous démontrons qu'il est possible de mesurer simultanément la longueur d'onde de résonance et le facteur de qualité de la microcavité en fonction de l'évènement de détection, en temps réel et avec une grande immunité au bruit. Deuximement, nous développons un modle électromagnétique précis pour calculer la longueur d'onde

de résonance et le facteur de qualité pour toutes les géométries asymétriques des microcavités. Le modèle est utilisé pour déterminer les paramètres de la microcavité afin d'obtenir un signal maximum avec le capteur. Troisièmement, nous effectuons une analyse compréhensive du bruit pour les capteurs à microcavité qui mesurent les changements dans la longueur d'onde de résonance et le facteur de qualité pour la détection. L'analyse du signal et du bruit démontre qu'il y a une dimension optimale et un facteur de qualité pour lesquels un rapport signal sur bruit (SNR) maximum est obtenu, et qu'un facteur de qualité plus élevé ne donne pas nécessairement un SNR plus élevé. Finalement, nous développons un modèle et démontrons qu'une combinaison de la mesure de la longueur d'onde de résonance et du facteur de qualité d'un capteur par microcavité fournit une détection plus précise. De plus, le modèle est étendu afin de développer un paramètre de détection pour comparer la performance de plusieurs capteurs.

À l'exception du modèle électromagnétique qui s'applique à toutes les microcavités WGM asymétriques, toutes les techniques et analyses développées dans cette thèse sont indépendantes de la géométrie de la microcavité WGM. De plus, le modèle électromagnétique, l'analyse du signal et du bruit et les démonstrations sur la combinaison de multiples paramètres de détection s'appliquent aussi aux autres approches démontrées précédemment. En outre, la démarche présentée est appropriée pour plusieurs modes de détection, allant de la phase liquide à gazeuse. Nous croyons que la présente thèse est un pas de plus vers une performance optimale des capteurs à microcavité WGM.

Acknowledgements

First of all I am thankful to the God almighty who has given me the abilities to produce this thesis.

I would like to thank my thesis advisor Prof. Andrew Kirk for guidance and support he has provided me throughout the course of my Ph.D. program. He always encouraged and refined my new research ideas and gave me independence to pursue them. He had been a great help in teaching me how to think critically by properly documenting each success or failure in a research project. I am deeply obliged to him for all the knowledge he has imparted to me over the last few years. Thank you Prof. Kirk for giving me an opportunity to explore science under your supervision!

I thank my thesis committee members, Prof. Lawrence Chen, and Prof. Maryam Tabrizian for many useful discussions. I also thank Prof. Stephen Arnold for providing me an intuition of whispering gallery modes during his visit to McGill in Summer 2011.

I am thankful to Prof. Andrea Armani for accepting me as an exchange student in her lab at University of Southern California (USC) in Fall 2011. I am grateful to her for all fruitful discussions we had in the last two years. I also thank Simin, Ashley, Ce, Maria, Rasheeda, Victoria, Michele, Jason, Kelvin, Soheil, and Mark for making my stay amazing at USC.

I am grateful to Sandrine for providing me a French translation of my thesis abstract. I also thank my friends and colleagues Venkat, Sandrine, Phil, Chams, Andra, Mehrnoosh, Samira, Ahmed, Graham, Songzhe, and Sara to facilitate a wonderful experience for me at McGill. I also appreciate help in various matters from our amazing administrative assistants, Chris, Maru, Carrie, Rowena, and Connie. Also my experimental work was not possible without great help of our excellent people in the machine shop, Don and Ali. I am grateful to them for providing me machined parts in a timely manner.

I am highly grateful to my academic advisor Prof. Frank Barnes at University of Colorado, Boulder for exposing and teaching me fundamentals of optics. He always helped me in developing proper understanding of important concepts. I am also thankful to my professors Shahid Bokhari, Nauman Zafar, Masood Ahmed (Late), and Noor Sheikh at University of Engineering and Technology Lahore, Pakistan to prepare and inspire me for pursuing Ph.D. research.

I thank my dear friend Usman for his continuous support throughout my stay in

North America. I am also thankful to my friends Ahmed Hayat and Raja for making my stay in Montreal enjoyable.

I am grateful to my parents in law, Akhtar and Shaista, for their love and prayers over the last few years. I am also lucky to have such wonderful sisters Raheela, Shumaila, and Sadia whose love and best wishes are always with me. I would also like to thank my amazing brothers, Waqar and Mohsin, for their constant support and encouragement throughout my life.

I express my deep gratitude to my wife, Amna, who has enriched all aspects of my life in the last seven years. It will take another thesis to explain that without her constant love and support the present thesis will not be possible.

Finally, I do not have words to express my thankfulness to my parents, A.H.Cheema and Shamim Anjum, as I would not be able to reach this level today without their help and prayers. Thank you *Daddy* and *Ammee*! I dedicate this thesis to them and to my wife.

Imran Cheema
Montreal, June 2013

Contents

Abstract	i
Sommaire	iii
Acknowledgements	v
List of Figures	xi
List of Tables	xvii
1 Introduction	1
1.1 Microcavity sensors	2
1.2 Microcavity geometries	3
1.3 Coupling mechanisms	4
1.4 Sensing techniques	7
1.5 Contributions	10
1.5.1 Contribution of authors in published/submitted papers	11
1.6 Summary	12
List of Acronyms	1
2 Preliminary concepts	15
2.1 Whispering gallery mode microcavities	15
2.1.1 Fabrication of the microtoroidal cavity	20
2.2 Cavity ring down spectroscopy	21
2.3 Phase shift-cavity ring down spectroscopy	22

2.3.1	PS-CRDS relations for a free space cavity	22
2.4	Experimental setup	24
2.4.1	Optical fiber tapering setup	24
2.4.2	Microcavity coupling setup	25
2.5	Conclusions	27
3	Mathematical treatment of a cavity coupled with a waveguide for the modulated inputs: PS-CRDS expressions	28
3.1	Fundamental coupled mode equations	29
3.2	CW source	31
3.2.1	Coupling regimes	32
3.2.2	Magnitude and phase of the waveguide field	33
3.3	Pulse (Cavity Ring Down Spectroscopy, CRDS)	35
3.3.1	Coupling regimes	36
3.4	Sinusoid (Phase Shift Cavity Ring Down Spectroscopy, PS-CRDS)	38
3.4.1	Coupling Regimes	40
3.4.2	Phase of the waveguide signal in each coupling regime	41
3.4.3	Experimental point of view	46
3.4.4	Intensity independence	49
3.4.5	Validation for the equations	50
3.5	Conclusions	54
4	Simultaneous measurement of quality factor and wavelength shift by phase shift microcavity ring down spectroscopy	55
4.1	Experimental Setup	57
4.2	Results and discussion	59
4.3	Conclusions	64
5	Accurate determination of the quality factor and tunneling distance of axisymmetric resonators for biosensing applications	65
5.1	Mathematical description	68
5.1.1	Perfectly matched layer formulation	68
5.1.2	Finite element method equation with perfectly matched layer	70
5.1.3	Analytical expressions of the spherical resonator	70

5.2 Results	72
5.2.1 Comparison between simulations and analytical results	72
5.2.2 Comparison between simulations and experimental results	73
5.2.3 Computational speed and numerical accuracy	76
5.3 Discussion and application to PS-CRDS microcavity sensor	77
5.4 Conclusions	81
6 Optimum parameters for achieving maximum signal to noise ratio in microcavity sensors: signal and noise analysis	82
6.1 Signal analysis	84
6.1.1 Modeling results	84
6.1.2 Experimental results	84
6.2 Noise analysis	87
6.2.1 Noise sources	87
6.2.2 Noise in the wavelength measurements	91
6.2.3 Noise in the Q measurements (based upon the Lorentz fit)	93
6.2.4 Noise in the Q measurements (based upon the PS-CRDS)	94
6.3 Signal to Noise Ratio	99
6.4 Conclusions	102
7 Towards more accurate microcavity sensors: maximum likelihood estimation applied to combination of quality factor and wavelength shifts	103
7.1 Estimation model of a sensing event	105
7.1.1 Maximum likelihood estimation: Uncorrelated noise sources	107
7.1.2 Maximum likelihood estimation: Correlated noise sources	108
7.1.3 Discussion of the estimator	108
7.2 Estimation: Experimental results	109
7.3 Distinct estimation regimes: Modeling results	113
7.4 Discussion	114
7.5 Conclusions	117
8 Conclusions	118
A Sensing metric	125

Contents

x

References

127

List of Figures

1.1	A conceptual picture of the optical sensor	1
1.2	The Sensing principle of a microcavity sensor	3
1.3	Coupling configurations a)Prism b)Tapered Fiber c) Fiber Half Block d) Hybrid Fiber Prism e) Silica strip line pedestals antiresonant reflecting waveguide (SPARROW)	6
2.1	(a) Geometrical and (b)Wave representation of the WGMs	16
2.2	Various TE modes of a $105\mu m$ microsphere and a microtoroid ($D = 100\mu m, d = 5\mu m$) around 1550nm ($m=290$). They are obtained from the finite element model presented in Chapter 5.2.1. Top of the second column shows the cross-section of a microtoroidal cavity (see Fig. 2.5).	17
2.3	The original WGM extends out of the microcavity due to a sensing event (adapted from [1])	18
2.4	Loss mechanisms in a microcavity-waveguide system. WGM radiation loss (e.g., a smaller cavity has a higher radiation loss), material loss (e.g., a silica cavity has a higher loss at 633nm than at 1550nm), scattering loss(e.g., the loss due to surface roughness in a microring), surroundings loss (e.g., a microcavity immersed in water has a higher loss at 1550nm than at 633mm), contaminants loss (e.g., scattering or absorption of unwanted particles on a cavity surface or in its surroundings), external coupling loss (e.g., power coupled from a cavity to a coupling waveguide).	20
2.5	Fabrication process of a microtoroidal cavity (provided with permission from Simin Mehrabani).	21
2.6	The CRDS principle	21
2.7	The PS-CRDS principle	23

2.8	The tapering setup	24
2.9	The diffraction colors along thinnest part of the taper	25
2.10	The microcavity coupling setup. (a) Layout of the setup. FG- Function generator (b) The green signal represents the FG voltage and the yellow signal represents the tapered fiber output (c)The full setup (d)The flow cell (e)An image of a microtoroidal cavity along with a taper.	26
3.1	A conceptual picture of the coupled mode model of the microcavity-waveguide system	30
3.2	Input Sources. (a)CW (b)Pulse (c)Sinusoidal	31
3.3	Undercoupled regime for the CW laser source. $Q_{intrinsic} = 1.232 \times 10^6$, $Q_{undercoupled} = 8.21 \times 10^5$, $(1/\tau_e = 0.5/\tau_o)$	34
3.4	Critically Coupled regime for the CW laser source. $Q_{intrinsic} = 1.232 \times 10^6$, $Q_{criticallycoupled} = 6.16 \times 10^5$, $(1/\tau_e = 1/\tau_o)$	34
3.5	Overcoupled regime for the CW laser source. $Q_{intrinsic} = 1.232 \times 10^6$, $Q_{overcoupled} = 4.11 \times 10^5$, $(1/\tau_e = 2/\tau_o)$	35
3.6	Transition region of a tapered fiber	36
3.7	Undercoupled regime.	37
3.8	Critically coupled regime.	37
3.9	Overcoupled regime.	38
3.10	A conceptual picture of the coupled mode model of a microcavity-waveguide system for the PS-CRDS. The cavity field coupled to the waveguide, E_{cwg} , carries a phase shift, ϕ , w.r.t. the input field (assuming 0 input phase). The total waveguide field, E_{wg} , is coherent sum of the E_{cwg} , and the E_{ip} and has a phase shift, θ , w.r.t. the input field, E_{ip}	38
3.11	Undercoupled regime. $1/\tau_e < 1/\tau_o$. Positive phase shift between the input and the waveguide signal is clearly visible.	42
3.12	Critically coupled regime. $1/\tau_e = 1/\tau_o$. Approximately $\frac{\pi}{2}$ phase shift between the input and the waveguide signal.	43
3.13	Overcoupled regime. $1/\tau_e > 1/\tau_o$. Negative phase shift between the input and the waveguide signal is clearly visible.	43
3.14	Strongly overcoupled regime. $1/\tau_e = 10/\tau_o$. The waveguide signal has approximately 2ϕ phase shift.	44

3.15 Undercoupled regime. $\tau_o = 10^{-8}s$, $f_m = 40MHz$. From Eq. (3.26), the undercoupled regime requires, $\frac{2\tau}{\tau_e \sqrt{1 + (\tau\omega_m)^2}} < 1$, as shown in Fig. 3.15(a).	45
3.16 Overcoupled regime. $\tau_o = 10^{-8}s$, $f_m = 40MHz$. From Eq. (3.28), the overcoupled regime requires, $\frac{2\tau}{\tau_e \sqrt{1 + (\tau\omega_m)^2}} > 1$, as shown in Fig. 3.16(a).	46
3.17 Comparison of the PS-CRDS coupled mode equations (CM), the small angle approximation equations and the exact equations, $\tau_o = 10^{-9}s$, $f_m = 40MHz$.	51
3.18 Comparison of the PS-CRDS coupled mode equations (CM), the small angle approximation equations and the exact equations, $\tau_o = 2 \times 10^{-9}s$, $f_m = 40MHz$	51
3.19 Representative undercoupled regime data	53
3.20 Representative overcoupled regime data	53
 4.1 (a) Experimental Setup, FG - Function Generator (b) Magnified view of the microacquarium. A cover slip is placed 2mm (approx.) above the microcavity chip holder with a spacer to form the microacquarium. (c) Scanning electron microscope (SEM) image of the microtoroidal cavity	58
4.2 Two types of measurements (a) Minimum of one of the resonant peak is tracked as function of the biodetection event (b) Phase shift experienced by the waveguide signal is tracked as a function of the biodetection event. With reference to Fig. (a), black sinusoid is extracted at the resonant peak.	60
4.3 Full scan with zoom in view of FSP and BSP (a) Continuous monitoring of phase shift of the waveguide signal (w.r.t FG_2 signal) as function of disassociation of the streptavidin from the biotin (b) Due to limitations of the computer speed, two FSPs and BSPs are separated by 5s respectively.	61
4.4 Experimental parameters. The curves are not smooth because each data point is 5s apart on each curve, a limitation of the computer used in the experiment. In (b), negative values signify that the resonant wavelength is shifting towards blue	62
4.5 A typical error signal for phase shift of the waveguide signal (w.r.t FG_2 signal), recorded by moving the taper far away from the microcavity. Mean: $\pm 0.2662^\circ$, Variance: 0.1076° , mode: $\pm 0.3387^\circ$. Based upon the detected signals, $(\frac{Signal}{Noise})_{min} = 12dB$, and $(\frac{Signal}{Noise})_{max} = 15.8dB$	63

5.1	a) (False color) Logarithmic intensity of the fundamental TE mode of a silica microsphere in air. b) Normalized field intensity along the dashed line shown in (a). Dotted curve shows potential, normalized to k^2 . Tunneling distance is indicated by t.	72
5.2	Modeling results at 1550nm. WGM Quality factors for various silica sphere diameters of fundamental TE mode. OUB and OLB represent upper and lower bounds that are calculated by using Oxborrow's model [2].	74
5.3	Modeling results at 1550nm. Tunneling distance of a fundamental TE mode as a function of the microcavity geometries. Inset of Fig. 5.3(b) shows the cross section of a microtoroidal cavity.	75
5.4	Comparison between the modeling and the experimental results. WGM Quality factors of fundamental TM mode for various silica microtoroidal cavity diameters immersed in ethanol. Minor diameter d of each cavity is slightly different and is around $5\mu m \pm 1\mu m$. The experimental quality factors are determined by Lorentz curve fitting of the resonant peaks ($Q = \lambda/\Delta\lambda$) where $\lambda \approx 1530nm$	76
5.5	Convergence plot for the quality factor determination of a microsphere.	77
5.6	Modeling results show the existence of an optimum geometry . Change in quality factor (ΔQ) of fundamental TM mode as a function of major diameter (D) of a microtoroidal cavity (minor diameter(d) = $6\mu m$) immersed in water. ΔQ shows the difference between Q_{total} for water and that measured when small refractive index change ($\delta n = 10^{-3}$) is introduced into the water. (a)Modeling results for $\lambda = 633nm$ (b)Modeling results for $\lambda = 1530nm$	79
5.7	Modeling results. Various quality factors (Eq. (5.22)) for fundamental TM mode involved in a microtoroidal cavity immersed in water as a function of D ($d = 6\mu m$). In the optimum region the Q_{wgm} is close to Q_{total} .(a) Modeling results at $\lambda = 633nm$. (b) Modeling results at $\lambda = 1530nm$. $Q_{silica} \approx 10^{11}$ (Silica has very low absorption at 1530nm) and is omitted in the figure to reduce the range in y-axis.	80

6.1	Signal results at 765nm. (a), and (c) show the modeling results. (b), and (d) show the experimental results. The inset of (c) is a micrograph of a micro-toroidal cavity and the inset of (d) shows its cross-section. The signals, $\Delta\lambda$, and ΔQ , in response to a RI change (5×10^{-4}), as a function of quality factor (intrinsic for modeling and loaded for experiments) of the cavity in the DI water. The resonant wavelength shifts towards red and the quality factor decreases with the increase of RI. The number at each data point represents the major diameter (D) of the cavity in microns. For the modeling results, minor diameter (d) is fixed at $6\mu m$, while for the experimental results, d is $6 \pm 1\mu m$	86
6.2	Noise sources in the three measurement approaches.	87
6.3	(a)Monte Carlo simulations (MC) of individual noise sources. σ_L -Laser wavelength instability. (b)Total wavelength noise, σ_λ .(c)A representative normal probability density function (pdf) fit of the experimental noise data. The sum of the areas of the rectangles is equal to one.(d)Total quality factor noise, σ_Q	93
6.4	Setup for determination of the noise, σ_N , in the PS-CRDS measurements. .	96
6.5	The experimental noise data ($\sigma_\theta = 4.10 \times 10^{-4}$ deg.) for the phase shift (θ) of the waveguide signal w.r.t to the reference signal (FG ₂).	97
6.6	Determination of the noise in the Q for the same instruments (a)Noise in the Q by using the PS-CRDS, evaluated by a combination of the experiments and the coupled mode equations (Chapter 3). (b) Noise in the Q by using a combination of the Monte Carlo simulations and the Lorentz fit (via OriginLab software.) of the resonant peak.	98
6.7	Setup for showing that the PS-CRDS measurements are independent of the RIN	99
6.8	Results show that the RIN does not contribute to the noise in the PS-CRDS measurements. Typical RIN of the lasers is $10^{-12} - 10^{-15}$ Hz ^{1/2}	99

6.9	Signal to Noise ratio results at 765nm. TJ- Noise due to the taper jitter included (noise data taken in water with the signal data when the cavity and the taper not in contact). NTJ- Noise due to the taper jitter not included (noise data taken in air with the cavity and the taper touching). (a), and (c) show the modeling results. (b), and (d) show the experimental results. In (d) the noise in Q is generated by Monte Carlo simulations at the experimental Q. The number at each data point represents the major diameter (D) of the cavity in microns.	100
6.10	Same data of Fig. 6.9 as a function of major diameter, D, of microtoroidal cavities. (a), and (c) are modeling results. (b), and (d) are experimental results.	101
7.1	The change in wavelength ($\Delta\lambda$) and quality factor (ΔQ) is induced by a sensing event. Each measurement has an experimental noise, i.e., N_λ , and N_Q . The estimator estimates ΔX from the outputs (measurements) of the system.	105
7.2	(a) Experimental setup. FG-Function Generation, Det-Detector. Flow cell is same as the one used in [3] (b)Scanning electron microscope image of a typical microtoroidal cavity (c) Cross section of the microtoroidal cavity showing its dimensions: Major diameter, D , and minor diameter, d	110
7.3	Experimental results. $\Delta\lambda$ is positive (i.e. λ shifts towards red) and ΔQ is negative (i.e. Q decreases) as ΔX increases. This behavior is consistent with the fundamental microcavity theory and is verified by simulations.	111
7.4	A normal probability distribution fit (pdf) to the experimental noise data ($\sigma_\theta = 4.10 \times 10^{-4}$ deg.) for phase shift (θ) of the waveguide signal w.r.t to the reference signal (FG ₂).The sum of the areas of the rectangles is equal to one. From the noise data, the noise (σ_Q) in ΔQ calculation is 30 for the quality factor of 5×10^4 . The noise (σ_λ) in $\Delta\lambda$ measurement is 46 fm. See Section 7.2 for further details and discussion.	112
7.5	Modeling Results. D- $\Delta\lambda$: $\Delta\lambda$ is dominant contributor in the estimator. D- ΔQ : ΔQ is dominant contributor in the estimator. AEC: Approximately equal contribution from the two measurements. For details of the simulation and other symbols, see Section 7.1 and Section 7.3.	114
8.1	Contributions are shown in green.	123

List of Tables

1.1	Various microcavity geometries (Adapted from [4, 5], with modifications). LCORR-Liquid core optical ring resonator, Q-Quality factor	5
1.2	Comparison of various coupling configurations	6
1.3	Comparison of various sensing techniques.	8
7.1	Estimation Results. From the commercial SPR system (GenOptics, France), $\Delta X = 1.95 \times 10^{-3}$ RIU.	112

Chapter 1

Introduction

An optical sensor is a device that uses light as a probe to detect and/or provide information about a specific event. Optical sensors find applications in numerous sectors, e.g., health care, pharmaceutical, environmental monitoring, agriculture, and security [6]. In these applications principle requirements are that the sensor should be (i) sensitive, (ii) real time, (iii) specific, and (iv) inexpensive. Interdisciplinary approaches are required to fulfill all of these requirements. To motivate this, a conceptual diagram of the sensor is shown in Fig. 1.1, i.e., a team of engineers, physicists, biologists, chemists, biochemists, microfluidics experts, and professionals from a target application industry are required to make a successful sensor.

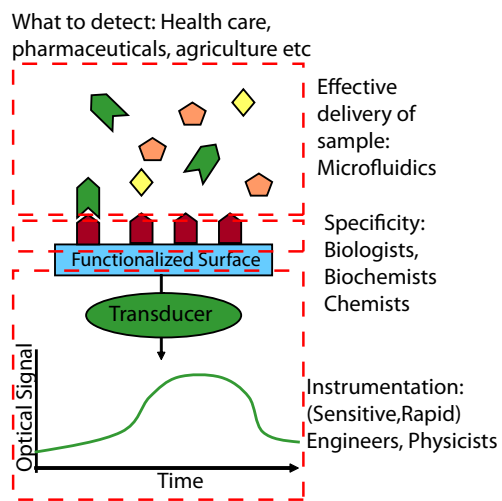


Fig. 1.1 A conceptual picture of the optical sensor

In the last couple of decades many researchers have developed various instrumentation platforms for label free, real time, sensitive and miniature sensors. These platforms include sensors based on surface plasmon resonance, interferometers, waveguides, microcavities, optical fibers, and photonic crystals [7, 8]. Among these platforms, whispering gallery mode (WGM) microcavities¹ with ultra high quality factors ($Q \sim 10^6 - 10^9$) have huge potential for ultra sensitive sensing, as in contrast to the other platforms, light interacts with a sample many times in the microcavity sensors [9, 10, 11]. Motivated from this, the present thesis is focused towards the instrumentation part of the optical sensor, where our goal is to develop novel techniques and related analyses towards optimal microcavity sensors.

We now describe the rest of the chapter. In Section 1.1, we present an intuitive picture of the microcavity sensors. In Section 1.2, we provide the motivation for using microtoroidal cavities by presenting an overview of primary forms of microcavities, demonstrated so far, for sensing applications. In Section 1.3, we provide motivation for using the tapered optical fiber as a coupling technique by comparing various coupling mechanisms for microcavity sensors. Section 1.4 outlines the advantages and disadvantages of four different approaches, used so far, to measure the microcavity parameters in a sensor. We then motivate a reader by asking some research questions followed by our contributions to the field in Section 1.5. Finally, Section 1.6 provides a summary of all the chapters in the thesis.

1.1 Microcavity sensors

Optical microcavities are optical analogues of well studied resonant systems in various disciplines, e.g., a RLC circuit (Electrical), a tuning fork (Acoustic), and a cantilever fixed at one end (Mechanical). These resonant systems are characterized by their resonant frequency and the quality factor. Intuitively a microcavity sensor can be thought of as a resonant system, say RLC circuit (R-resistor, L-inductor, C-capacitor), which is trying to sense changes in one of the circuit parameters (which is induced by a sensing event). The information about the sensing event is extracted by measuring either the change in the resonant frequency or the quality factor of the circuit. From the circuit theory, the

¹In this thesis when we refer to microcavities, it mean those based upon the WGM. We look at theoretical concepts behind the WGM in chapter 2

resonant frequency is a function of L and C, whereas the quality factor is a function of all of the three parameters (R,L,C). Analogously, a change in effective refractive index of the microcavity mode due to a sensing event (L,C) influences both the resonant frequency and the quality factor of the cavity. However, loss experienced by the microcavity mode due to absorption of the sensing event (R) is primarily captured in change of the quality factor of the cavity.

The sensing principle of a typical microcavity sensor is shown in Fig. 1.2. Briefly, the microcavity traps light depending on its geometry, material and incident wavelength. An external coupling mechanism, such as a waveguide, can be used to inject the light of a desired wavelength in the microcavity. In the WGM microcavities, light circulates in the form of traveling waves. The portion of the cavity mode lying outside the microcavity interacts with a sensing event and as a result its properties, such as the resonant wavelength² and the quality factor change. The change of these properties are then correlated to the sensing event.

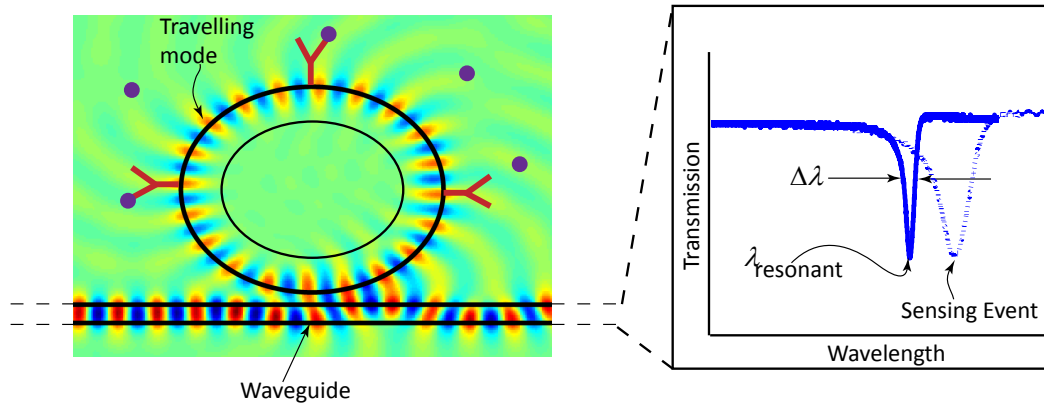


Fig. 1.2 The Sensing principle of a microcavity sensor

1.2 Microcavity geometries

The first microcavity sensor was demonstrated in 2002 [10,11] and was based upon a microsphere. Since then various geometries of microcavities have been used in sensing appli-

²In this thesis, we primarily use the word ‘resonant wavelength’ or simply the wavelength instead of the ‘resonant frequency’. Other than the factor of speed of light, conceptually, both mean the same for the microcavity sensors.

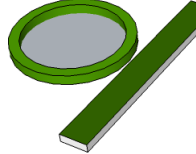
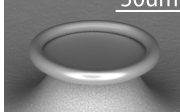
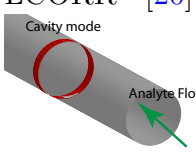
cations. A list of primary microcavity geometries, utilized for various sensing applications, along with some of their properties is shown in table 1.1.

From table 1.1, a microring is a good candidate for a viable sensor however, it suffers from low quality factor due to roughness of the ring along its circumference, a manifestation of the etching process in its fabrication. A microsphere, one of the oldest known microcavities, is much easier to fabricate. A variety of bench-top sensing applications have been demonstrated by utilizing microspheres [5, 21]. However, overall integration of a microsphere with microfluidics and optical components is a challenge, primarily due to the fabrication procedure. Liquid core optical ring resonators (LCORR) provides an inherent integration of the microfluidics but as compared to a microsphere or a microtoroid it suffers from low quality factor. Also integration of the LCORR with optical components is difficult due to its fabrication technique. A microtoroidal cavity, being fabricated using standard optical fabrication procedures, not only possesses a high quality factor but also has a high potential of providing an integrated platform [19, 22]. Motivated from this, we use microtoroidal cavities in this thesis however, it should be noted that focus of the current work is not towards the demonstration of an integrated instrument. Significantly all techniques and analyses, geared towards optimal performance of the sensor, developed in this thesis are applicable to a wide range of microcavity geometries.

1.3 Coupling mechanisms

An important aspect of the microcavity sensor is a coupling mechanism, i.e., a technique of injecting light into the microcavity and monitoring the change in properties of the microcavity as a function of the sensing event. The input light couples to the microcavity when its propagation constant (or momentum) matches to that of a desired cavity mode. To achieve mode matching, various configurations have been proposed as shown in Fig. 1.3. In table 1.2, we compare all of these configurations. Based upon the comparison, SPARROW (Silica strip line pedestals antiresonant reflecting waveguide) coupler is an excellent choice but to date there is no known solution to use it with a microcavity (except with a microring). Therefore, we choose the tapered optical fiber as a coupling mechanism in this thesis. Again, all of the approaches developed in this theses are independent of the mentioned coupling configurations (table 1.2).

Table 1.1 Various microcavity geometries (Adapted from [4, 5], with modifications). LCORR-Liquid core optical ring resonator, Q-Quality factor

Geometry based microcavity sensor	Fabrication	Q: air/water	Microfluidics integration	Optics integration	Multiplexing
Sphere [10, 11] 	Heating an end of a cleaved optical fiber by a flame or a high power laser	$> 10^9 / 10^7 - 10^8$	Not yet, but possible	Not yet, but challenging	Not fully yet [12], but challenging
Ring [13, 14] 	Primarily, standard optical lithography and in few instances [13, 15], nanoimprint lithography	$10^3 - 10^5 / 10^3 - 10^5$	Yes [16]	Not fully yet, but likely [16]	Yes [16]
Toroid [17] 	CO_2 reflow after standard optical lithography [18] or replace the reflow step by chemical etching [19]	$> 10^8 / 10^7 - 10^8$	Not yet, but possible	Not yet, but possible	Not yet, but possible
LCORR [20] 	Heating, while stretching a fused silica capillary	$/ \sim 10^6$	Yes (intrinsic to the cavity)	Not yet, but challenging	Not yet, but challenging

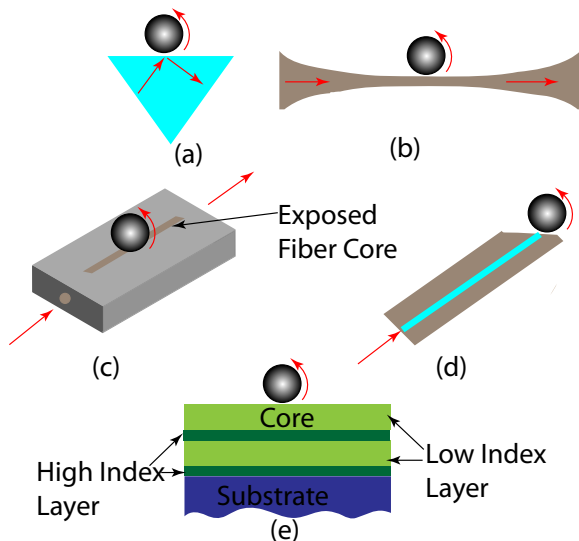


Fig. 1.3 Coupling configurations a)Prism b)Tapered Fiber c) Fiber Half Block d) Hybrid Fiber Prism e) Silica strip line pedestals antiresonant reflecting waveguide (SPARROW)

Table 1.2 Comparison of various coupling configurations

Configuration	Pros	Cons
Prism Coupler [23]	Efficient	Bulky, more optical components are required for the coupling and the extraction
Tapered Fiber Coupler [24]	Efficient, coupling and extraction from the same fiber	Delicate taper, prone to breaking
Fiber Half Block Coupler [25]	Coupling and extraction from the same fiber, not prone to breaking	Less efficient
Hybrid Fiber Prism Coupler [26]	Efficient and somewhat robust	More optical components are required for the extraction
Silica based SPARROW Coupler [27]	Efficient, robust	Extremely difficult to integrate with all the microcavities (except with a microring)

1.4 Sensing techniques

To track changes in properties of a microcavity, as a function of a sensing event, there have been four major techniques utilized so far. In table 1.3, we compare these four methods.

The wavelength tracking method has been primarily used since demonstration of the first microcavity sensor [10, 11]. This method has been used to sense various events. Currently researchers are looking ways to improve performance of the sensor by either enhancing the signal³ or minimizing the noise in the mentioned sensing techniques (table 1.3).

One way to increase the signal is to confine the cavity mode near the surface by using a subwavelength layer on the microcavity. In this approach researchers have reported increase in the sensitivity, by coating higher refractive index layer on a microsphere, for wavelength shift measurements [33]. However, such a coating induces loss for a cavity mode, consequently the quality factor of the cavity degrades.

Signal enhancement is also possible by replacing the passive microcavities with active ones. In active microcavities the effective linewidth of a laser peak becomes narrower than that of the passive cavities. The signal enhancement in active microcavities has been utilized for both wavelength shift [34] and the linewidth splitting [35] approaches. However, an active microcavity has a lower quality factor as compared to that of a passive cavity. Also the impact of active enhancement on the noise in the sensor still requires thorough investigation.

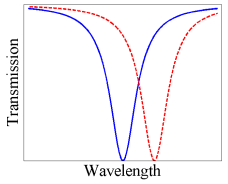
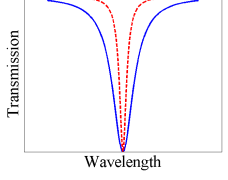
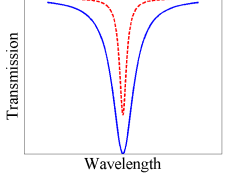
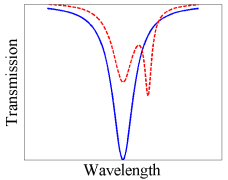
Amplification of the signal in microcavities is also possible by using plasmons [36]. Recently researchers have started utilizing plasmonic enhancement techniques for wavelength shift based microcavity sensors [29, 37]. However, one of the challenging aspects is to immobilize metal particles on the areas of higher mode intensity. The use of metal particles can also degrade the quality factor of the cavity significantly. Also the effect on the sensor noise by plasmonic enhancement approaches still needs a thorough analysis.

The peak linewidth splitting based microcavity sensors require a high quality factor starting resonant peak to resolve the doublet, induced by the sensing event, in the peak. Researchers have proposed an interferometric setup to minimize the effect of this issue [38].

Wavelength instability is one the main noise mechanisms for microcavity sensors. Recently researchers have demonstrated a sophisticated interferometer setup for microcav-

³By signal, we mean measuring change in a desired property, such as the resonant wavelength or the quality factor, of the cavity as a function of a sensing event.

Table 1.3 Comparison of various sensing techniques.

Technique	Implementation	Pros	Cons
Change in the resonant wavelength  Red peak due to the sensing event	(i) Track minimum of the resonant peak directly [28] or (ii) Track minimum of a parabolic fit to the peak [29] or (iii) Fix laser at a wavelength and monitor change in transmission, then extract the resonant wavelength change from the transmission change [13]	Simpler implementation and real time	Ignores absorption of a sensing event, signal depends upon a sensing event's location along the mode profile, noise sources such as laser intensity fluctuation and wavelength instability, parabolic fit method has fit error, transmission change method assumes that the quality factor does not change
Change in the quality factor  Wavelength	Fit the resonant peak to a Lorentzian function and then extract the quality factor [17]	Sense both mode effective index change and absorption due to a sensing event	Non-linear curve fitting, No realtime application demonstrated so far, signal depends upon a sensing event's location along the mode profile, fit error due to the assumed Lorentzian function, noise sources such as laser intensity fluctuation and wavelength instability
Change in transfer characteristics of the cavity  Wavelength	Monitor the resonant peak strength [30, 31]	Simpler implementation and real time	Primarily for absorption measurements, signal depends upon a sensing event's location along the mode profile, noise sources such as laser intensity fluctuation and wavelength instability
Splitting of the single resonant peak into doublet  Wavelength	Fit the doublet to a two peak Lorentzian function and extract the two resonant wavelengths and their separation [32]	Signal independent of a sensing event's location along the mode profile	Non-linear curve fitting, No realtime application demonstrated so far, primarily demonstrated for sizing of solid particles, fit error due to the assumed Lorentzian function, noise sources such as laser intensity fluctuation and wavelength instability

ity sensors, based upon the wavelength shift measurement approach, to minimize effect of the wavelength noise [39].

All of the above mentioned approaches have been utilized to probe various sensing events ranging from detection of protein, DNA, virus, binding kinetics to sizing of nanobeads [5]. We now mention some of the notable works. In 2007, detection of single molecule, Interleukin-2, was claimed by using wavelength tracking method in conjunction with a microtoroidal cavity (detection limit (DL):15kDa, signal to noise ratio (SNR):10, Q:1 – 2×10^8) [40]. However, major discrepancies had been indicated in this work. [41, 42]. In 2008, researchers demonstrated detection of single virus, InfluenzaA, by employing wavelength measurement approach in a microsphere (DL: $\sim 300,000$ kDa, SNR:3, Q: 6.4×10^5) [43]. In 2011, researchers employed an interferometer to minimize the noise in wavelength measurement technique and demonstrated detection of single InfluenzaA virus using a microtoroidal cavity (DL: $\sim 300,000$ kDa, SNR:38, Q: 10^7 – 10^8) [39]. In 2011, single InfluenzaA was detected by using an active microtoroidal cavity in conjunction with the linewidth splitting approach (DL: $\sim 300,000$ kDa, SNR:300, Q: 6×10^6) [35]. However, this demonstration was in air rather than in water. In 2012, researchers reported detection of single RNA virus, MS2, by using a plasmonic enhancement technique along with wavelength measurement approach in a microsphere (DL: ~ 3011 kDa, SNR:8, Q: 4×10^5) [29]. In 2013, detection of single protein, Thyroglobulin, had been reported by employing a plasmonic enhancement method in conjunction with wavelength tracking approach in a microsphere (DL:66kDa, SNR:13, Q: 4×10^5) [44]. For sensitive, realtime, specific, and inexpensive detection of analytes further work on measurement techniques and related analyses (considered in this thesis), microfluidics, surface chemistry and microfabrication is highly desired.

Based upon the information presented so far, one may ask many research questions. Some of these are:

- Is there an alternative way to track the changes which a sensing event induces in properties of a microcavity which is real time, sensitive and has a higher noise immunity?
- All of the aforementioned methods measure one of the parameters of the cavity, e.g., the resonant wavelength or the quality factor. Is there a way to track multiple parameters simultaneously and in real time as a function of a sensing event⁴?

⁴One can think of an approach, similar to the first and the second in table 1.3, where in a sensing

- If we are able to track multiple parameters simultaneously, is it useful?, i.e., can we develop a sensing modality which can provide a better estimate of a sensing event based upon measurement of the multiple parameters?
- Accurate expressions/models are necessary for designing an optimal microcavity sensor. Analytical expressions for the wavelength and the quality factor for some of microcavities, e.g., microspheres, exist [45]. But what about the expressions/models for other microcavities, such as microtoroidal cavities?
- Noise analysis is an essential part of any sensor, however, little attention has been given to it [46,47]. Can we have a comprehensive noise analysis of microcavity sensors?
- Currently, it is often stated in the literature that maximum sensitivity is obtained by operating a microcavity at its highest possible quality factor [4,48,49]. Is this really true? How does the quality factor impact the signal and the noise of the microcavity sensor?
- There are a plethora of sensor platforms available in the literature. From the instrumentation (see Fig.1.1) point of view, can we have a metric with which can compare performance of the multiple sensors?

The answers to the above questions are contributions of the thesis, which have been published⁵ in the form of journal articles and proceedings.

1.5 Contributions

We now outline the main contributions of the thesis.

- Mathematical treatment and demonstration of a first microcavity sensor based upon the phase shift-cavity ring down spectroscopy. We show that it is possible to simultaneously measure the resonant wavelength and the quality factor, as a function of the sensing event, in real time and with higher noise immunity. This was reported by Cheema et al. in [50,51,3,52].

experiment the resonant peak is fitted by a Lorentzian curve to extract both the resonant wavelength and the quality factor. However, such an approach requires extra signal processing and is not real time due to inherent slowness of the non-linear curve fitting process.

⁵Some material is in the process of publication

- Develop an accurate finite element model of axisymmetric WGM microcavities for determining the resonant wavelength, the quality factor, and the tunneling distance. This was reported by Cheema et al. in [53, 54].
- Comprehensive signal and noise analysis of the microcavity sensors that measure changes in the resonant wavelength and the quality factor to probe a sensing event, This was reported by Cheema et al. in [55, 56].
- Demonstrate that there is an optimal size and quality factor for a microcavity at which the maximum signal to noise ratio (SNR) is obtained, and that a highest quality factor may not result in the highest SNR. This was reported by Cheema et al. in [56].
- Model and demonstrate that a combination of the resonant wavelength and the quality factor measurements of a microcavity sensor provide a more accurate sensing approach. The model is extended to develop a sensing metric to compare the performance of a wide range of sensors (optical or non-optical).This was reported by Cheema et al. in [55, 57].

1.5.1 Contribution of authors in published/submitted papers

- In [51, 3], S.Mehrabani and A.A.Hayat undertook the fabrication of the microtoroidal cavities, under the guidance of Prof. A.M.Armani (University of Southern California) and Prof. Y-A Peter (Ecole Polytechnique de Montreal) respectively. S. Mehrabani also functionalized the microcavities under the guidance of Prof. A.M.Armani. The author of this thesis, M. I. Cheema, developed the technique, performed the reported experiments at University of Southern California under the guidance of Prof. A.M.Armani. (proof of concept experiments were done earlier at McGill University), analyzed the data, and wrote the paper. The co-authors further helped with paper edits and structure. The overall work was carried out under the supervision of the thesis adviser, Prof. A.G.Kirk.
- In [56], C.Shi performed the experiments according to my directions and under the guidance of Prof. A.M.Armani at University of Southern California. Prof. A.M.Armani provided guidance on overall objective of the paper. The author of

this thesis, M. I. Cheema, developed the technique, analyzed the data, and wrote the paper. The co-authors further helped with paper edits and structure. The overall work was carried out under the supervision of the thesis adviser, Prof. A.G.Kirk.

- In [55, 57], Prof. U.A.Khan (Tufts University) guided the development of the signal processing framework, in particular, the mathematical model and estimation techniques. The microtoroidal cavities were provided by Prof. A.M.Armani and she also guided experiments. The author of this thesis, M. I. Cheema, developed the technique, performed the experiments (at McGill University), analyzed the data, and wrote the paper. The co-authors further helped with paper edits and structure. The overall work was carried out under the supervision of the thesis adviser, Prof. A.G.Kirk.

1.6 Summary

We now summarize the rest of the thesis.

Chapter 2: In this chapter, we provide the background material necessary to understand the rest of the thesis. It includes theoretical description of the WGM microcavities, the cavity ring down spectroscopy (CRDS), and the phase shift cavity ring down spectroscopy (PS-CRDS). We also provide description of the general experimental setup, including fabrication of the tapered optical fibers.

Chapter 3: By using the coupled mode theory, we derive the PS-CRDS expressions for a microcavity coupled with a waveguide. We also derive the conditions for the coupling regimes of a PS-CRDS based microcavity sensor, which differ from the conditions for a CW input. We cast the derived expressions in a way to be useful for the real experiments.

Chapter 4: Until now, the primary method of detection has been based upon tracking the resonant wavelength shift as a function of biodetection events. One of the sources of noise in all resonant-wavelength shift measurements is the noise due to intensity fluctuations of the laser source. An alternative approach is to track the change in the quality factor of the optical cavity by using phase shift cavity ring down spectroscopy, a technique which is insensitive to the intensity fluctuations of the laser source. In this chapter, using biotinylated microtoroid resonant cavities, we show simultaneous

measurement of the quality factor and the wavelength shift by using phase shift cavity ring down spectroscopy. These measurements were performed for disassociation phase of biotin-streptavidin reaction. We find that the disassociation curves are in good agreement with the previously published results.

Chapter 5: In the previous chapter, we demonstrate that a microcavity biosensor can track a biodetection event as a function of its quality factor by using phase shift cavity ring down spectroscopy (PS-CRDS). However, to achieve maximum sensitivity, it is necessary to optimize the microcavity parameters for a given sensing application. In this chapter, we introduce an improved finite element model which allows us to determine the optimized geometry for the PS-CRDS sensor. The improved model not only provides fast and accurate determination of quality factors but also determines the tunneling distance of axisymmetric resonators. The improved model is validated numerically, analytically, and experimentally.

Chapter 6: The work in past few years has been focused on optimizing the microcavity performance by increasing the quality factor of the cavity. However, this approach overlooks the impact of the quality factor on the signal to noise ratio (SNR) of the sensor. In this chapter, our purpose is to show the existence of optimum parameters, both theoretically and experimentally, for achieving maximum SNR in the microcavity sensors. In particular, we conduct a comprehensive signal and noise analysis of a microtoroidal cavity, that is utilized as a refractometric sensor followed by demonstration of a distinct optimum SNR region for the sensor. We find that the maximum SNR is not at the maximum quality factor of the microcavity. In addition, we also show that the quality factor measurements, using the PS-CRDS, have high noise immunity as compared to that of the Lorentz fit based measurements.

Chapter 7: In microcavity sensors, a sensing event is estimated by measuring shift in the resonant wavelength, or in the quality factor of the microcavity. However, all published work only uses one of these measures for estimating the sensing event. In this chapter, we show that the estimation accuracy of a sensing event can be improved by a combination of both the quality factor and the resonant wavelength measurements in a microcavity sensor. These two measurements act as inputs to a mathematical model that we develop by using principle of maximum likelihood

estimation. We further demonstrate an experimental application of this model by introducing a refractive index change for a microtoroidal cavity sensor immersed in a liquid. By further using the finite element method simulations in conjunction with the estimator model, we show the existence of three distinct measurement regimes as a function of the quality factor of the microcavity. Finally, the estimator model is extended to develop a sensing metric to compare performance of multiple sensors.

Chapter 8: In this chapter, we conclude the thesis and discuss our contributions.

Note that each chapter contains additional references to provide the motivation and to compare our work to existing works.

Chapter 2

Preliminary concepts

In this chapter, we present the preliminary concepts required to develop a better understanding of the rest of the thesis. In Section 2.1, we provide a description of the whispering gallery modes along with an explanation of the resonant wavelength, the quality factor and the fabrication process of a microtoroidal cavity. Cavity ring down spectroscopy (CRDS) and phase shift-cavity ring down spectroscopy (PS-CRDS) are explained in Sections 2.2 and 2.3, respectively. The details of the experimental setup for coupling light into microcavities are given in Section 2.4. Finally, we conclude the chapter in Section 2.5.

2.1 Whispering gallery mode microcavities

The mathematical treatment of the whispering gallery modes (WGM) in a microcavity has been comprehensively presented in numerous works [45, 58, 1, 59, 60]. In this section, we provide a conceptual picture of the WGM with reference to sensing applications.

In dielectric microcavities, such as silica microspheres, microrings, and microtoroids, light travels in the form of whispering gallery modes (WGM). The name WGM came from Lord Rayleigh's explanation of the propagation of acoustic waves along walls of the gallery located under the dome of St. Paul Cathedral in London [61]. In the geometrical optics regime, the WGMs can be thought of as totally internally reflected waves propagating in a circular orbit within a cavity as shown in Fig. 2.1. In the wave optics regime, the WGMs represent those waves that do not occupy whole volume of the cavity, rather, they travel along the cavity surface with some of their portion extending outside the cavity.

The WGM can be characterized by four parameters, namely, (i) polarization (TE

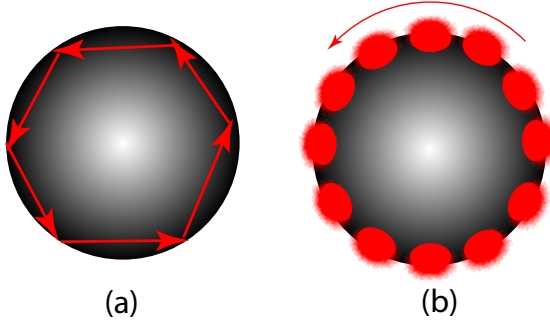


Fig. 2.1 (a) Geometrical and (b)Wave representation of the WGMs

or TM), (ii) total angular momentum number, l , (iii) azimuthal angular momentum number, m , and (iv) radial quantum number, ν . Based upon these parameters, following are some of the important points for a mode of a microsphere [58], and a microtoroidal cavity [59, 60]:

- With an analogy to the electromagnetic treatment of optical waveguides, l determines the total wave number, k , and m determines the propagation constant, β , of a WGM. For a microsphere of radius a ,
$$k = \frac{\sqrt{l(l+1)}}{a}, \quad (2.1)$$
- The number of WGM maxima in the radial direction are ν for a microsphere, whereas for a microtoroid they are given by $2\nu + 1$.
- For a microsphere, the fundamental mode is represented by $\nu = 1$, $l = m$, whereas for a microtoroid it is represented by $\nu = 0$, $l = 0$.
- For a microsphere, the number of WGM maxima in the polar direction are given by $l - m + 1$.

These points are illustrated in Fig. 2.2.

The number of modes in a microcavity depends upon its size. Since the minor diameter of a microtoroidal cavity is typically in the range of $3 - 10\mu\text{m}$, it supports fewer modes as compared to a microsphere whose diameter may reach to $500\mu\text{m}$. This results in a sparser and a simpler mode spectrum for a microtoroidal cavity which is useful for sensing applications.

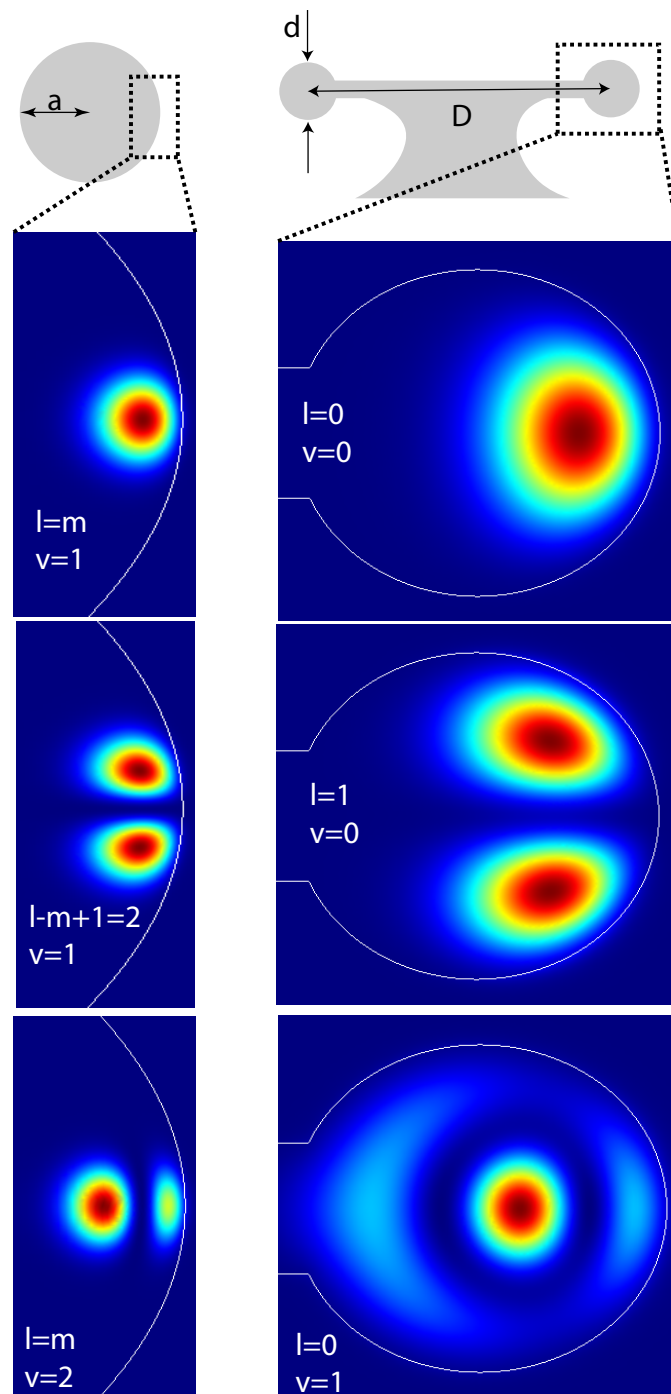


Fig. 2.2 Various TE modes of a $105\mu m$ microsphere and a microtoroid ($D = 100\mu m, d = 5\mu m$) around 1550nm ($m=290$). They are obtained from the finite element model presented in Chapter 5.2.1. Top of the second column shows the cross-section of a microtoroidal cavity (see Fig. 2.5).

Resonant wavelength

An approximate condition for the resonant wavelength of a microsphere can be derived from Eq. (2.1),

$$2\pi a = \lambda_r l, \quad \text{for } l \gg 1, \quad (2.2)$$

where λ_r represents the effective resonant wavelength. Equation (2.2) states that l wavelengths (λ_r) are present along the circumference of the microsphere ($2\pi a$). Similarly in our experience with the finite element model of a microtoroidal cavity (Chapter 5), an approximate condition of a resonant wavelength for a fundamental mode of a microtoroidal cavity is

$$\pi(D + d) \approx \lambda_r l, \quad (2.3)$$

where D , and d represent the major and the minor diameters of the cavity (Fig. 2.2).

From the sensing perspective, we assume that the microcavity (refractive index, n_m) is immersed in a medium of refractive index $n_w < n_m$. If n_w increases or the effective size of the cavity increases due to a sensing event then the WGM further extends out of the cavity and consequently the resonant wavelength shifts towards red. This is graphically shown in Fig. 2.3.

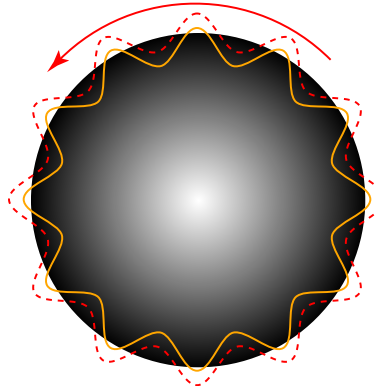


Fig. 2.3 The original WGM extends out of the microcavity due to a sensing event (adapted from [1])

Quality factor

The quality factor (Q) of a microcavity is an important parameter which encompasses all of the losses experienced by the cavity. It is defined as

$$Q = \omega_o \frac{\text{Time-averaged energy stored}}{\text{Power loss}}. \quad (2.4)$$

From the principle of conservation of energy, it can be shown that the decay of energy (U) follows the following time dependant equation [62]

$$U(t) = U_o e^{\frac{-\omega_o t}{Q}}, \quad (2.5)$$

where ω_o is the resonant frequency, and U_o is the initial energy stored in the cavity. Equation (2.5) can be written as

$$U(t) = U_o e^{\frac{-t}{\tau}}, \quad (2.6)$$

where τ represents the ‘ring down’ time of the cavity and is related to Q by

$$Q = \omega_o \tau. \quad (2.7)$$

Equation (2.7) provides the time domain definition of Q whereas, by taking the Fourier transform of Eq. (2.5), one can obtain the frequency domain definition of Q ,

$$Q = \frac{\omega_o}{\Delta\omega} = \frac{\lambda_r}{\Delta\lambda}, \quad (2.8)$$

where $\Delta\omega$, and $\Delta\lambda$ are the FWHM of the cavity line shape function (typically assumed as a Lorentzian) in the frequency and the wavelength units, respectively.

The rate of decay of energy in a microcavity can be due to a variety of loss mechanisms including the WGM radiation, the absorption by surroundings of the microcavity, the intrinsic material absorption, the scattering from surface inhomogeneities of the cavity, the surface contaminants, and the external coupling. Therefore, the overall rate of decay is given by

$$\frac{1}{\tau} = \frac{1}{\tau_{wgm}} + \frac{1}{\tau_{surroundings}} + \frac{1}{\tau_{material}} + \frac{1}{\tau_{scattering}} + \frac{1}{\tau_{contaminants}} + \frac{1}{\tau_{external}}, \quad (2.9)$$

$$\frac{1}{\tau} = \frac{1}{\tau_o} + \frac{1}{\tau_e}, \quad (2.10)$$

where other than the external coupling decay rate, $1/\tau_e$, all of the other decay rates come

under the cavity intrinsic loss and are lumped into a single parameter, $1/\tau_o$. Similarly, the total quality quality of the cavity can also be represented as

$$\frac{1}{Q} = \frac{1}{Q_o} + \frac{1}{Q_e}. \quad (2.11)$$

A physical representation of each of the losses is shown in Fig. 2.4.

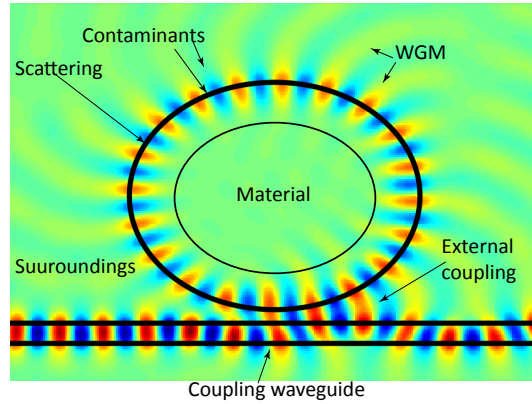


Fig. 2.4 Loss mechanisms in a microcavity-waveguide system. WGM radiation loss (e.g., a smaller cavity has a higher radiation loss), material loss (e.g., a silica cavity has a higher loss at 633nm than at 1550nm), scattering loss(e.g., the loss due to surface roughness in a microring), surroundings loss (e.g., a microcavity immersed in water has a higher loss at 1550nm than at 633mm), contaminants loss (e.g., scattering or absorption of unwanted particles on a cavity surface or in its surroundings), external coupling loss (e.g., power coupled from a cavity to a coupling waveguide).

Again from the sensing perspective, if n_w increases due to a sensing event then Q_{wgm} decreases (see Figs. 2.3–2.4) and consequently the total quality factor, Q , of the cavity decreases. Similarly, absorption of a sensing event primarily influences $Q_{surroundings}$.

2.1.1 Fabrication of the microtoroidal cavity¹

The microtoroids are fabricated on $2\mu m$ thermally grown silica on silicon wafers. First, silica micropads are patterned on the silicon wafer by photolithography techniques and buffered HF etching at a room temperature. Next, XeF_2 gas at 2800mmHg is used to

¹We do not fabricate the microtoroidal cavities at McGill. We collaborate with Prof. Andrea Armani at Univ. of Southern California, and Prof. Yves-Alain Peter at Ecole Polytechnique, Montreal for their fabrication.

isotropically undercut the silicon which results in silica microdisks on top of the silicon pillars. Finally, the disks are reflowed by a 50W CO₂ laser to form the microtoroids. The major diameter (Fig. 2.2) of the microtoroids is primarily controlled by an initial size of the disks, whereas their minor diameter (Fig. 2.2) is primarily controlled by the reflow process [18]. The fabrication process is shown in Fig. 2.5.

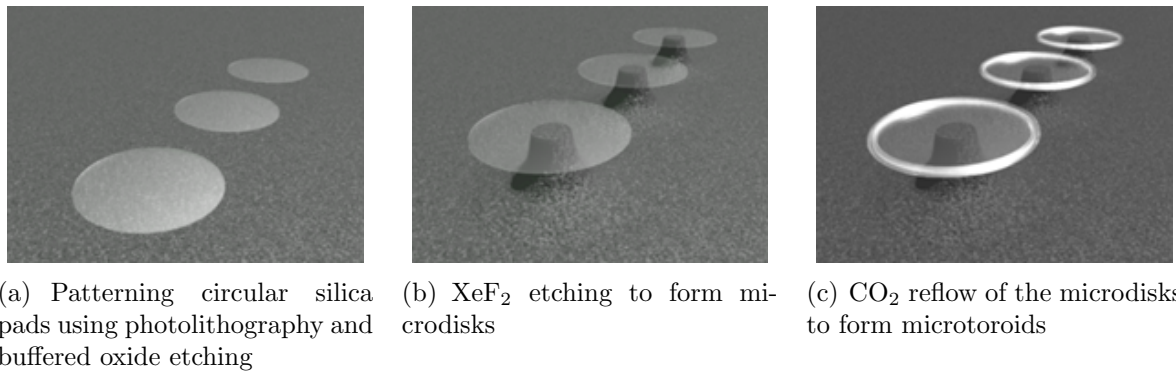


Fig. 2.5 Fabrication process of a microtoroidal cavity (provided with permission from Simin Mehrabani).

2.2 Cavity ring down spectroscopy

The working principle of the CRDS for free space cavities is shown in Fig. 2.6.

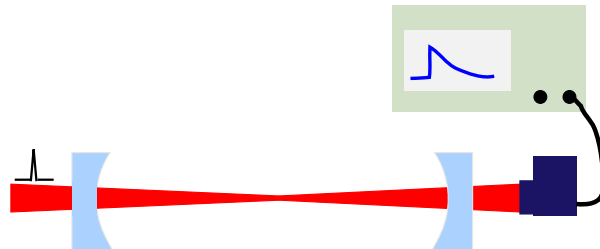


Fig. 2.6 The CRDS principle

Laser light is coupled into a cavity via mode matching optics. After achieving the resonance, the laser is switched off which initiates leakage of the light out of the cavity that decays over time. The decay rate, Eq.(2.9), is then determined by applying an exponential fitting algorithm to the detected light.

The CRDS measurements for both of free space cavities and microcavities coupled with a waveguide are similar. From the sensing perspective, the decay rate is correlated with a sensing event.

2.3 Phase shift-cavity ring down spectroscopy

The CRDS requires an exponential fitting of the detector output which is not suitable for a real time sensing application. This drawback can be removed by using PS-CRDS. In PS-CRDS, modulated light from a CW laser source is injected into a cavity. The output light from the cavity has a phase shift, with respect to the input light, that is related to the ring down time, τ , of the cavity [63].

An experimental determination of the phase shift, ϕ , for a free space cavity differs significantly from that of a microcavity-waveguide system. The major difference is that in a free space cavity, the output light is solely from the cavity, whereas in a microcavity-waveguide system the output light is a coherent sum of both of the input and the microcavity light. Here, we derive an expression of the phase shift, ϕ , for a free space cavity, whereas a microcavity-waveguide system for the PS-CRDS measurements is dealt in detail in Chapter 3.

2.3.1 PS-CRDS relations for a free space cavity [63, 64]

The intensity of a modulated light entering the cavity can be represented by

$$I_{ip} = I_o(1 + \alpha_i \sin \omega_m t), \quad (2.12)$$

where α_i is the modulation depth and ω_m is the modulation frequency. The impulse response of the cavity is

$$h(t) = C \exp\left(-\frac{t}{\tau}\right). \quad (2.13)$$

Therefore, intensity at the cavity output is

$$I_{op}(t) = I_{ip} * h(t) \quad (2.14)$$

$$= C \int_{-\infty}^t I_o(1 + \alpha_i \sin \omega_m t') \exp\left(-\frac{t-t'}{\tau}\right) dt', \quad (2.15)$$

where \tilde{t} is a dummy variable for performing the convolution. The value of C can be found by applying the principle of conservation of energy, i.e., total intensity coupled to the cavity in a time interval must be equal to the intensity coupled out in that time interval,

$$C \int_{-\infty}^t I \exp\left(-\frac{t-\tilde{t}}{\tau}\right) d\tilde{t} = I, \quad (2.16)$$

$$\Rightarrow C = \frac{1}{\tau}. \quad (2.17)$$

Substituting value of C in Eq. (2.15), and after many lines of algebra it can be shown that

$$I_{op}(t) = I(1 + \alpha_o \sin(\omega t + \phi)), \quad (2.18)$$

where

$$\tan \phi = -\omega_m \tau, \quad (2.19)$$

$$\alpha_o = \frac{\alpha_i}{\sqrt{1 + \omega_m^2 \tau^2}}, \quad (2.20)$$

i.e., the output light has a phase shift, ϕ , w.r.t. the input light. Both of the phase shift, ϕ , and the output modulation depth, α_o , can be correlated to a sensing event.

It has been shown that the phase shift, ϕ , can be measured in an intensity independent way [63] by using the phase sensitive detection (PSD) technique [65]. The PSD technique can be implemented either in a software, such as NI Labview®, or one can use commercially available lock-in amplifiers which work on the principle of PSD.

Figure 2.7 shows a graphical relationship between the input and the output waves in the free space PS-CRDS system.

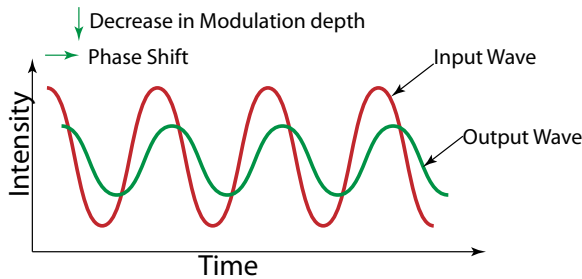


Fig. 2.7 The PS-CRDS principle

2.4 Experimental setup

In this section, we explain the experimental setup for coupling of laser light into microcavities. The experimental setup consists of two parts, namely,(i) optical fiber tapering setup, and (ii) microcavity coupling setup. In the following, we briefly describe each of them.

2.4.1 Optical fiber tapering setup

The tapered optical fibers provide an efficient coupling mechanism for injecting light into microcavities. In a tapered fiber, a portion of the optical fiber is thin enough ($< 2\mu m$), such that an electromagnetic field can evanescently couple from it to a microcavity. The primary purpose of a tapering setup is to fabricate these thin portions in standard optical fibers, such as SMF-28. Another goal of a tapering setup is to make sure that these thin portions are long enough to meet the requirements of a coupling setup. Our setup for the tapering of optical fibers is shown in Fig. 2.8.

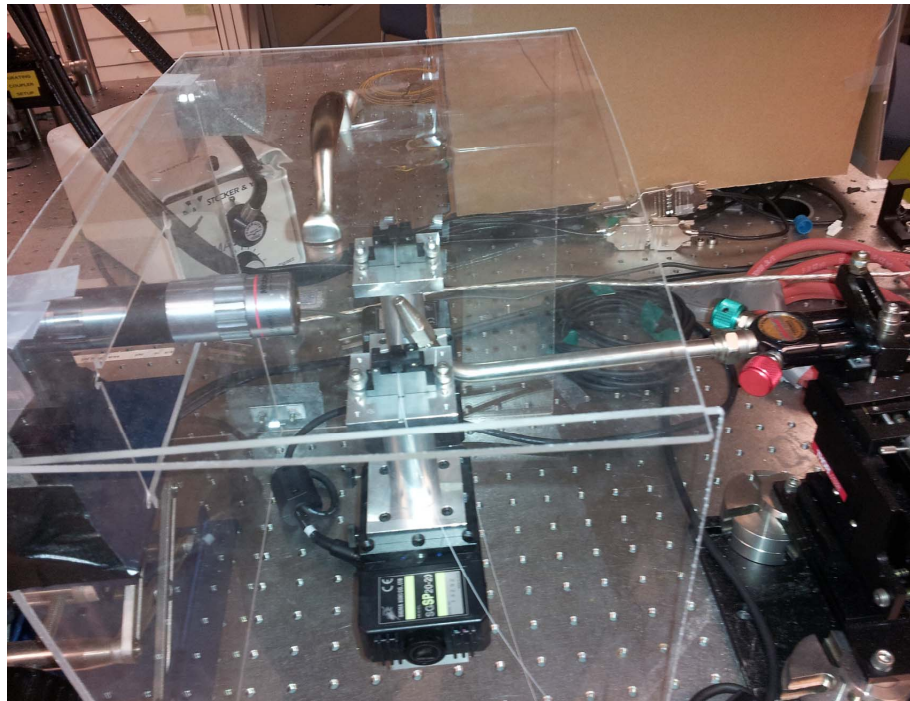


Fig. 2.8 The tapering setup

The tapered fibers are fabricated by heating an optical fiber while pulling it through

the computer controlled motorized stages. The heating is provided by the hydrogen torch which rests on the 3 axis stage to position the flame for the optimal tapering process. During the pulling process, an image of the tapered fiber is continuously monitored through the imaging system. The tapering process is manually stopped by simultaneously switching off the motorized stages and the hydrogen flame at the instant when the image shows the diffraction colors (Fig. 2.9) along thinnest part of the taper. Any sag in the taper is then minimized by pulling one end of the taper manually through the micrometer on any of the stage. To minimize effect of air currents, the whole setup is closed by plexiglass sheets from the top and the three sides. Our tapering setup usually produces $\sim 1\mu\text{m}$ thin tapers, that are 3-4cm long with 0.5-2dB loss. Since the motorized stages rest on a portable block, the fabricated taper along with the stages are easily transferable to the coupling setup.



Fig. 2.9 The diffraction colors along thinnest part of the taper

2.4.2 Microcavity coupling setup

The purpose of a coupling setup is to ensure (a) appropriate optical conditions, and (b) optimal positioning of a microcavity and a tapered fiber to achieve a desired coupling between them. Our microcavity coupling setup is shown in Fig. 2.10. A chip containing microtoroidal cavities is placed on a mount on a 3-axis positioning stage (10nm resolution) whereas, the position of the taper is controlled by a 2 axis stage ($1\mu\text{m}$ resolution).

A CW tunable laser is used as an input source for the taper. The smallest wavelength step in tunable lasers is usually 1-100pm. This limits the highest observable quality factor to $\sim 10^6$ at 1550nm. Moreover, the process of changing the wavelength in steps is extremely slow and is not suitable for sensing applications. This issue can be overcome by modulating the wavelength of the laser externally. The option of fine wavelength tuning through an external function generator is usually available in modern tunable lasers, e.g., Yenista Optics Tunics T100R, and Newport TLB 6700. To ensure a steady state operation of the microcavity, voltage and frequency of the function generator waveform are constrained by

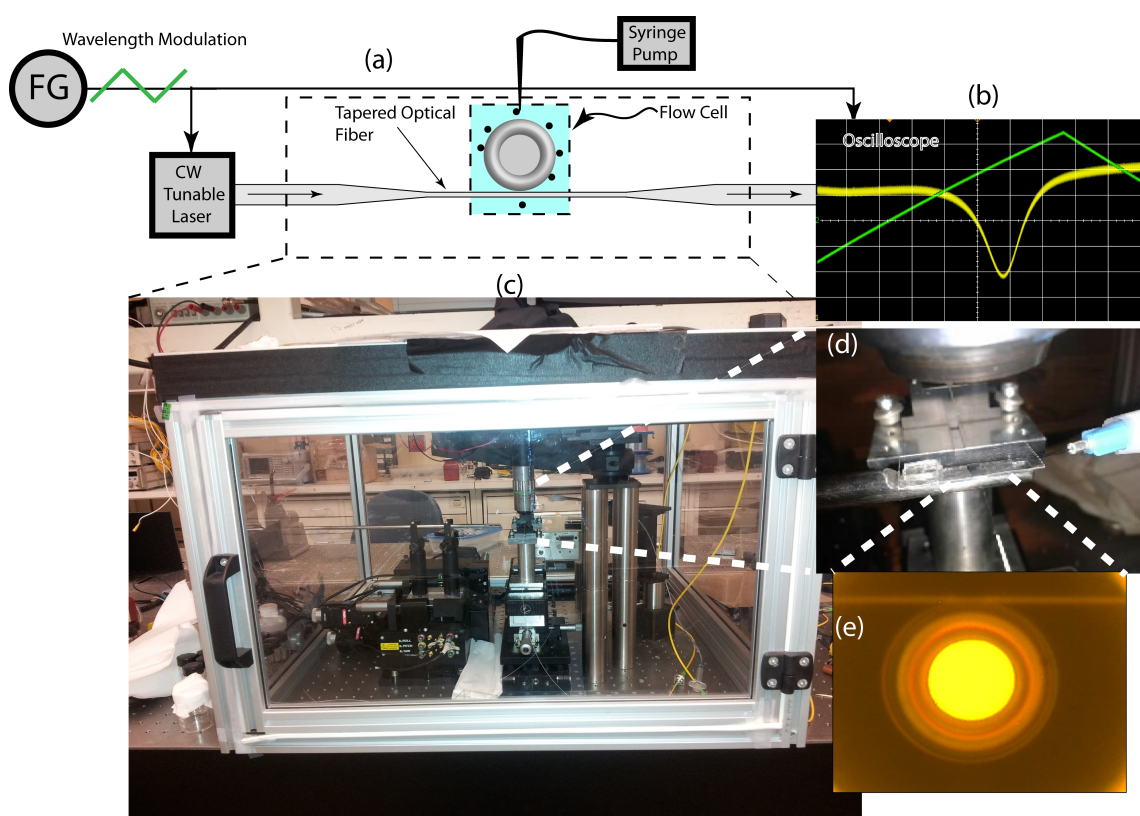


Fig. 2.10 The microcavity coupling setup. (a) Layout of the setup. FG-Function generator (b) The green signal represents the FG voltage and the yellow signal represents the tapered fiber output (c)The full setup (d)The flow cell (e)An image of a microtoroidal cavity along with a taper.

the following relation [66]

$$\left(\frac{\text{Volts}}{\text{seconds}} \right) (\text{LCF}) \ll \frac{\text{Change in the wavelength}}{\tau} = \frac{2\pi c}{Q^2}, \quad (2.21)$$

where LCF represents a laser conversion factor of mapping the input voltage to the wavelength units.

With the laser and the function generator on, the resonant peaks are found by positioning the microcavity and the taper within the coupling distance (typically $< 1\mu\text{m}$). To minimize any movements in the taper (taper jitter) due to air currents, the whole setup is enclosed in the transparent box.

2.5 Conclusions

To facilitate better understanding of the rest of the thesis for a reader, we explain background concepts including the WGM microcavities, the resonance wavelength, the quality factor, the CRDS, and the PS-CRDS. We also describe our experimental setup for coupling light into microcavities.

Chapter 3

Mathematical treatment of a cavity coupled with a waveguide for the modulated inputs: PS-CRDS expressions

An accurate mathematical model is the key to understand any physical system. To date, there has been no complete and accurate mathematical model demonstrated for understanding the PS-CRDS measurements in a microcavity-waveguide system. However, in 2008, by approximating the cavity-waveguide system with a four mirror model [67], Barnes et al. [68] developed an expression for the phase shift, θ , of the *waveguide signal*. They then evaluated the expression experimentally at multiple modulation frequencies to extract the ring down time of the cavity in air. However, to determine the ring down time in the scattering mode¹, they employed the standard expressions of PS-CRDS (Chapter 2) by assuming that the captured light is scattered solely from the cavity while the light scattered from the waveguide has negligible contribution. In this thesis we do not focus on the scattering mode as capturing of the scattered light through a liquid medium with an acceptable signal to noise ratio is challenging for sensing applications.

As explained in Chapter 2, the phase shift, ϕ , ² of the *cavity signal* gives the direct

¹Here, it means that any light scattered from the cavity in free space

²Barnes et al. use the symbol ϕ for phase shifts of both the waveguide and the cavity signal in their paper [68]

information of the cavity ring down time, whereas the waveguide signal represents a coherent sum of the input signal and the cavity signal. In the present chapter, with aid of the coupled mode theory, we develop explicit expressions for the microcavity phase shift, ϕ . We also show the conditions for the various coupling regimes in the PS-CRDS system, which differ than that of the continuous wave case. In our treatment, we assume a microcavity as a black box with a given ring down time (or a quality factor). In Chapter 5, we develop an accurate electromagnetic model to determine the quality factor of any axisymmetric WGM microcavity. That model and the expressions developed in the present chapter provide a complete picture of the PS-CRDS measurements for a microcavity coupled with a waveguide.

We now describe the rest of the chapter. In Section 3.1, we provide the fundamental coupled mode (CM) equations for a cavity-waveguide system. For a continuous wave (CW) laser source, solution of the CM equations and the conditions for the coupling regimes are presented in Section 3.2. In Section 3.3, we solve CM equations for a pulse laser source and also provide experimental results for the coupling regimes. Then we look at solution of the CM equations in detail for a sinusoidal input (PS-CRDS). In particular, we (i) derive the expressions for magnitude and phase of the cavity and the waveguide fields (Section 3.4), (ii) derive the conditions for the coupling regimes (Section 3.4.1), (iii) look at a couple of conditions and their implications for phase shift of the waveguide signal (Section 3.4.2), (iv) derive the approximate and the exact expressions, to be used in experiments, for phase shift of the cavity signal in terms of the experimentally measured parameters (Section 3.4.3), (v) show that calculation of the phase shift of the cavity field from the measured parameters does not involve any of the intensity terms (Section 3.4.4), and (vi) validate the PS-CRDS expressions numerical and experimentally (Section 3.4.5). Finally, we conclude the chapter in Section 3.5.

3.1 Fundamental coupled mode equations

We use the coupled mode (CM) treatment to develop a theoretical analysis of a microcavity coupled with a waveguide (tapered optical fiber). A conceptual microcavity-waveguide system is shown in Fig. 3.1.

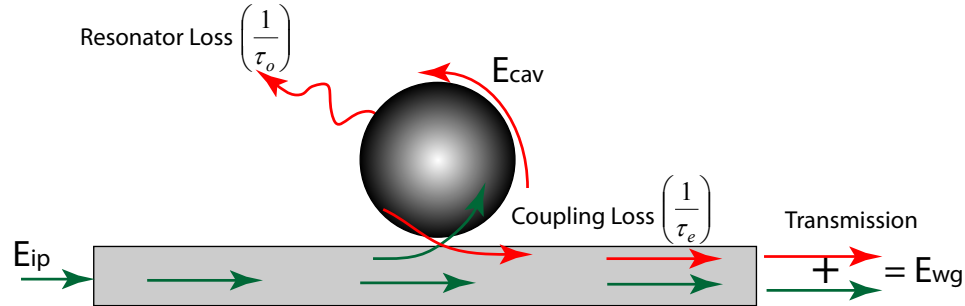


Fig. 3.1 A conceptual picture of the coupled mode model of the microcavity-waveguide system

The fundamental CM equations of a cavity coupled to a waveguide are [69]

$$\frac{dE_{cav}}{dt} = j\omega_o E_{cav} - \left(\frac{1}{\tau_o} + \frac{1}{\tau_e} \right) E_{cav} + \kappa E_{ip}, \quad (3.1)$$

$$E_{wg} = E_{ip} - \kappa E_{cav}, \quad (3.2)$$

where E_{cav} is the cavity field, ω_o is resonant frequency, $\frac{1}{\tau_o}$ is decay rate due to the cavity intrinsic loss, $\frac{1}{\tau_e}$ is decay rate due to the coupling loss (loss due to coupling of the field to the waveguide), E_{ip} is field at input of the waveguide, E_{wg} is field at output of the waveguide, and κ is a coupling parameter given as,

$$\kappa = \left| \sqrt{\frac{2}{\tau_e}} \right|. \quad (3.3)$$

Equation (3.3) has been derived by using conservation of energy [69]. A negative sign, with the second term of Eq. (3.2), is due to coupling of the input field from the waveguide to the cavity ($\pi/2$ phase shift) and then back from the cavity to the waveguide (over all π phase shift)

Intuitively, Eq. (3.1) can be represented as

$$\underbrace{\frac{dE_{cav}}{dt}}_{\text{rate of change of the cavity field}} = \underbrace{j\omega_o E_{cav}}_{\text{the cavity field}} - \underbrace{\left(\frac{1}{\tau} \right) E_{cav}}_{\text{loss experienced by the cavity field}} + \underbrace{\kappa E_{ip}}_{\text{coupling from the waveguide}}, \quad (3.4)$$

where ring down time, τ , of the cavity is defined as

$$\frac{1}{\tau} = \frac{1}{\tau_o} + \frac{1}{\tau_e}. \quad (3.5)$$

In the following, we examine the solutions of Eq. (3.1) and Eq. (3.2) for three different input cases (Fig. 3.2) namely, (i) CW source, (ii) pulse source (cavity ring down spectroscopy, CRDS), and (iii) sinusoidal source (phase shift-cavity ring down spectroscopy, PS-CRDS).

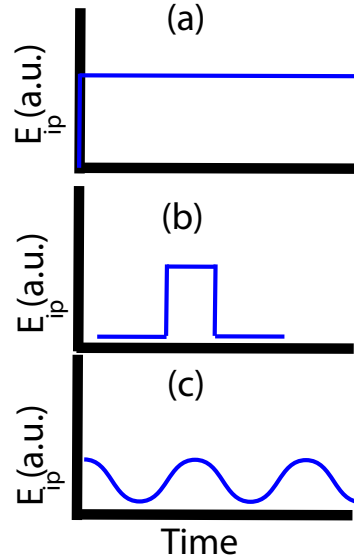


Fig. 3.2 Input Sources. (a)CW (b)Pulse (c)Sinusoidal

3.2 CW source

The CW laser source can be treated as a step input, with a magnitude E_{in} and a frequency ω , to the coupled mode equations. Solving Eq. (3.1) and Eq. (3.2) using this input,

$$E_{cav}(t) = \frac{\sqrt{2/\tau_e} E_{in}}{1/\tau + j(\omega - \omega_o)} [e^{j\omega t} - e^{(j\omega_o - 1/\tau)t}], \quad (3.6)$$

The second term in the cavity field represents the transient component. In the steady state, the cavity field is given by

$$E_{cav} = \frac{\sqrt{2/\tau_e} E_{in}}{1/\tau + j(\omega - \omega_o)} e^{j\omega t}. \quad (3.7)$$

Therefore, the field in the waveguide is obtained by substituting Eq. (3.7) in Eq. (3.2),

$$E_{wg} = \frac{\frac{1}{\tau_o} - \frac{1}{\tau_e} - j(\omega - \omega_o)}{\frac{1}{\tau_o} + \frac{1}{\tau_e} + j(\omega - \omega_o)} E_{in} e^{j\omega t}. \quad (3.8)$$

3.2.1 Coupling regimes

Based upon the relationship between the cavity field coupled back to the waveguide, κE_{cav} , and the input field, E_{ip} , there are three distinct regimes of operation for a cavity-waveguide system. These regimes are commonly known as the coupling regimes. In this section, we examine at the conditions for each of these regimes.

At resonance, $\omega = \omega_o$, Eq. (3.8) reduces to

$$E_{wg} = \frac{\frac{1}{\tau_o} - \frac{1}{\tau_e}}{\frac{1}{\tau_o} + \frac{1}{\tau_e}} E_{in} e^{j\omega_o t}. \quad (3.9)$$

Based upon Eq. (3.9), the three distinct coupling regimes are:

- **Undercoupled.** The condition for the undercoupled regime is

$$\frac{1}{\tau_o} > \frac{1}{\tau_e}, \quad (3.10)$$

i.e., the power coupled from the cavity to the waveguide (coupling loss) is less than the power dissipated in the cavity (cavity loss) i.e., $\kappa E_{cav} < E_{ip}$.

- **Critically coupled.** The condition for the critically coupled regime is

$$\frac{1}{\tau_o} = \frac{1}{\tau_e}, \quad (3.11)$$

i.e., the power coupled from the cavity to the waveguide (coupling loss) is equal to the power dissipated in the cavity (cavity loss). In this situation, there is a zero signal in the waveguide i.e., $\kappa E_{cav} = E_{ip}$. Intuitively, in this situation, the cavity field coupled

back to the waveguide has the same magnitude but π phase shifted w.r.t the input field, consequently, there is a zero waveguide signal.

- **Overcoupled.** The condition for the overcoupled regime is

$$\frac{1}{\tau_o} < \frac{1}{\tau_e}, \quad (3.12)$$

i.e., the power coupled from the cavity to the waveguide (coupling loss) is greater than the power dissipated in the cavity (cavity loss) i.e., $\kappa E_{cav} > E_{ip}$.

3.2.2 Magnitude and phase of the waveguide field

The quality factor for the cavity-waveguide system is given by Eq.(3.13)(see Section 2.1),

$$Q = \frac{\omega_o}{\Delta\omega} = \frac{\lambda_o}{\Delta\lambda} = \omega_o\tau, \quad (3.13)$$

i.e., the quality factor is affected by the coupling regime and the value measured in the undercoupled regime is closer to the intrinsic quality factor ($Q = \omega_o\tau_o$). Figures 3.3–3.5 show the intensity and the phase plots, generated by using Eq. (3.8), as a function of the CW laser frequency for the three coupling regimes. Phase plots (Figs. 3.3(b)-3.5(b)) show that at the resonant frequency, the waveguide signal for undercoupled and overcoupled regimes are π phase shifted whereas the phase discontinuity in the critical coupling plot occurs at the point of zero waveguide signal (see Eq. (3.8)). The zero waveguide signal in the critically coupled regime is due to the fact that E_{in} and E_{cav} are equal in amplitude and have π phase difference.

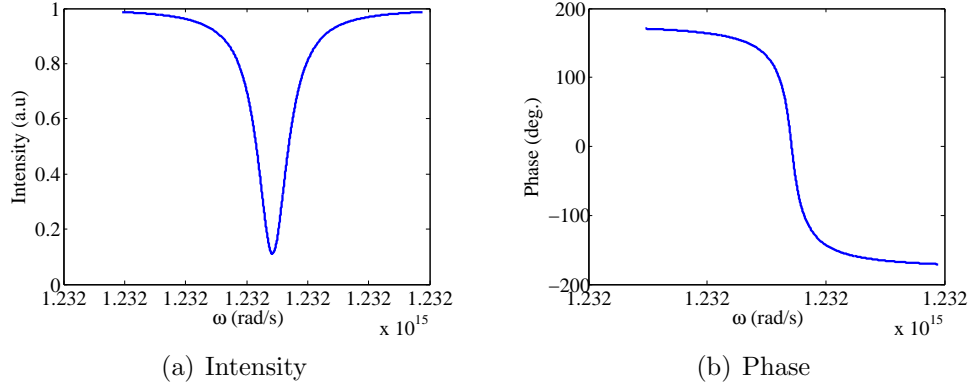


Fig. 3.3 Undercoupled regime for the CW laser source. $Q_{intrinsic} = 1.232 \times 10^6$, $Q_{undercoupled} = 8.21 \times 10^5$, $(1/\tau_e = 0.5/\tau_o)$

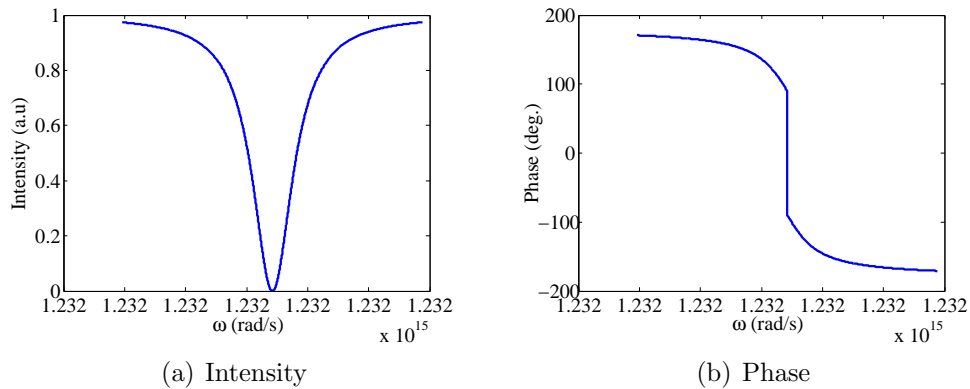


Fig. 3.4 Critically Coupled regime for the CW laser source. $Q_{intrinsic} = 1.232 \times 10^6$, $Q_{criticallycoupled} = 6.16 \times 10^5$, $(1/\tau_e = 1/\tau_o)$

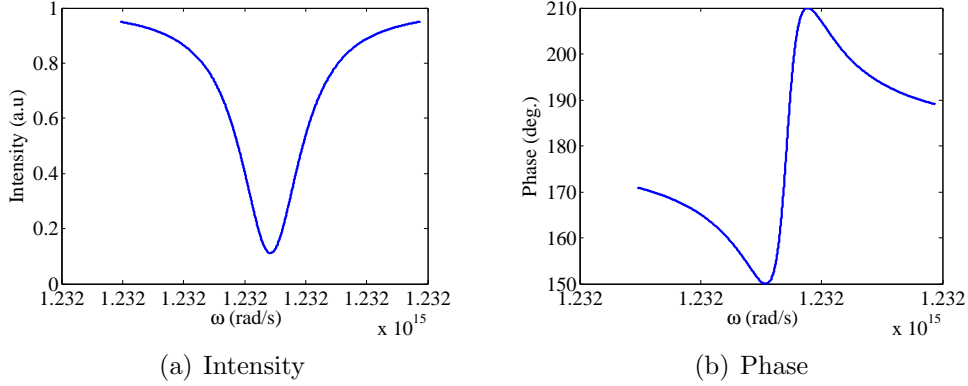


Fig. 3.5 Overcoupled regime for the CW laser source. $Q_{intrinsic} = 1.232 \times 10^6$, $Q_{overcoupled} = 4.11 \times 10^5$, $(1/\tau_e = 2/\tau_o)$

3.3 Pulse (Cavity Ring Down Spectroscopy, CRDS)

For modeling the pulse input, we use Eq. (3.6) at a resonant wavelength in conjunction with Eq. (3.2). To represent the cavity field (E_{cav}) at a zero input, we induce the exponential decay (corresponding to the ring down time of the cavity) of a field present in the cavity immediately before the input pulse goes to zero. Therefore, the cavity field, E_{cav} , at the resonant wavelength is given by Eq. (3.14),

$$E_{cav}(t) = \begin{cases} \frac{\sqrt{2/\tau_e}}{1/\tau} [1 - e^{-t/\tau}] E_{in} e^{j\omega_o t} & E_{ip} \neq 0, \\ E_p e^{-t/\tau} e^{j\omega_o t} & E_{ip} = 0, \end{cases} \quad (3.14)$$

where E_p is field in the cavity immediately prior to the moment when E_{ip} goes to zero.

The waveguide field, E_{wg} , is obtained by using Eq. (3.14) in Eq. (3.2) and is given by Eq. (3.15),

$$E_{wg}(t) = \begin{cases} \left(1 - \frac{2/\tau_e}{1/\tau} [1 - e^{-t/\tau}] \right) E_{in} e^{j\omega_o t} & E_{ip} \neq 0, \\ \sqrt{2/\tau_e} E_p e^{-t/\tau} e^{j\omega_o t} & E_{ip} = 0. \end{cases} \quad (3.15)$$

3.3.1 Coupling regimes

The same coupling regimes and the mathematical relationships (Eqs.(3.10)–(3.12)) apply in the pulse case, as shown previously for the CW laser case. Figures 3.7–3.9 show the modeling and the experimental results for each of the coupling regimes. It should be noted that the modeling results are not for the same conditions as that of the experimental results. The experimental pulse length is shorter than the time for the cavity to reach the steady state. In the modeling, rise and fall time of the pulse are taken as 0 however, experimentally there are always finite rise and fall times as can be seen clearly in Figs. 3.7(b), 3.8(b), and 3.9(b).

The experiments are performed at 1530nm by coupling a pulse, obtained by externally modulating a CW laser, into the cavity at the resonant wavelength. The resonant wavelength is initially determined by using a high resolution Optical Spectrum Analyzer. The experiments are performed with the taper and the cavity in contact. The coupling regimes are obtained by varying the coupling loss. The coupling loss is varied by coupling the cavity from various points of transition region of the taper (Fig.3.6).



Fig. 3.6 Transition region of a tapered fiber

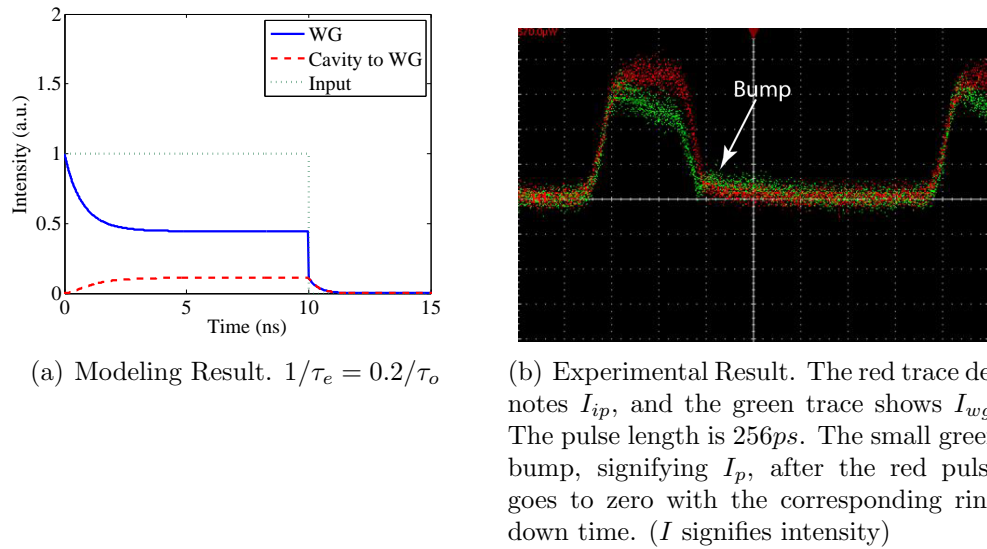


Fig. 3.7 Undercoupled regime.

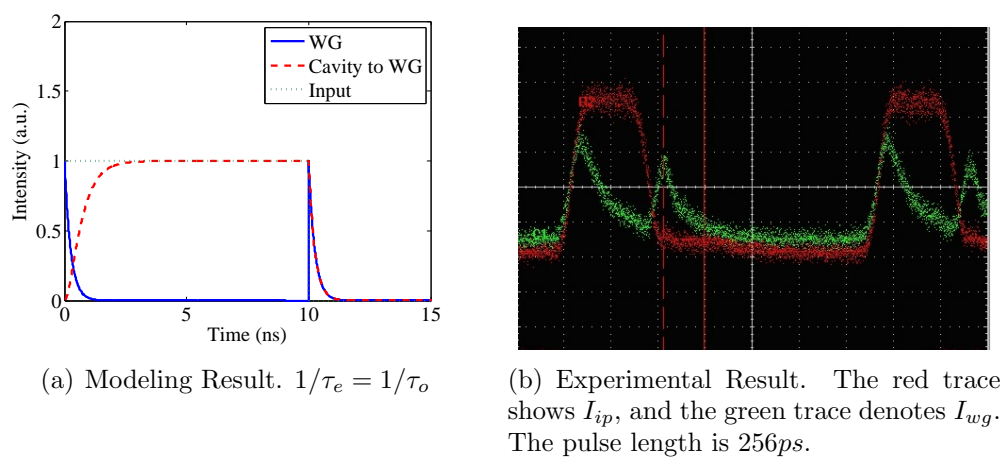


Fig. 3.8 Critically coupled regime.

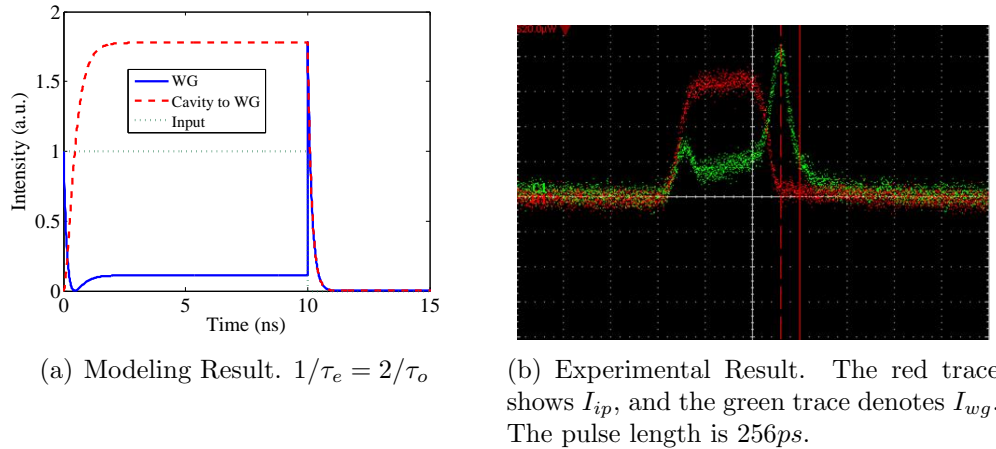


Fig. 3.9 Overcoupled regime.

3.4 Sinusoid (Phase Shift Cavity Ring Down Spectroscopy, PS-CRDS)

We now use a sinusoid as an input to the CM equations and derive the fundamental expressions for PS-CRDS system. A conceptual microcavity-waveguide system for the PS-CRDS is shown in Fig. 3.10.

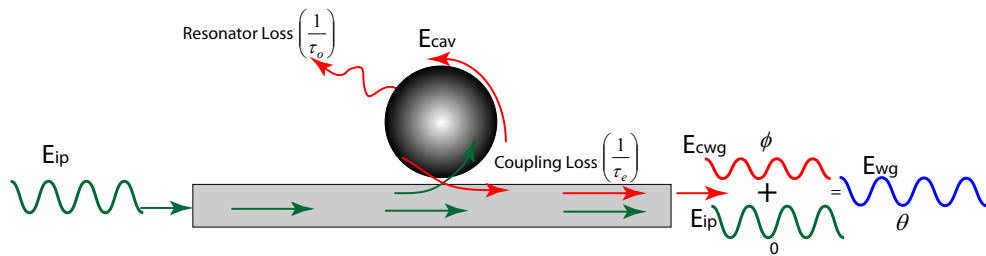


Fig. 3.10 A conceptual picture of the coupled mode model of a microcavity-waveguide system for the PS-CRDS. The cavity field coupled to the waveguide, E_{cwg} , carries a phase shift, ϕ , w.r.t. the input field (assuming 0 input phase). The total waveguide field, E_{wg} , is coherent sum of the E_{cwg} , and the E_{ip} and has a phase shift, θ , w.r.t. the input field, E_{ip} .

Experimentally, a sinusoid is generated by either direct or external modulation of a CW laser source. Mathematically, the sinusoid can be modeled by using a positive

frequency component of $\cos(\omega_m t) \cos(\omega t)$, i.e., E_{ip} is given by Eq. (3.16).

$$E_{ip} = \frac{e^{j(\omega+\omega_m)t} + e^{j(\omega-\omega_m)t}}{4}, \quad (3.16)$$

where ω represents frequency of the input optical field, and ω_m represents the frequency of a modulation signal. Using Eq. (3.16) as an input to the coupled mode equations, Eqs. (3.1)–(3.2), results in the cavity field that is given by Eq. (3.17),

$$E_{cav}(t) = \frac{\sqrt{2/\tau_e}\tau (-2e^{(j\omega_o-1/\tau)t}(1-j\tau(\omega_o-\omega)) + e^{j(\omega-\omega_m)t}(1+j\tau(\omega_m-\omega_o+\omega)) + e^{j(\omega+\omega_m)t}(1-j\tau(\omega_m+\omega_o-\omega)))}{4(1-j\tau(\omega_m+\omega_o-\omega))(1+j\tau(\omega_m-\omega_o+\omega))} E_{ip}. \quad (3.17)$$

At the resonance Eq. (3.17) reduces to Eq. (3.18),

$$E_{cav}(t) = \frac{\sqrt{2/\tau_e}\tau (-2e^{(-t/\tau)t} + e^{-j\omega_m t}(1+j\tau\omega_m) + e^{j\omega_m t}(1-j\tau\omega_m))}{4(1+(\tau\omega_m)^2)} E_{ip} e^{j\omega_o t}. \quad (3.18)$$

The waveguide signal is then obtained by substituting Eq. (3.16) and Eq. (3.18) in Eq. (3.2).

To determine the coupling regimes and phase shift of the cavity and the waveguide signals w.r.t the input signal, we need to obtain the cavity field coupled back to the waveguide ($\sqrt{2/\tau_e}E_{cav}$). This field can easily be deduced from Eq. (3.18) in the steady state at the resonant frequency (positive exponential) and is given by Eq. (3.19),

$$E_{cwg} = \kappa E_{cav} = \frac{2\tau(1-j\tau\omega_m)}{\tau_e(1+(\tau\omega_m)^2)} E_{ip}. \quad (3.19)$$

The phase of E_{cwg} can be obtained by taking the ratio of imaginary and real parts of Eq. (3.19). Consequently, phase shift of E_{cwg} field (i.e the field coupling from the cavity back to the waveguide) w.r.t to E_{ip} sinusoidal field is given by Eq. (3.20),

$$\boxed{\phi = -\tan^{-1}(\omega_m\tau)}, \quad (3.20)$$

where ‘-’ sign signifies that the cavity field always lags w.r.t. the input field. The angle, ϕ , represents the phase shift between $\kappa E_{cav} = E_{cwg}$ and E_{ip} , where E_{ip} is assumed to have a zero starting phase. It is clear that if we determine the phase shift, ϕ , we know the ring

down time, τ , and consequently the quality factor of the cavity. Similarly the magnitude of E_{cwg} is given by Eq. (3.21),

$$|E_{cwg}| = \frac{2\tau}{\tau_e \sqrt{1 + (\tau\omega_m)^2}} |E_{ip}|. \quad (3.21)$$

However, it is the magnitude and relative phase of the waveguide signal that is measured experimentally and so it is important to determine the expressions for them. Starting with the waveguide signal,

$$E_{wg} = E_{ip} - E_{cwg}, \quad (3.22)$$

$$= \frac{1 + (\tau\omega_m)^2 - \frac{2\tau}{\tau_e} + j \left(\frac{2\tau^2}{\tau_e} \omega_m \right)}{1 + (\tau\omega_m)^2} E_{ip}, \quad (3.23)$$

the phase of the waveguide signal (using the real and the imaginary parts of above equation) is given by Eq. (3.24),

$$\theta = \tan^{-1} \left(\frac{\frac{2\tau^2}{\tau_e} \omega_m}{1 + (\tau\omega_m)^2 - \frac{2\tau}{\tau_e}} \right). \quad (3.24)$$

The angle, θ , represents the phase shift between E_{wg} and E_{ip} .

Similarly, magnitude of the waveguide signal is given by Eq. (3.25),

$$|E_{wg}| = \frac{\sqrt{\left(1 + (\tau\omega_m)^2 - \frac{2\tau}{\tau_e}\right)^2 + \left(\frac{2\tau^2}{\tau_e} \omega_m\right)^2}}{1 + (\tau\omega_m)^2} |E_{ip}|. \quad (3.25)$$

Equations (3.20), (3.21), (3.24), and (3.25) are the fundamental equations of a cavity coupled with a waveguide for studying the PS-CRDS applications.

We can see from these expressions that calculation of the loaded ring down time, τ , and hence the loaded Q requires measurement of both the phase shift and the relative amplitude of the light in the waveguide. In Section 3.4.3, we look over this in more detail.

3.4.1 Coupling Regimes

We now deduce the coupling regimes from Eq. (3.21).

- **Undercoupled** regime requires $\kappa E_{cav} = E_{cwg} < E_{ip}$ i.e.,

$$\frac{1}{\tau} > \frac{2}{\tau_e \sqrt{1 + (\tau \omega_m)^2}}, \quad (3.26)$$

which reduces to $\frac{1}{\tau_o} > \frac{1}{\tau_e}$ for $\omega_m = 0$, as in the previously mentioned CW and the pulse cases.

- **Critically coupled** regime requires $\kappa E_{cav} = E_{cwg} = E_{ip}$ i.e.,

$$\frac{1}{\tau} = \frac{2}{\tau_e \sqrt{1 + (\tau \omega_m)^2}}, \quad (3.27)$$

which reduces to $\frac{1}{\tau_o} = \frac{1}{\tau_e}$ for $\omega_m = 0$, as in the previously mentioned CW and the pulse cases. However, it should be noted that in the sinusoidal input regime, *the waveguide signal is non zero as opposed to the CW laser input case*. The reason is that although the condition, $\kappa E_{cav} = E_{cwg} = E_{ip}$, is true the phase difference between the two components is not π , as the field, E_{cwg} , carries an additional phase shift due to various losses (Fig. 2.4) experienced by the cavity (Eq. (3.20)).

- **Overcoupled** regime requires $\kappa E_{cav} = E_{cwg} > E_{ip}$ i.e.,

$$\frac{1}{\tau} < \frac{2}{\tau_e \sqrt{1 + (\tau \omega_m)^2}}, \quad (3.28)$$

which reduces to $\frac{1}{\tau_o} < \frac{1}{\tau_e}$ for $\omega_m = 0$, as in the previously mentioned CW and the pulse cases.

3.4.2 Phase of the waveguide signal in each coupling regime

Since experimentally we measure phase shift of the waveguide signal, θ , let us look at it in further detail. We consider two cases:

(i) When $\omega_m \tau \ll 1$

This is a typical situation in our experiments since we use modulation frequency in the range of $1 - 50 MHz$ (bandwidth limitation of the available equipment) and the typical ring down times are in the range of $10^{-9} - 10^{-12} s$. In this approximation, the coupling

regimes presented in Eqs. (3.26), (3.27), and (3.28) reduce to Eqs. (3.10), (3.11), and (3.12) respectively. However, as explained previously, we have a non-zero waveguide signal in the critically coupled regime. Rewriting the phase shift, θ , of the waveguide signal (Eq. (3.24)) for the approximation, $\omega_m\tau \ll 1$,

$$\theta = \tan^{-1} \left(\frac{2\tau\omega_m}{\tau_e \left(\frac{1}{\tau_o} - \frac{1}{\tau_e} \right)} \right). \quad (3.29)$$

From Eq. (3.29), it is clear that in order to achieve a larger θ (for higher signal to noise ratio), the modulation frequency, ω_m , should also be larger. Therefore, depending upon specifications of the available equipment, a higher ω_m is chosen for experiments reported in this thesis.

From Eq. (3.29), it is also clear that sign of the phase shift, θ , is

- Positive for the undercoupled regime.
- Negative for the overcoupled regime.
- Close to $\frac{\pi}{2}$ for the critically coupled regime

Figures 3.11, 3.12, and 3.13, show each of these coupling regimes.

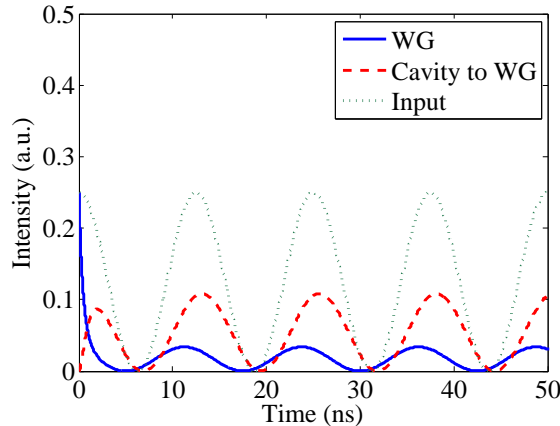


Fig. 3.11 Undercoupled regime. $1/\tau_e < 1/\tau_o$. Positive phase shift between the input and the waveguide signal is clearly visible.

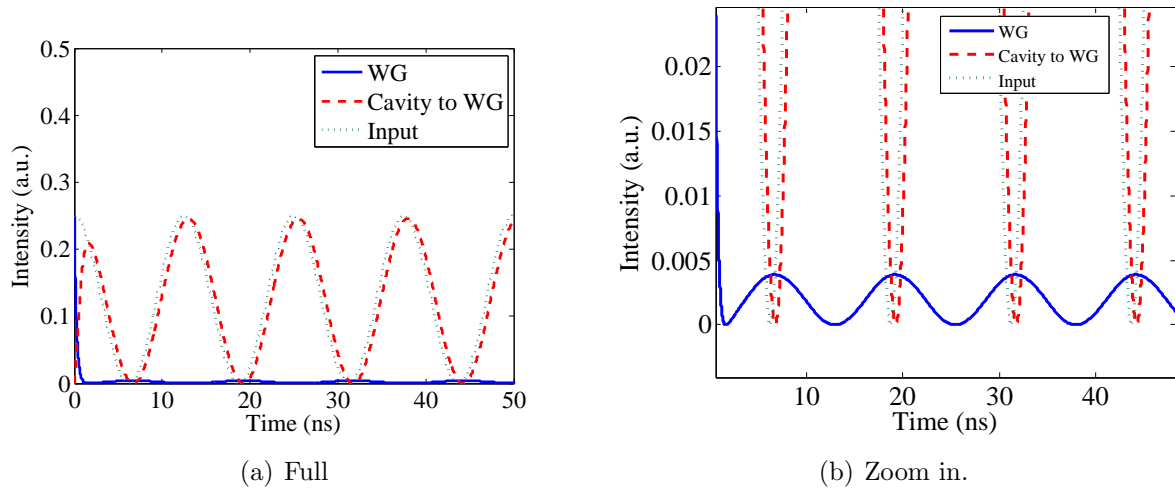


Fig. 3.12 Critically coupled regime. $1/\tau_e = 1/\tau_o$. Approximately $\frac{\pi}{2}$ phase shift between the input and the waveguide signal.

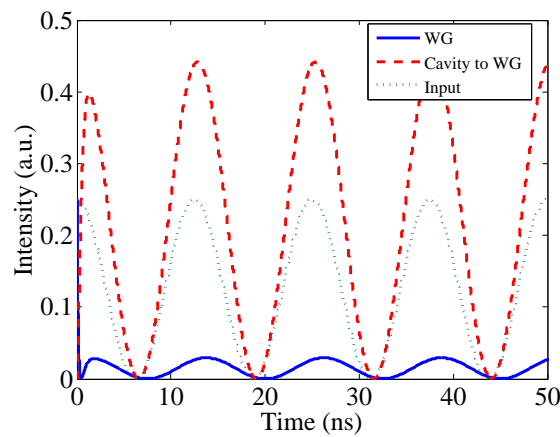


Fig. 3.13 Overcoupled regime. $1/\tau_e > 1/\tau_o$. Negative phase shift between the input and the waveguide signal is clearly visible.

We can also see that for the strongly overcoupled regime, $\frac{1}{\tau_e} \gg \frac{1}{\tau_o}$, Eq. (3.29) becomes

$$\theta = -\tan^{-1}(2\pi\omega_m), \quad (3.30)$$

i.e., in the strongly overcoupled case, measurement of the waveguide phase shift allows direct calculation of the loaded ring down time of the cavity. This is evident in Fig. 3.14.

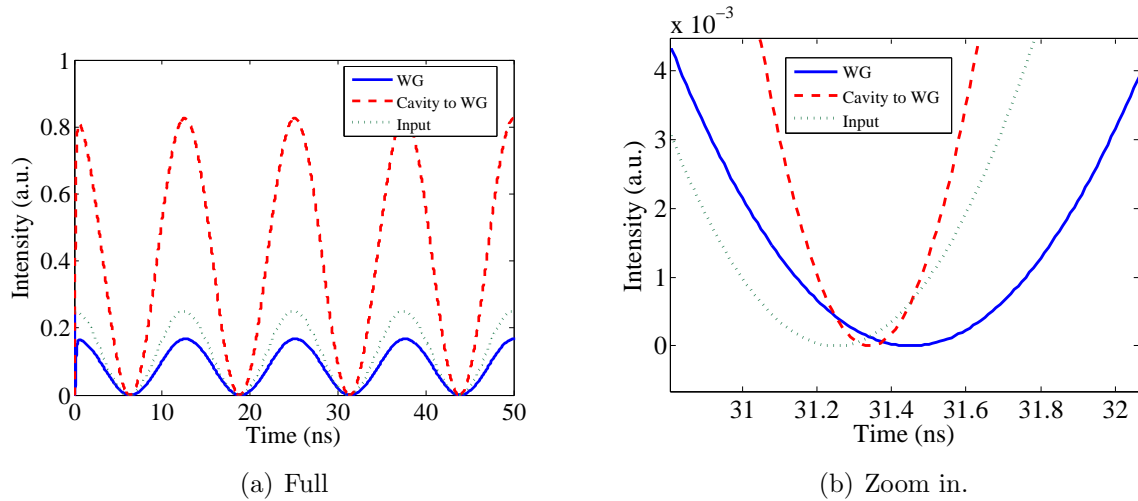


Fig. 3.14 Strongly overcoupled regime. $1/\tau_e = 10/\tau_o$. The waveguide signal has approximately 2ϕ phase shift.

(ii) When $\omega_m \tau \gg 1$

When the GHz modulation frequencies are used or when the ring down time, τ , is comparable to the modulation frequency, ω_m , even in the MHz range then the exact expressions, Eqs. (3.24)–(3.28), will apply. In this case for any condition of the undercoupled regime phase shift of the waveguide signal, θ , is always positive. For the weakly overcoupled regime θ is also positive however, for the medium to the strongly overcoupled regime, θ is negative. Figures 3.15, and 3.16 show this behavior. In particular, Figs. 3.15(a), and 3.16(a) show that the phase shifts (Figs. 3.15(b) and 3.16(b)) are calculated in the undercoupled and the overcoupled regimes, respectively.

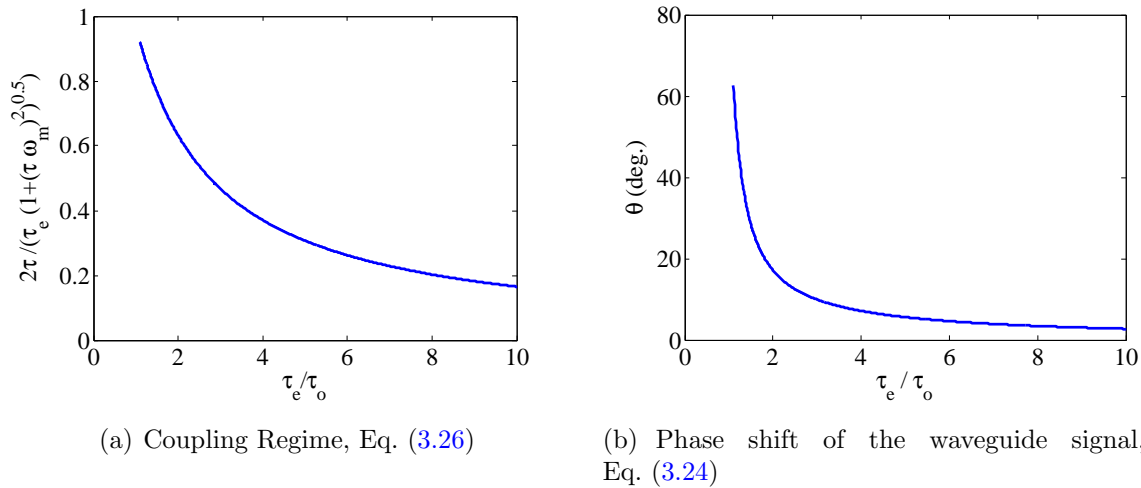


Fig. 3.15 Undercoupled regime. $\tau_o = 10^{-8}s$, $f_m = 40MHz$. From Eq. (3.26), the undercoupled regime requires, $\frac{\tau_e}{\tau_e \sqrt{1 + (\tau \omega_m)^2}} < 1$, as shown in Fig. 3.15(a).

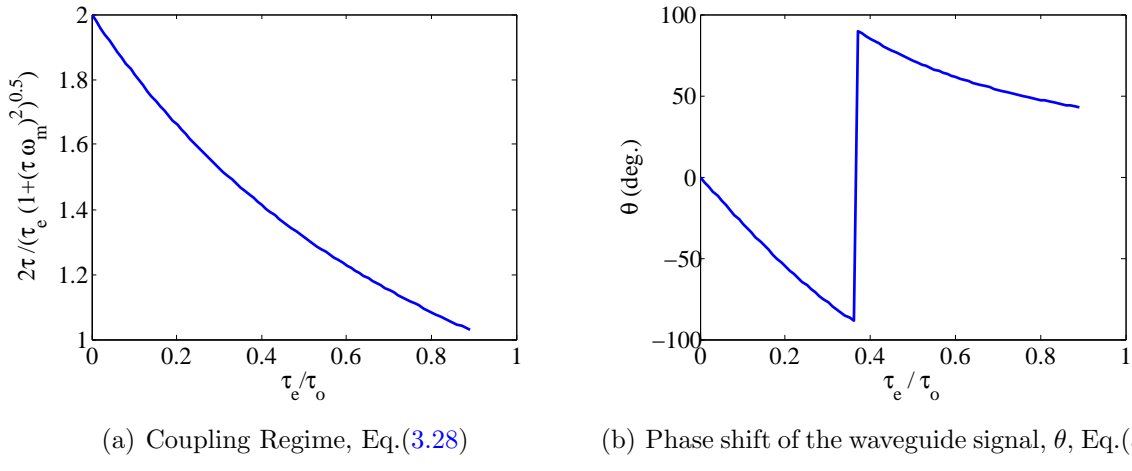


Fig. 3.16 Overcoupled regime. $\tau_o = 10^{-8}s$, $f_m = 40MHz$. From Eq. (3.28), the overcoupled regime requires, $\frac{2\tau}{\tau_e \sqrt{1 + (\tau \omega_m)^2}} > 1$, as shown in Fig. 3.16(a).

3.4.3 Experimental point of view

Although Eqs. (3.20), (3.21), (3.24), and (3.25) describe the PS-CRDS system completely but from the experimental point of view we know only phase shift (w.r.t input) of the waveguide signal, θ , its magnitude, $I_{wg} = E_{wg}^2$, magnitude of the input signal, $I_{ip} = E_{ip}^2$, and the modulation frequency, ω_m . This information is not sufficient to deduce the phase shift, ϕ , of the cavity signal, as we still do not know about the coupling lifetime, τ_e . In this section, we recast the PS-CRDS fundamental equations in the form of known quantities such that the phase shift, ϕ , can be deduced.

Rewriting the waveguide signal at the resonant wavelength,

$$E_{wg} = E_{ip} \cos(\omega_m t) - E_{cwg} \cos(\omega_m t + \phi), \quad (3.31)$$

where phase shift of the cavity field, ϕ , and field coupling back to the waveguide from the cavity, E_{cwg} , are defined in Eq. (3.20), and Eq. (3.21), respectively. Equation (3.31) can be represented as

$$E_{wg} = |E_{wg}| \cos(\omega_m t + \theta), \quad (3.32)$$

where magnitude and phase of Eq. (3.32) are

$$|E_{wg}| = \sqrt{E_{ip}^2 - 2E_{ip}E_{cwg} \cos \phi + E_{cwg}^2}, \quad (3.33)$$

$$\tan \theta = \frac{-E_{cwg} \sin \phi}{E_{ip} - E_{cwg} \cos \phi}. \quad (3.34)$$

It should be noted that Eqs. (3.33) and (3.34) are identical to Eqs. (3.25) and (3.24), respectively.

The intensity of the waveguide signal at the resonant wavelength is

$$I_{wg} = |E_{wg}|^2 \cos^2(\omega_m t + \theta) = I_{wg} \left(\frac{1}{2} + \frac{\cos(2\omega_m t + 2\theta)}{2} \right). \quad (3.35)$$

Experimentally, we measure the following:³.

- Magnitude of the input signal (waveguide signal at the non-resonant wavelength), i.e., $I_{ip} = |E_{ip}|^2$.
- Magnitude of the waveguide signal, i.e., $I_{wg} = |E_{wg}|^2$ at the resonant wavelength.
- Phase shift, θ , of the waveguide signal

Therefore, rewriting Eq. (3.33), and Eq. (3.34) in the form of known quantities (i.e., measured ones),

$$I_{wg} = I_{ip} - 2\sqrt{I_{ip}}E_{cwg} \cos \phi + E_{cwg}^2, \quad (3.36)$$

$$\tan \theta = \frac{-E_{cwg} \sin \phi}{\sqrt{I_{ip}} - E_{cwg} \cos \phi}. \quad (3.37)$$

Equations (3.36), and (3.37) represent two equations with the two unknowns, i.e., the field coupled to the waveguide from the cavity, E_{cwg} , and the phase shift of the cavity field, ϕ . We solve this system for two cases:

Case 1: Small angle approximation ($\sin \phi \approx \phi$)

This case is applicable where small ring down times are involved. After solving Eqs. (3.36), and (3.37) for the approximation, $\sin \phi \approx \phi$, we get two solutions, one for the positive θ

³Experimentally, we measure I_{wg} and 2θ at $2\omega_m$ (modulation frequency of the input signal). In real experiments, frequency displayed on the clock or function generator is basically $2\omega/2\pi$

(can represent the undercoupled or the overcoupled regime, see Section 3.4.2) and the other one for the negative θ (always represents the overcoupled regime, see Section 3.4.2). For a positively detected phase shift of the waveguide signal, $+\theta$, we have,

$$\phi_{+\theta} = \frac{\tan \theta}{1 - \sqrt{\frac{I_{ip}}{I_{wg} \cos^2 \theta}}}, \quad (3.38)$$

$$E_{cwg_{+\theta}} = \sqrt{I_{ip}} - \sqrt{I_{wg}} \cos \theta. \quad (3.39)$$

For a negatively detected phase shift of the waveguide signal, $-\theta$, we have,

$$\phi_{-\theta} = \frac{\tan \theta}{1 + \sqrt{\frac{I_{ip}}{I_{wg} \cos^2 \theta}}}, \quad (3.40)$$

$$E_{cwg_{-\theta}} = \sqrt{I_{ip}} + \sqrt{I_{wg}} \cos \theta. \quad (3.41)$$

Case 2: Exact

This case is applicable for any condition. Again, solving Eqs. (3.36), and (3.37) yields two solutions. For a positively detected phase shift of the waveguide signal, $+\theta$, we have,

$$\phi_{+\theta} = -\cos^{-1} \left[\sqrt{\frac{I_{ip}(I_{ip} + I_{wg}) + I_{wg}(-3I_{ip} + I_{wg}) \cos^2 \theta - 2I_{wg} \cos^3 \theta \tan^2 \theta \sqrt{I_{ip}I_{wg}}}{I_{ip}^2 + I_{wg}^2 - 2I_{ip}I_{wg} \cos 2\theta}} \right]. \quad (3.42)$$

For a negatively detected phase shift of the waveguide signal, $-\theta$, we have,

$$\phi_{-\theta} = -\cos^{-1} \left[\sqrt{\frac{I_{ip}(I_{ip} + I_{wg}) + I_{wg}(-3I_{ip} + I_{wg}) \cos^2 \theta + 2I_{wg} \cos^3 \theta \tan^2 \theta \sqrt{I_{ip}I_{wg}}}{I_{ip}^2 + I_{wg}^2 - 2I_{ip}I_{wg} \cos 2\theta}} \right], \quad (3.43)$$

where the underbrace indicates the only difference between Eqs. (3.42), and (3.43). The corresponding fields coupled to the waveguide from the cavity are

$$E_{cwg+\theta} = \frac{1}{8\sqrt{I_{ip}I_{wg}}(-I_{wg} + I_{ip}\sec^2\theta)} \csc^2\theta \sec^2\theta$$

$$\sqrt{\frac{I_{ip}(I_{ip} + I_{wg}) + I_{wg}(-3I_{ip} + I_{wg})\cos^2\theta - 2\cos^4\theta\sqrt{I_{ip}I_{wg}^3\sec^2\theta\tan^4\theta}}{I_{ip}^2 + I_{wg}^2 - 2I_{ip}I_{wg}\cos 2\theta}}$$

$$(2I_{ip}I_{wg}(2I_{ip} + I_{wg}) + 3(-I_{ip} + I_{wg})\sqrt{I_{ip}I_{wg}^3\sec^2\theta\tan^4\theta} - 4\cos 2\theta)$$

$$(I_{ip}I_{wg}(I_{ip} + I_{wg}) + I_{ip}\sqrt{I_{ip}I_{wg}^3\sec^2\theta\tan^4\theta} - I_{wg}\sqrt{I_{ip}I_{wg}^3\sec^2\theta\tan^4\theta})$$

$$+ \cos 4\theta (2I_{ip}I_{wg}^2 - I_{ip}\sqrt{I_{ip}I_{wg}^3\sec^2\theta\tan^4\theta}$$

$$+ I_{wg}\sqrt{I_{ip}I_{wg}^3\sec^2\theta\tan^4\theta}) , \quad (3.44)$$

$$E_{cwg-\theta} = \frac{1}{8\sqrt{I_{ip}I_{wg}}(-I_{wg} + I_{ip}\sec^2\theta)} \csc^2\theta \sec^2\theta$$

$$\sqrt{\frac{I_{ip}(I_{ip} + I_{wg}) + I_{wg}(-3I_{ip} + I_{wg})\cos^2\theta + 2\cos^4\theta\sqrt{I_{ip}I_{wg}^3\sec^2\theta\tan^4\theta}}{I_{ip}^2 + I_{wg}^2 - 2I_{ip}I_{wg}\cos 2\theta}}$$

$$(2I_{ip}I_{wg}(2I_{ip} + I_{wg}) - 3(-I_{ip} + I_{wg})\sqrt{I_{ip}I_{wg}^3\sec^2\theta\tan^4\theta} + 4\cos 2\theta)$$

$$(-I_{ip}I_{wg}(I_{ip} + I_{wg}) + I_{ip}\sqrt{I_{ip}I_{wg}^3\sec^2\theta\tan^4\theta} - I_{wg}\sqrt{I_{ip}I_{wg}^3\sec^2\theta\tan^4\theta})$$

$$+ \cos 4\theta (2I_{ip}I_{wg}^2 + I_{ip}\sqrt{I_{ip}I_{wg}^3\sec^2\theta\tan^4\theta}$$

$$- I_{wg}\sqrt{I_{ip}I_{wg}^3\sec^2\theta\tan^4\theta}) , \quad (3.45)$$

where the underbraces indicate the only differences between Eqs. (3.44), and (3.45).

3.4.4 Intensity independence

The results for phase shift of the cavity signal are independent of the intensity terms. This fact is proved in the following.

From Eq. (3.36),

$$I_{wg} = I_{ip} - 2\sqrt{I_{ip}I_{cwg}}\cos\phi + I_{cwg}, \quad (3.46)$$

and from Eq. (3.21),

$$I_{cwg} = \left(\frac{2\tau}{\tau_e \sqrt{1 + (\tau\omega_m)^2}} \right)^2 I_{ip} = \alpha I_{ip}, \quad (3.47)$$

where α is a constant given by,

$$\alpha = \left(\frac{2\tau}{\tau_e \sqrt{1 + (\tau\omega_m)^2}} \right)^2. \quad (3.48)$$

Substituting Eq. (3.47) in Eq. (3.46) results in

$$I_{wg} = I_{ip} (1 - 2\sqrt{\alpha} \cos \phi + \alpha) = \alpha_u I_{ip}, \quad (3.49)$$

where α_u is a constant given by,

$$\alpha_u = (1 - 2\sqrt{\alpha} \cos \phi + \alpha), \quad (3.50)$$

i.e., intensity of the waveguide signal is of the form, $I_{wg} = \alpha_u I_{ip}$. Now If we revisit Eqs. (3.38), (3.40), (3.42), and (3.43), we can see clearly that all the intensity terms cancel out. Hence, the results for the phase shift of the cavity signal are independent of the intensity terms.

3.4.5 Validation for the equations

In this section, we validate the equations developed in the previous sections both numerically and experimentally.

Numerical validation

Figures 3.17, and 3.18 show comparison of the coupled mode equations, the approximate and the exact expressions developed in the previous sections. As expected the exact expressions, to be used in experiments, give identical results as that of the fundamental PS-CRDS coupled mode equations. However, the approximate expressions also give fairly accurate results for $\phi < 10^\circ$. We can also see that, as expected, the phase shift and hence the quality factor in the overcoupled regime is lower than that of the undercoupled regime.

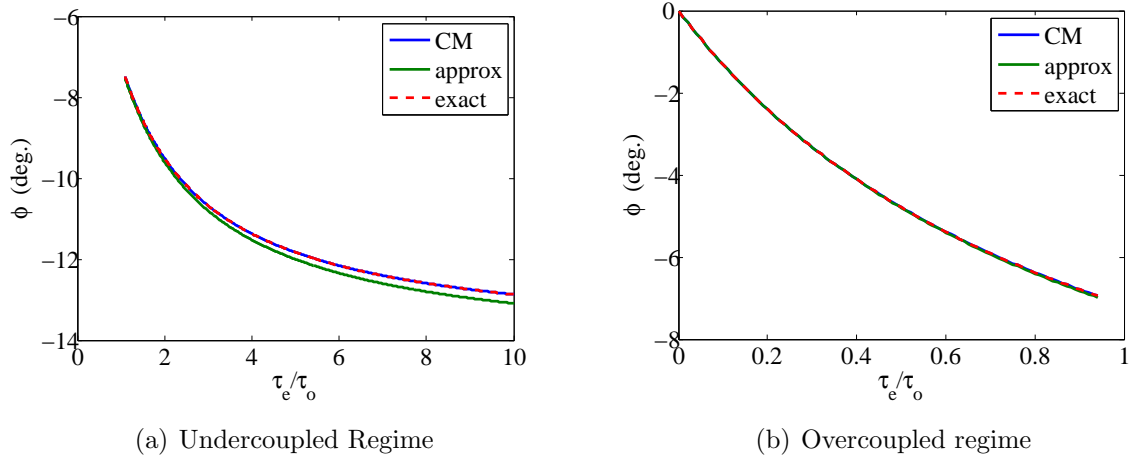


Fig. 3.17 Comparison of the PS-CRDS coupled mode equations (CM), the small angle approximation equations and the exact equations, $\tau_o = 10^{-9}s$, $f_m = 40MHz$.

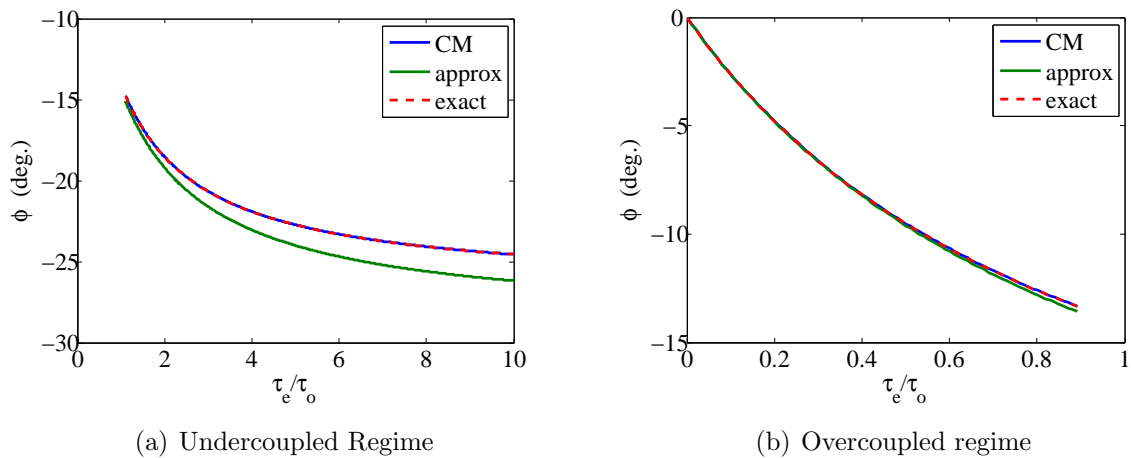


Fig. 3.18 Comparison of the PS-CRDS coupled mode equations (CM), the small angle approximation equations and the exact equations, $\tau_o = 2 \times 10^{-9}s$, $f_m = 40MHz$.

Experimental validation

We describe the detailed experimental setup in Chapters 4 and 7. Briefly, a 1530nm laser is used to couple the light in a toroidal microcavity via a tapered optical fiber. The phase shift of the waveguide signal, θ , and its magnitude, I_{wg} are measured at the resonant wavelength. The coupling regimes are obtained by varying the air gap between the cavity and the tapered fiber. The summary of the measurement procedure is given below:

- a. Divide the measured phase shift of the waveguide signal, 2θ , by 2
- b. Measure the waveguide signal intensity, I_{wg} , at the resonant wavelength
- c. Measure the waveguide signal intensity, I_{ip} , at the non-resonant wavelength
- d. If the measured θ is positive, use Eqs. (3.38) or (3.42), to calculate ϕ
- e. If the measured θ is negative, use Eqs. (3.40) or (3.43), to calculate ϕ
- f. Insert the calculated ϕ in $\tan \phi = -\frac{\omega_m}{2}\tau$ to calculate the ring down time, τ . (Note that ω is divided by 2 because this equation is derived for the fields)

All of the above steps are single shot measurements from the experimental data.

In the following, we provide the results for a positively and a negatively detected phase shift, θ , of the waveguide signal.

Positively detected θ

A representative experimental result for a positively detected phase shift of the waveguide signal, $+\theta$, is shown in Fig. 3.19. Since this data is taken when the tapered fiber is far from the resonator, we can say that the data corresponds to the undecoupled regime [70, 71]. The quality factor obtained by using the exact expression is in agreement with the one obtained by fitting the resonant peak to a Lorentzian curve.

Negatively detected θ

A representative experimental result for a negatively detected phase shift of the waveguide signal, $-\theta$, is shown in Fig. 3.20. A negative θ always represents the overcoupled regime. Here, it is obtained by bringing the taper close enough to the cavity without touching

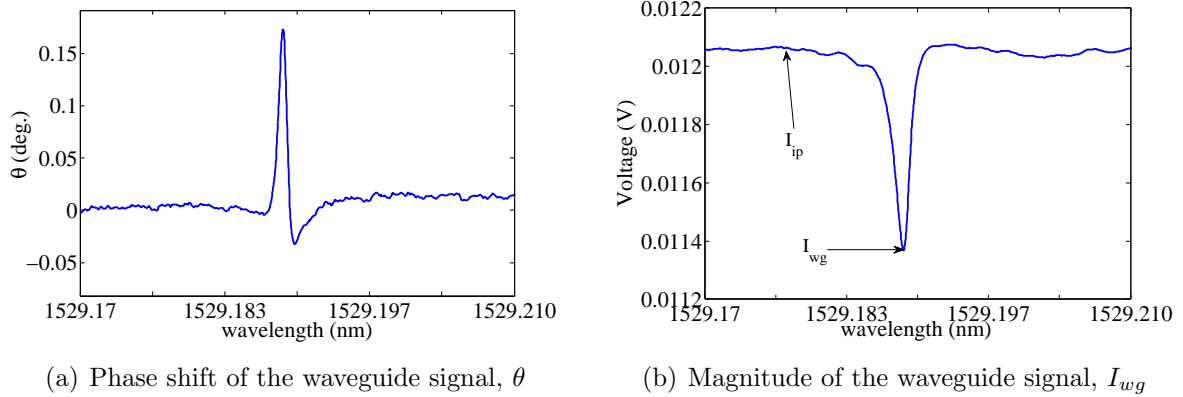


Fig. 3.19 Representative undercoupled regime data

it [70, 71]. Again, the quality factor obtained by using the exact expression is in agreement with the one obtained by fitting the resonant peak to a Lorentzian curve.

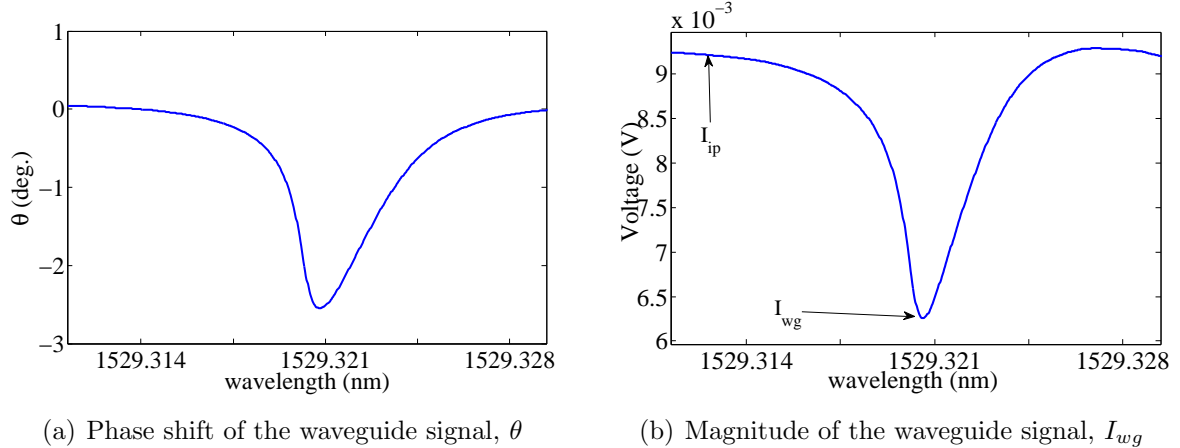


Fig. 3.20 Representative overcoupled regime data

3.5 Conclusions

With the aid of coupled mode theory, we can understand the cavity-waveguide system for continuous wave, pulse (CRDS), and sinusoidal (PS-CRDS) input sources. Specifically for the PS-CRDS system, we derive the mathematical expressions for phase shift and magnitude of the cavity signal and the waveguide signal. We study the PS-CRDS expressions for the various conditions involving the ring down time and the modulation frequency. We also show that, in contrast to the CW case, the coupling regimes in the PS-CRDS system have different conditions, e.g., the critically coupled regime in the PS-CRDS system has a non zero waveguide signal, whereas in the CW case the waveguide signal is zero. We also show that the calculation of phase shift of the cavity field is independent of any of the intensity terms. Finally, we validate the derived expressions numerically and experimentally.

Chapter 4

Simultaneous measurement of quality factor and wavelength shift by phase shift microcavity ring down spectroscopy

¹The last two decades have seen tremendous progress towards the development of real time, label free and miniature optical biosensors. Researchers have demonstrated numerous techniques based on the surface plasmon resonance, interferometers, waveguides, microcavities, optical fibers, and photonic crystals [7]. Among these different approaches, the large photon lifetime (Quality factor of $10^6 - 10^9$) of microcavities makes them a strong candidate for ultrasensitive biosensing, as the circulating photons will sample a biodetection event many times. The first microcavity biosensor was demonstrated by Vollmer et. al [11] in 2002, in which they detected proteins by measuring change of the resonant wavelength of a microsphere as a function of the binding event. Since then researchers have transitioned the microcavity-based sensors towards diagnostics platforms and protein behavior detection [72, 28].

Until now, the majority of work using microcavity biosensors focused on correlating the change in the resonant wavelength to a biodetection event on the surface of the

¹This chapter has been published in M. Imran Cheema, Simin Mehrabani, Ahmad A. Hayat, Yves-Alain Peter, Andrea M. Armani and Andrew G. Kirk, "Simultaneous measurement of quality factor and wavelength shift by phase shift microcavity ring down spectroscopy", Optics Express 20, 9090-9098 (2012).

microcavity. However, the binding event will also influence the photon lifetime or the ring down time (and hence quality factor) of the microcavity [50]. Apart from few instances, where quality factors have been determined based upon linewidth measurements [73,17], researchers have not sought to measure this property, and thus important information about the biodetection event is lost. Moreover, in all configurations of the microcavity biosensors used so far, random intensity fluctuations of the laser source add noise into the final measurement and hence the overall performance of the biosensor is degraded [46,47]. These issues can be overcome by using the microcavity as the key component in a phase shift cavity ring down spectroscopy (PS-CRDS) measurement.

Cavity ring down spectroscopy (CRDS) was first demonstrated in 1984 by Anderson et. al [74] in which laser light was injected into a free space optical cavity and after reaching a predefined transmission level at the cavity output, the laser was switched off by using a Pockels cell. The decay rate of the output light was then correlated with reflectivity of the mirrors. In 1988, O’Keefe et. al [75] transformed CRDS into a sensing method by measuring the absorption of molecular oxygen filled in a free space optical cavity. Since that time, many variants of the original CRDS technique have been demonstrated, and now CRDS is a well established technique for absorption measurements in gaseous phase [64]. One of the major advantages of this technique is its insensitivity to the intensity fluctuations of the laser source, since the decay rate is measured instead of the absolute intensity of the ring down time signal [64]. However, in order to extract the decay rate, fitting algorithms are applied [76] to the ring down time signal, and as a result, a fit error is introduced in the final result. To overcome the fitting error whilst remaining insensitive to the intensity fluctuations of the laser source, PS-CRDS can be used. This technique was first developed by Herbelin et.al [77] for measuring reflectance of mirrors and then later Englen et. al [63] successfully applied it to investigate the absorption of vibration states of molecular oxygen. In PS-CRDS, intensity modulated light is injected into the cavity which undergoes a phase change and decrease in modulation depth as it comes out of the cavity. Both of these parameters are related to the ring down time of the cavity.

With the success of CRDS in gaseous phase, the technique is also emerging as a new way for performing absorption measurements in the liquid phase [78] and for biosensing [79]. The first application of CRDS biosensing involved a resonator made of an optical fiber with couplers at its ends [80]. In this work, the researchers used taper section of the fiber as a sensing medium where the evanescent tail of the cavity modes interacted with the analyte

molecules. An alternative, inexpensive design is the use of fiber in a loop with a gap between the two ends for the insertion of a micro-fluidic chip. Loock et. al. applied PS-CRDS to the fiber loops to detect μM concentrations of chemicals in liquid samples [81]. However, fiber loop cavities have significantly lower quality factors than silica spheres or toroidal microcavities, resulting in significantly shorter photon lifetimes. Thus, by combining the advantages of PS-CRDS with an ultra-high-Q microcavity transducer, this sensing modality will be greatly improved. With this motivation, Barnes et.al [68] applied PS-CRDS to silica microspheres for determining their losses in air. To determine the ring down times in the transmission regime, they evaluated their derived waveguide phase shift expression at multiple modulation frequencies by using a linear fit to the experimental data (small angle approximation of their derived expression). The experimental scheme that was employed is not well-suited for biosensing application as it is not possible for that setup to track the quality factor or the resonant wavelength, as a function of a biodetection event, at multiple modulation frequencies. Therefore, the goal of our research is to show, 1) the application of PS-CRDS to microcavities in the liquid phase, and 2) to simultaneously track changes in the quality factor (ring down time) and the resonant wavelength shift as function of a biodetection event by PS-CRDS in a microcavity biosensor.

In our work, we used a bioconjugated [8] microtoroid optical resonator [18] to specifically detect unbinding of streptavidin (Fig. 4.1). We tracked both change in the Q and the resonant wavelength by using PS-CRDS and we found that the disassociation curves of biotin-streptavidin are in good agreement with the previously published results.

We now describe the rest of the chapter. We describe our experimental setup in Section 4.1. The quality factor is determined by using the experimental data in conjunction with the expressions developed in Chapter 3. The results are presented in Section 4.2. Finally, we conclude the chapter in Section 4.3.

4.1 Experimental Setup

In the conventional PS-CRDS experiments with the free space cavities, a locking technique, such as Pound-Drever-Hall [82] technique, is used for locking the laser frequency to the cavity mode. Such locking techniques can also be applied to microcavities [83]. However, locking the laser to the microcavity for biosensing means that information about the shift in resonant wavelength will not be measured; at the same time, if the locking technique is

not used, then the ring down time can not be measured because the microcavity resonance wavelength will shift due to the biodetection event. We have developed a novel experimental setup to overcome these difficulties. The experimental setup is shown in Fig. 4.1.

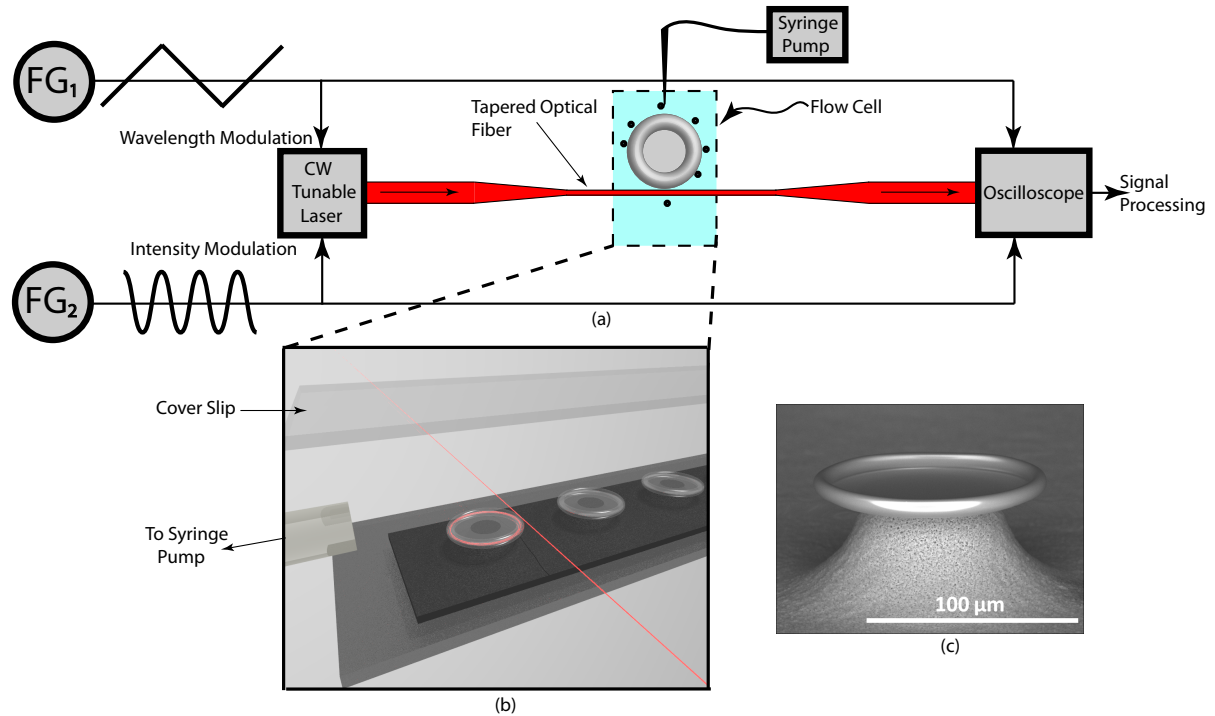


Fig. 4.1 (a) Experimental Setup, FG - Function Generator (b) Magnified view of the microacquarium. A cover slip is placed 2mm (approx.) above the microcavity chip holder with a spacer to form the microacquarium. (c) Scanning electron microscope (SEM) image of the microtoroidal cavity

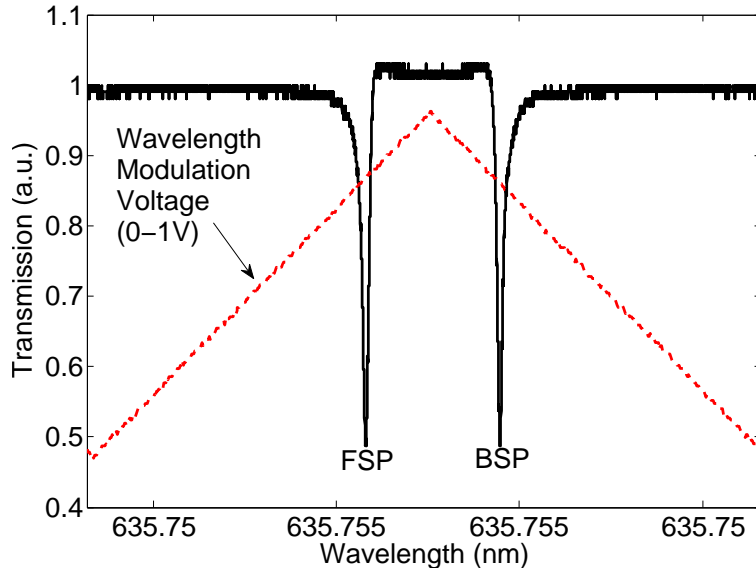
A tapered fiber [84] is used to evanescently couple the light from the CW tunable laser centered at 633nm into the microtoroidal cavity with a 105 μm (6 μm) major (minor) diameter. The microtoroidal cavity is covalently functionlized with biotin [8]. The bioconjugated cavity is immersed in the PBS microacquarium to ensure the biostability and bioactivity of the biotin layer and subsequent protein, and the setup is then flushed with 6mL of fresh PBS. We then inject 1nM of streptavidin via syringe pump at the rate of 50 $\mu L/min$. After 7 minutes of the injection, we switch off the syringe pump and start tracking the change in the Q and the resonant wavelength. As shown in previous works [71], the quality factor is very dependent on the coupled input power, which is controlled by the coupling gap. Therefore, all measurements are performed in contact at the same position

on the cavity. We also monitor depth of the peaks to make sure that it remains constant throughout the recording phase. Therefore, changes in coupled input power do not play a role in the change in the Q [71] in the present measurements. The procedure of tracking the ring down time and the resonant wavelength involves the following process:

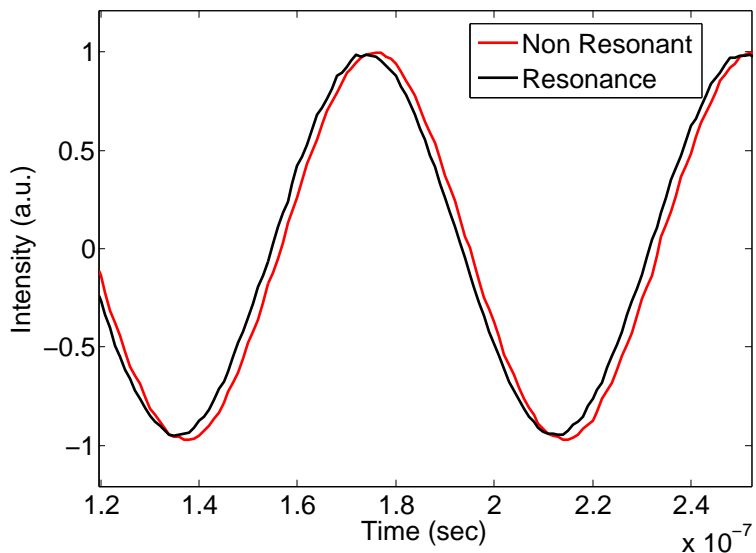
A function generator (FG_1) with triangular wave output (100mHz, 1V peak-to-peak) continuously modulates the wavelength of a tunable laser (New Focus, Velocity Scan 633nm tunable laser) to generate the resonant peaks as shown in Fig. 4.2a. The peaks are labelled as Forward Scanning Peaks (FSP), and Backward Scanning Peaks (BSP). After locating a resonant peak, a second function generator (FG_2) is switched on (13MHz, 4V peak-to-peak) to provide sinusoidal modulation of the laser intensity. After switching on both of the function generators, the phase shift between a reference sinusoid (sinusoidal modulated intensity of the laser before coupling) and the sinusoid at the fiber output is continuously recorded. In such a scan, there will be phase shifts only at the resonant peaks (Fig. 4.3). The same values of the phase shifts at the FSP and BSP indicate that there is no difference in the FWHM widths of the two peaks and hence any nonlinear effects are negligible [85], an important consideration for the biosensing experiments. The values of the peaks are the phase shifts which correspond to the ring down time (and hence Q) and positions of the peaks correspond to the resonant wavelength (see Chapter 3). Both of them can easily be extracted by further signal processing of the captured data.

4.2 Results and discussion

The binding kinetics of the biotin-streptavidin system in association and disassociation phase can be approximated by an exponential curve for the resonant wavelength [86]. During the association phase, the resonant wavelength shifts towards the red and in the disassociation phase it shifts towards the blue [28]. The change in resonant wavelength during the disassociation of the streptavidin from the biotin are shown in Fig. 4.4 which is in excellent agreement with [28]. The change in Q during the disassociation phase is also shown which is following an increasing trend which makes sense as the binding and unbinding of the streptavidin will decrease and increase the overall quality factor of the microtoroid respectively. The error signal, which is recorded with the tapered optical fiber alone, is also shown in Fig. 4.5. The noise shown in Fig. 4.5 is significantly smaller than the signal shown in Fig. 4.3 with the minimum and maximum signal to noise ratios of



(a) Frequency domain measurements



(b) Time domain measurements

Fig. 4.2 Two types of measurements (a) Minimum of one of the resonant peak is tracked as function of the biodetection event (b) Phase shift experienced by the waveguide signal is tracked as a function of the biodetection event. With reference to Fig. (a), black sinusoid is extracted at the resonant peak.

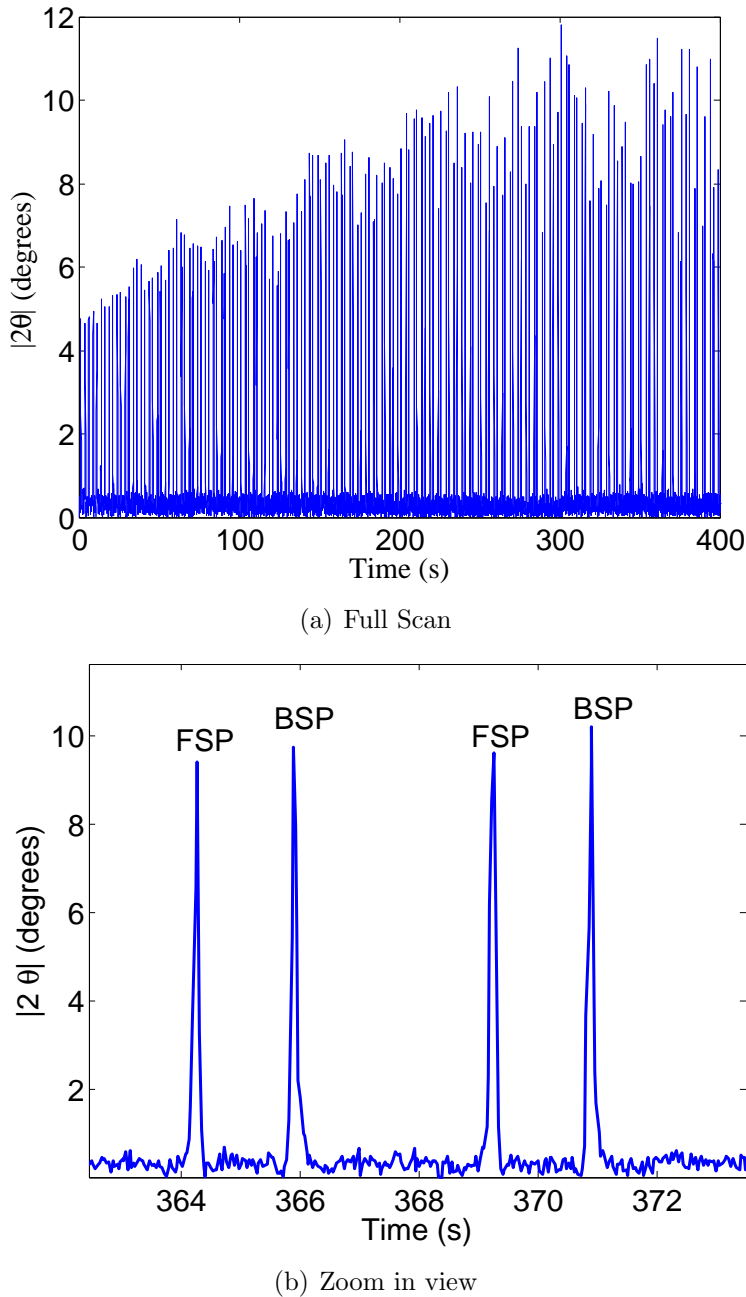


Fig. 4.3 Full scan with zoom in view of FSP and BSP (a) Continuous monitoring of phase shift of the waveguide signal (w.r.t FG₂ signal) as function of disassociation of the streptavidin from the biotin (b) Due to limitations of the computer speed, two FSPs and BSPs are separated by 5s respectively.

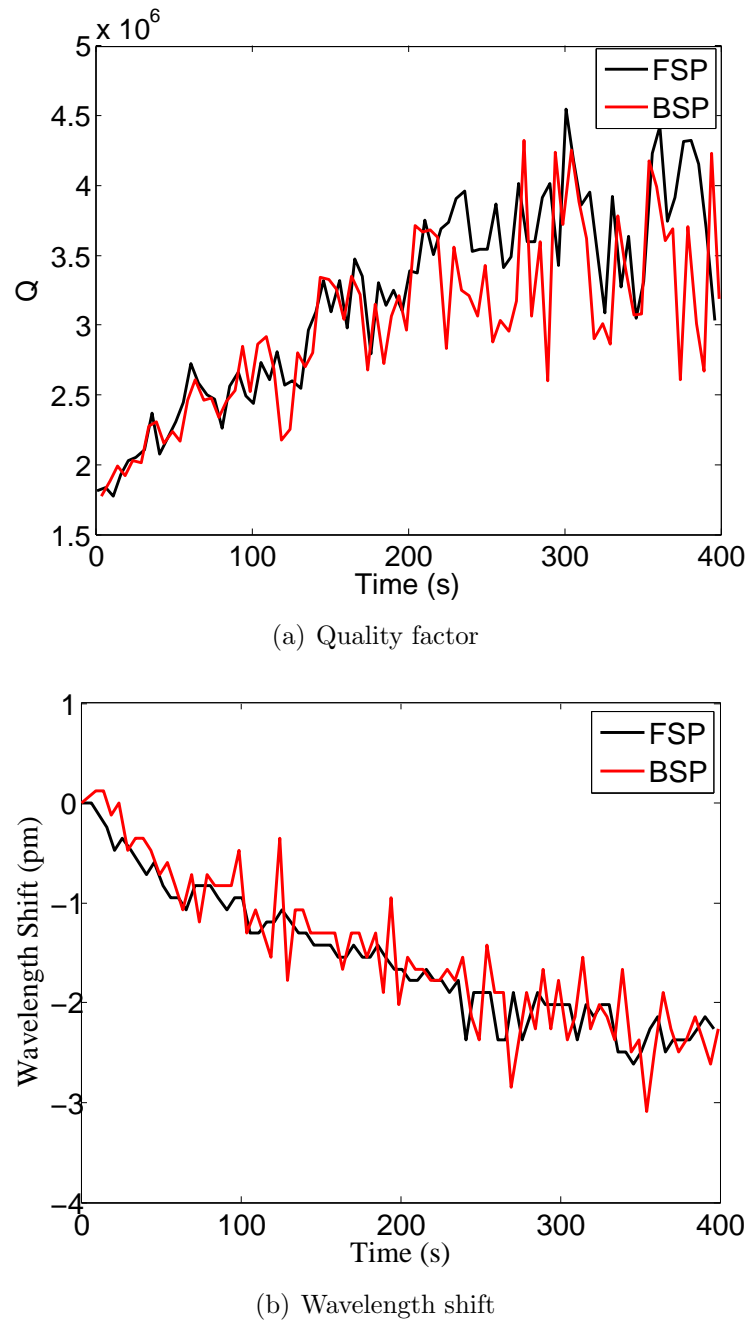


Fig. 4.4 Experimental parameters. The curves are not smooth because each data point is 5s apart on each curve, a limitation of the computer used in the experiment. In (b), negative values signify that the resonant wavelength is shifting towards blue

12dB and 15.8dB respectively. The noise in Q measurements corresponding to the error signal is 9×10^4 at the quality factor of 3.3×10^6 (Calculated by expressions developed in Chapter 3). The noise in wavelength measurements is around 30 fm at the quality factor of 3.3×10^6 (See Fig. 6.3b).

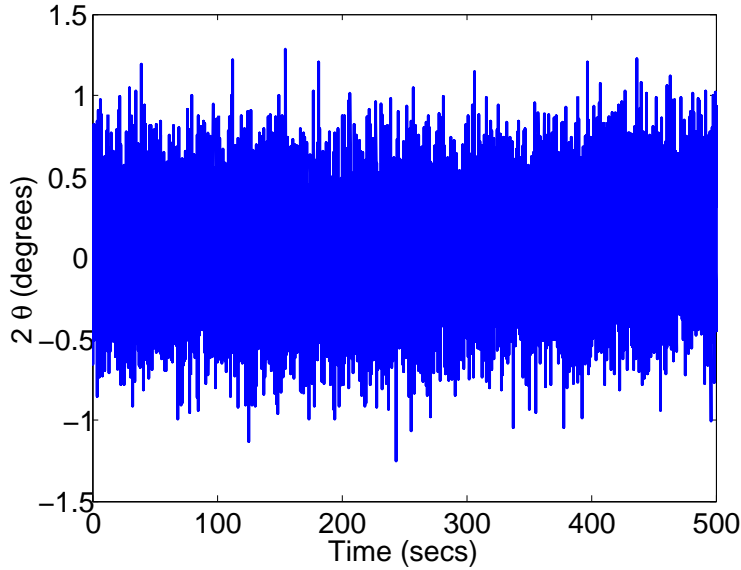


Fig. 4.5 A typical error signal for phase shift of the waveguide signal (w.r.t FG₂ signal), recorded by moving the taper far away from the microcavity. Mean: $\pm 0.2662^\circ$, Variance: 0.1076° , mode: $\pm 0.3387^\circ$. Based upon the detected signals, $\left(\frac{\text{Signal}}{\text{Noise}}\right)_{\min} = 12\text{dB}$, and $\left(\frac{\text{Signal}}{\text{Noise}}\right)_{\max} = 15.8\text{dB}$

The results indicate successful proof of the concept for the application of PS-CRDS to microcavities for biosensing. The PS-CRDS biosensor simultaneously tracks the Q and the resonant wavelength as a function of the biodetection event as opposed to its frequency domain counterpart which can only track the resonant wavelength in real time. The tracking of Q based upon the resonant peak requires non-linear fitting algorithms and would represent a significant challenge to real-time extraction of data. In our current setup, only tracking of the Q is free from noise due to the intensity fluctuations. However, the performance of the sensor can be improved by employing a lock-in amplifier which will reduce the error signal to 0.01° and hence the minimum and maximum signal to noise ratios will be improved to 27dB and 30dB respectively. In conventional wavelength shift based microcavity biosensors, minimum of the resonant wavelength is tracked by software. On

the other hand, by use of lock-in amplifier in PS-CRDS biosensor, accuracy of tracking of the resonant wavelength will be improved as compared to the frequency domain biosensor.

Since absorption of analytes influences the quality factor of the microtoroid, the PS-CRDS biosensor can also conduct such measurements in a faster (electronics) and an intensity noise free manner. On the other hand, absorption measurements [17, 31] in the wavelength shift based microcavity sensors (i.e., Q tracking based upon non-linear fitting algorithms) are slow (software) and carry noise not only due to the intensity fluctuations but also due to fitting of Lorentzian curves to the resonant peaks. Moreover, other noise mechanisms that are present in the wavelength shift based microcavity sensors, such as laser frequency jitter, conversion of FG_1 voltage to the wavelength [39], and shift in the resonant wavelength due to thermal fluctuations [37] are also minimized in the Q measurements. This observation is clear from the fact that these noise mechanisms will effect the location of the resonant peak whereas the Q measurements are independent of the peak's position.

CRDS with free space cavities is an emerging technique for liquid phase applications such as liquid chromatography [87, 88]. However, such devices suffer from scattering and reflection losses due to the placement of the liquid sample inside the cavity. In some cases [88], liquid is in contact with the mirrors which degrades the mirrors over a period of time. Moreover, different mirrors need to be employed to meet wavelength requirements in an experiment. The PS-CRDS sensor demonstrated in this work can overcome the above mentioned difficulties and has potential to offer a compact and sensitive solution for the liquid chromatography applications.

4.3 Conclusions

In summary, we have combined the advantages of CRDS (high noise immunity) and microcavities (high Q, low cost and compact) to develop a sensor that can simultaneously track the Q and the resonant wavelength as a function of a biodetection event. The sensor can also provide faster results for absorption measurements than its frequency domain counterpart. This work is also the first demonstration of applying PS-CRDS to microcavities for liquid phase applications. This PS-CRDS microcavity sensor has potential of finding wide applications not only in biosensing but also in analytical chemistry, pharmaceutical and agriculture sectors.

Chapter 5

Accurate determination of the quality factor and tunneling distance of axisymmetric resonators for biosensing applications

¹Microcavities are widely used in many applications such as biosensing, nonlinear processes, lasers and optomechanics. Most previously published work with microcavity biosensors has employed measurement of the change in resonant frequency of the sensor as a function of a biodetection event [5, 7] with only a few instances of using the quality factor as a sensing metric [10, 73, 17]. It has been shown that the quality factor of microcavities can be measured in the time domain using phase shift shift cavity ring down spectroscopy (PS-CRDS) [68]. This approach has recently been applied to biosensing applications [3]. In order to extend this work to ultra sensitive biosensing applications (e.g. determination of binding kinetics, detection of $pM - fM$ concentrations, and proteins, viruses etc), it is important to design a cavity with the optimum parameters for high sensitivity. One of the goals of the current work, is to rapidly estimate the quality factors of the microcavities with high accuracy to address these applications.

Whispering gallery mode (WGM) radiation occurs due to tunneling of photons

¹This chapter has been published in M. Cheema and A. Kirk, "Accurate determination of the quality factor and tunneling distance of axisymmetric resonators for biosensing applications," Opt. Express 21, 8724-8735 (2013).

through a potential barrier from the microcavity to a allowed wave propagation zone (see Fig. 5.1). The tunneling phenomenon has been utilized in various photonic devices such as photonic band gaps [89], super lattices [90] , and asymmetric cavities [91]. Recently Tomes et. al. [92] have performed remarkable experiments to image the tunneling process of axisymmetric microcavities. These experiments indicate that the tunneling phenomenon can be utilized for potential applications such as biosensing. However, to design the appropriate devices for a particular biosensing application, it is again necessary to accurately calculate the tunneling distance of axisymmetric microcavities. Another goal of our work is to address this issue.

In any modeling technique, reflections from boundaries of the computation domain are induced due to radiation produced by the whispering gallery modes (WGM) of a microcavity. For an accurate electromagnetic model, absorbing boundary conditions or perfectly matched layers (PML) are required to reduce these unwanted reflections. PML act as artificial boundaries that truncate the computation domain of open region scattering problems in the finite element method. There have been previous attempts to develop finite element models (FEM) of axisymmetric cavities which incorporate the PML. In 2005, Chinellato et al. [93] introduced a FEM model which was implemented in MATLAB. Whilst their model was capable of simulating the behavior of very small resonators ($< 3\mu m$) it was not adequate for resonators possessing the dimensions typically used in experiments. In 2009, Karl et al. [94] developed a 3D FEM model in JCMsuite for studying a micro-pillar cavity. However, this model does not consider the suppression of false solutions, a well known problem in finite element formulations [95,96]. Moreover, the quality factor of the modes was estimated by fitting the Lorentzian peak to the calculated spectrum of the cavity, thus introducing an extra approximation.

In 2007, Oxborrow [2] developed a FEM for open axisymmetric resonators in COMSOL without invoking any transverse mode approximation to Maxwell's equations, representing an advance on previous work [71,97]. In his work, he showed that the model could simulate resonators of arbitrary cross section in optical and microwave regimes, thus removing the size limitation in [93]. Another difference from [93] is in terms of suppression of false modes; Oxborrow used a simple penalty term in his master equation whereas Chinellato et al. used Nédélec edge and modified Lagrange nodal element functions to avoid the spurious modes. With Oxborrow's formulation in COMSOL, 3D rotationally symmetric problems are reduced to 2D and are solvable in seconds which is vast improvement over [93,94]. (For

further discussion and further comparison to other works see references [2, 98].)

The advantages of Oxborrow's model have made it a popular choice among researchers and it has been widely used in numerous research works e.g., [99, 100, 39, 101]. However in Oxborrow's model no PML was implemented and as a result the WGM quality factor could not be determined accurately. The quality factor due to the WGM radiation was estimated by placing a bound on its minimum and maximum possible values. These maximum and minimum values were determined by executing the model multiple times with different boundary conditions. Moreover, the model lacks the capability to estimate the quality factor of multiple modes simultaneously.

In order to provide accurate determination of the WGM quality factor, we have improved Oxborrow's model by modifying its master equation and implementing the PML along the boundaries of the computation domain. In the present work, geared towards sensing applications, we expand and refine the model presented in our earlier work [53]. Other researchers [102] have subsequently reported the inclusion of PML in Oxborrow's model for determining resonant frequencies and corresponding mode profiles of microring resonators but mathematical details have not been provided.

Our modified model does not have any of the drawbacks of Oxborrow's model. Moreover, we have computed the quality factors of all the modes without using any fitting algorithms as opposed to the approach taken in [94]. Furthermore, with the modified Oxborrow's method, tunneling distances can also be accurately extracted for microcavities of various shapes. In the present work, a simple expression for computing tunneling distance of microtoroidal cavities is also provided.

In our model, we treat the PML as an anisotropic absorber and implement it in the cylindrical coordinate system. Our model is applicable to any axisymmetric resonator geometry but due to the availability of analytical expressions for spherical resonators, we have validated the model by determining the quality factors and tunneling distances of a silica microsphere in air. We have found that our simulation results are in excellent agreement with the analytical results. We also apply our model to microtoroidal cavities immersed in liquid and show that our results are consistent with those obtained by experiments. The model is then used to determine the optimum parameters of a microtoroidal cavity sensor based upon phase shift cavity ring down spectroscopy.

The chapter is organized as follows. In Section 5.1, an improved FEM model is introduced by incorporating the PML. The optimal parameters of the PML are discussed

in Section 5.1.1. The analytical expressions of the quality factor and the tunneling distance of microspheres are presented in Section 5.1.3. These expressions are then used in Section 5.2.1 for comparing the modeling results. In the same Section, an empirical expression for tunneling distance of fundamental modes of a toroidal cavity is also provided. In Section 5.2.2, the model is validated experimentally by measuring the quality factors of the microtoroidal cavities in liquid. In Section 5.2.3, the model is validated numerically by running convergence test. In Section 5.3, we show that the model can be applied for sensing applications. In this section, we show that for a sensor, whose sensing metric is change in the quality factor, an optimum geometry exists for achieving maximum sensitivity. Finally, we conclude the chapter in Section 5.4.

5.1 Mathematical description

Applying Galerkin's method to the wave equation and after using the boundary conditions for open resonators, one can arrive at the FEM equation in the weak form [2]:

$$\int_V \left(\vec{\nabla} \times \vec{H}^* \right) \epsilon^{-1} \left(\vec{\nabla} \times \vec{H} \right) - \alpha (\vec{\nabla} \cdot \vec{H}^*) (\vec{\nabla} \cdot \vec{H}) + c^{-2} \vec{H}^* \cdot \frac{\partial^2 \vec{H}}{\partial t^2} \right) dV = 0, \quad (5.1)$$

where \vec{H} represents the magnetic field of the resonator and $\vec{\tilde{H}}$ represents the test magnetic field, an essential component of the weak form. The second term of Eq. (5.1) represents a penalty term to suppress false solutions. None of the field components will depend upon the azimuthal coordinate ϕ in the axisymmetric resonators, resulting in reduction of the 3D problem to a 2D problem.

5.1.1 Perfectly matched layer formulation

A PML can be treated as an anisotropic absorber in which the diagonal permittivity and permeability tensors of the absorber are modified according to Eq. (5.2) [103].

$$\bar{\epsilon} = \epsilon \bar{\Lambda}, \bar{\mu} = \mu \bar{\Lambda}. \quad (5.2)$$

The radial and axial modification factors are represented by $\bar{\Lambda}$, which is given by

Eq. (5.3)

$$\bar{\Lambda} = \left(\frac{\tilde{r}}{r} \right) \left(\frac{s_z}{s_r} \right) \hat{r} + \left(\frac{r}{\tilde{r}} \right) (s_z s_r) \hat{\phi} + \left(\frac{\tilde{r}}{r} \right) \left(\frac{s_r}{s_z} \right) \hat{z}, \quad (5.3)$$

where

$$s_r = \begin{cases} n_{medium} & 0 \leq r \leq r_{pml}, \\ n_{medium} - jG \left(\frac{r - r_{pml}}{t_{rpml}} \right)^N & r > r_{pml}, \end{cases} \quad (5.4)$$

$$s_z = \begin{cases} n_{medium} - jG \left(\frac{z_{lpml} - z}{t_{lpml}} \right)^N & z < z_{lpml}, \\ n_{medium} & z_{lpml} \leq z \leq z_{upml}, \\ n_{medium} - jG \left(\frac{z - z_{upml}}{t_{upml}} \right)^N & z > z_{upml}, \end{cases} \quad (5.5)$$

$$\tilde{r} = \begin{cases} r & 0 \leq r \leq r_{pml}, \\ r - jG \left(\frac{(r - r_{pml})^{N+1}}{(N+1)t_{pml}^N} \right) & r > r_{pml}, \end{cases} \quad (5.6)$$

where t_{rpml} , t_{upml} , t_{lpml} are the PML thicknesses in the radial, $+z$ and $-z$ directions respectively and r_{pml} , z_{upml} , z_{lpml} are the locations of the start of PML in the radial, $+z$ and $-z$ directions respectively. n_{medium} is refractive index of the medium, N is order of the PML, and G is a positive integer.

In the PML expressions (s_r, s_z, \tilde{r}) , the imaginary component contributes to the attenuation of waves in the PML but at the same time, due to the discrete nature of the FEM mesh, a large imaginary component will introduce reflections at the interface between the PML and the medium. In order to determine the optimal value for the imaginary component, we have investigated linear, quadratic, and cubic PML of different thicknesses for various values of G by running many simulations for various sphere diameters. To deduce the optimum values of the parameters, we then compared the simulation results for Q_{WGM} of spherical cavities with the analytical ones. The simulation results show that a linear (i.e. $N = 1$), and $\lambda/4$ thick PML with a G value of 5 is optimum. We have also used these optimum values for the simulations of the microtoroidal cavities. The location of PML is also important to obtain accurate results. The radial PML should be greater than the tunneling distance (t) of the microcavity and the z PML should be greater than FWHM (w_z) of WGM along the z axis. After running series of simulations we find the

following as optimum values (w.r.t. $(r, z) = (0, 0)$, see Fig. 5.1):

$$r_{pml} \geq 6t, \quad (5.7)$$

$$z_{(u,l)pml} \geq |5.5w_z|. \quad (5.8)$$

5.1.2 Finite element method equation with perfectly matched layer

In order to incorporate the PML, we have reformulated Eq. (5.1) in the following way:

$$\int_V \left((\vec{\nabla} \times \vec{H}^*) \bar{\epsilon}^{-1} (\vec{\nabla} \times \vec{H}) - \alpha (\vec{\nabla} \cdot \vec{H}^*) (\vec{\nabla} \cdot \vec{H}) + c^{-2} \vec{H}^* \cdot \bar{\mu} \cdot \frac{\partial^2 \vec{H}}{\partial t^2} \right) dV = 0. \quad (5.9)$$

By casting Eq. (5.9) into the FEM software COMSOL, a full vectorial finite element model of a silica sphere in air can be obtained. By using the eigenvalue solver in COMSOL, resonant frequencies (f_r) of all the modes can easily be determined. Quality factor due to the WGM radiation can be calculated as [2]:

$$Q_{wgm} = \frac{\Re(f_r)}{2\Im(f_r)}. \quad (5.10)$$

5.1.3 Analytical expressions of the spherical resonator

Quality factor

The quality factor due to WGM radiation losses in a spherical microcavity can be written as [104]:

$$Q_{wgm} = \frac{1}{2} \left(m + \frac{1}{2} \right) p^{1-2M} (p^2 - 1)^{\frac{1}{2}} e^{2T_m}, \quad m \gg 1, \quad (5.11)$$

where

m = azimuthal mode number,

$$p^2 = \frac{\epsilon_{sphere}}{\epsilon_{medium}}, \quad (5.12)$$

$$T_m = \left(m + \frac{1}{2} \right) (m_l - \tanh(m_l)), \quad (5.13)$$

$$m_l = \cosh^{-1} \left(p \left(1 - \frac{1}{m + \frac{1}{2}} \left(t_q^0 \beta + \frac{p^{1-2M}}{\sqrt{(p^2 - 1)}} \right) \right)^{-1} \right), \quad (5.14)$$

$$\beta = \left(\frac{1}{2} \left(m + \frac{1}{2} \right) \right)^{\frac{1}{3}}, \quad (5.15)$$

$$M = \begin{cases} 0 & \text{For TE,} \\ 1 & \text{For TM,} \end{cases} \quad (5.16)$$

t_q^0 is the q^{th} root of equation $F_{airy}(t_q^0) = 0$

m can be calculated using the characteristic equation for WGM frequencies [105]:

$$p^{1-2M} \frac{j'_m[pk_0a]}{j_m[pk_0a]} = \frac{h'_m[k_0a]}{h_m[k_0a]}, \quad (5.17)$$

where j , h are Bessel functions, k_0 is the wave number ($2\pi/\lambda_0$), and a is the radius of a microsphere.

It should be noted that Eq. (5.11) is an asymptotic solution for the Q_{wgm} of the spherical resonator which requires $m \gg 1$, however the error is less than 1% for $m \geq 19$ [106]. In our comparison for the analytical results, we have applied Eq. (5.11) to silica spheres with mode numbers (m) ranging from 25 – 80.

Tunneling distance

The Schrodinger equation for a microsphere for a fundamental mode can be written in radial coordinates (r) as [107]:

$$-\frac{d^2\Psi_r}{dr^2} + V_r \Psi_r = E \Psi_r, \quad (5.18)$$

where $E = k^2$ is the total energy and Ψ_r is a position probability function of a photon. The potential (V_r) is given by

$$V_r = k^2(1 - p_r^2) + \frac{m(m+1)}{r^2}, \quad (5.19)$$

where p_r is ratio of relative permittivity of the sphere and the surrounding medium in radial coordinates. Analytically, tunneling distance for a fundamental mode of a microsphere can be written as [107]:

$$t = \frac{\sqrt{m(m+1)}}{k} - a. \quad (5.20)$$

5.2 Results

5.2.1 Comparison between simulations and analytical results

Figure 5.1 shows a fundamental TE mode of a silica spherical cavity in air.

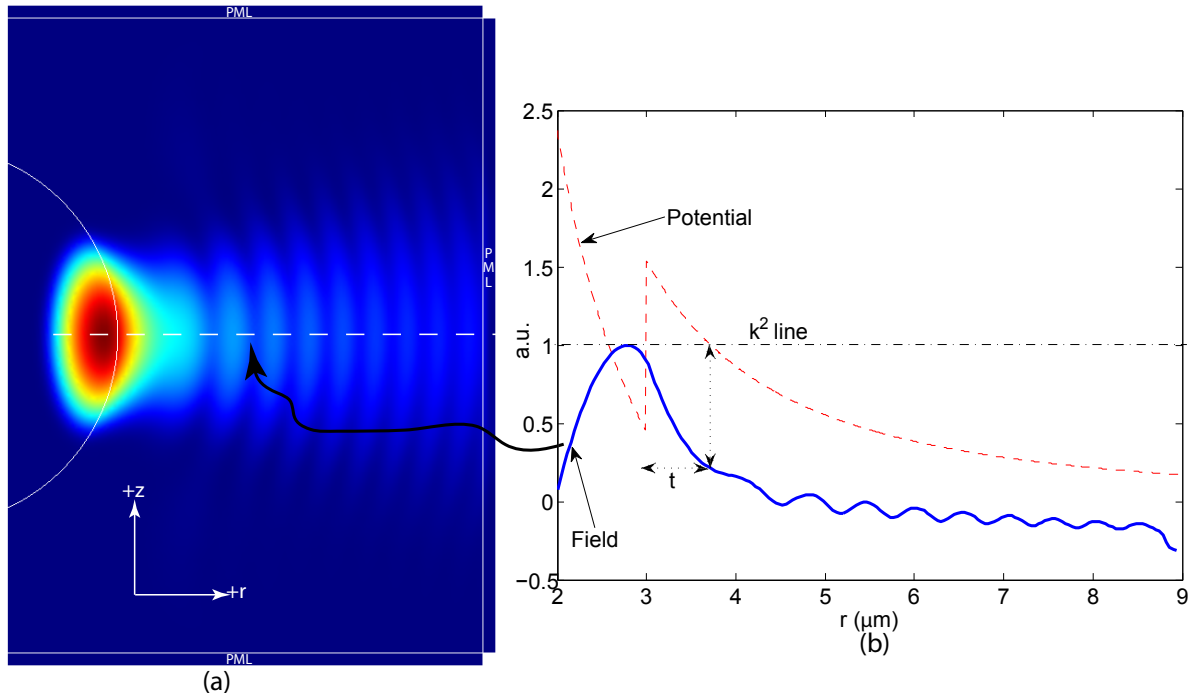


Fig. 5.1 a) (False color) Logarithmic intensity of the fundamental TE mode of a silica microsphere in air. b) Normalized field intensity along the dashed line shown in (a). Dotted curve shows potential, normalized to k^2 . Tunneling distance is indicated by t .

We have plotted the quality factor due to the fundamental TE whispering gallery mode radiation for various sphere diameters at 1550nm. Similar results are obtained for the TM mode. Figure 5.2 shows the comparison of the FEM simulation results and results obtained by using analytical expressions presented in Section 5.1.3. We have also calculated

the minimum and maximum Q_{wgm} values using Oxborrow's model [2] for each sphere diameter and those are also shown in Fig. 5.2. It can be seen that the new model provides a more accurate estimate than Oxborrow's model, and returns a single value of Q rather than a range of values. The slight difference between the analytical and the FEM values is attributed to discretization of the computation domain. The accuracy will improve with finer mesh elements (see Section 5.2.3). It can also be seen that Oxborrow's bounds do not always straddle the analytical solutions. One of the possible reasons for this discrepancy may be that while deriving these bounds, in order to simplify the derivation, Oxborrow assumes that the modes are transverse but in reality the modes of these axisymmetric resonators are not perfectly transverse [2].

Figure 5.3 shows the results for tunneling distance for both microsphere and microtoroidal cavities. An empirical relation for the tunneling distance for fundamental modes of the microtoroidal cavities can be extracted from the simulation results and is given as:

$$t = \frac{\sqrt{m(m+1)}}{k} - \frac{D+d}{2}, \quad (5.21)$$

where D and d are major and minor diameter of a microtoroid and are shown in Fig. 5.3(b). The tunneling distance results are also in agreement with experimental results presented in [92].

5.2.2 Comparison between simulations and experimental results

Our model is also appropriate for other axisymmetric resonators where analytical solutions are not available. In order to test this, we have used our FEM model to determine the total quality factor of microtoroidal cavities [18] and have compared the simulation results with experimental measurement of the quality factor. Mathematically the total quality factor (Q_{total}) can be represented by:

$$Q_{total} = \frac{1}{Q_{wgm}^{-1} + Q_{surroundings}^{-1} + Q_{material}^{-1} + Q_{coupling}^{-1}}. \quad (5.22)$$

In order to validate the model with reasonable range of quality factors, it is necessary to ensure suitable experimental conditions in which to observe these quality factors. We have performed the experiments with the microtoroids immersed in ethanol (refractive index: 1.3538 at 1550nm [108]) by using the fluidic cell described in [3]. We have preferred

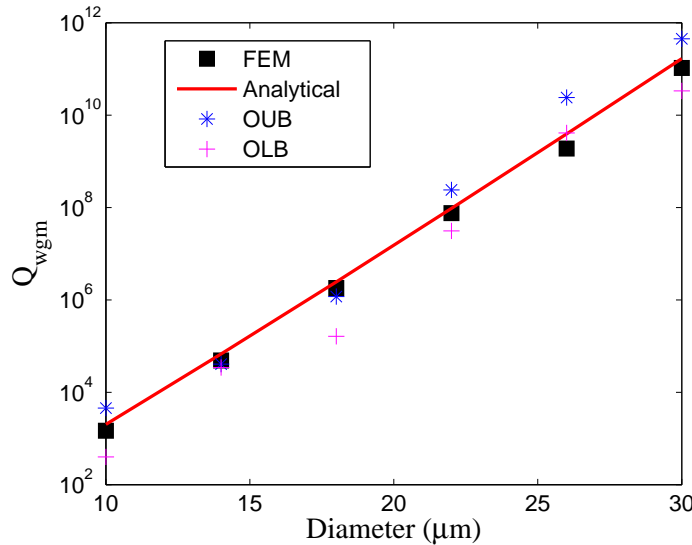
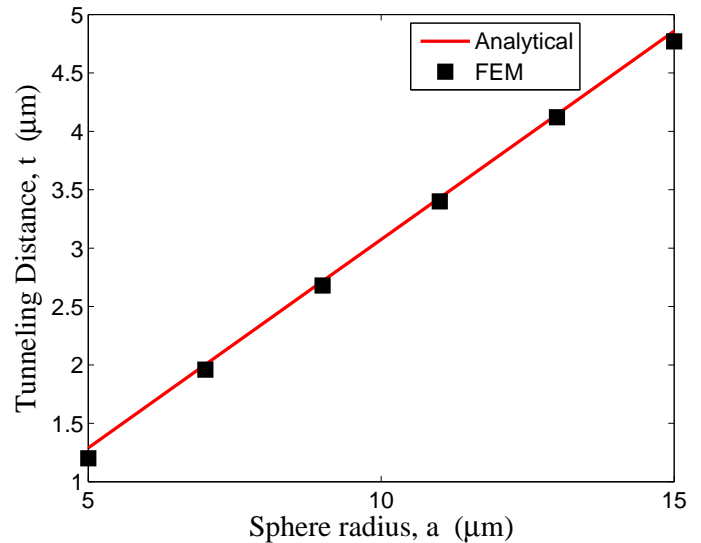


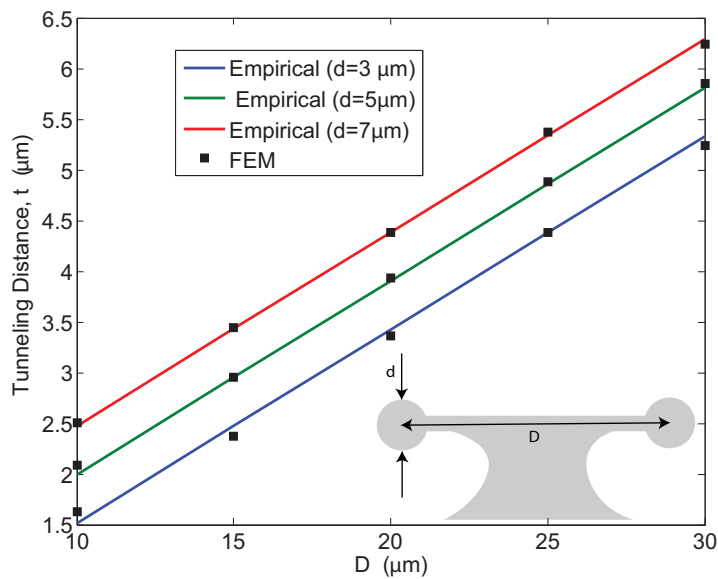
Fig. 5.2 Modeling results at 1550nm. WGM Quality factors for various silica sphere diameters of fundamental TE mode. OUB and OLB represent upper and lower bounds that are calculated by using Oxborrow's model [2].

ethanol over water as ethanol not only provides low refractive index contrast between the silica cavity and the surroundings but also has low absorption as compared to water at 1550nm [109]. This will allow us to select a wide range of microtoroidal cavities whose Q_{total} is mainly limited by the Q_{wgm} .

A broadband source (peak wavelength:1530nm) is used to couple the light into microtoroids via a tapered optical fiber (taper waist: $\leq 1\mu m$). The resonant peaks are observed on a high resolution optical spectrum analyzer (Apex AP 2443B, resolution: 0.16pm) and quality factor is determined by Lorentz curve fitting of the peaks ($Q = \lambda/\Delta\lambda$). The tapered fiber is positioned (using 10nm resolution nanostages) along the equator of the cavity to couple light into fundamental transverse modes. It is ensured that the tapered fiber does not touch the cavity during the measurements. In order to minimize the effect of $Q_{coupling}$ on Q_{total} , the power at the peak wavelength of the source is set around $-48dBm$ (Optical spectrum analyzer sensitivity: $-70dBm$) and all the measurements are taken in highly undercoupled regime. The comparison between simulation and experimental results is shown in Fig. 5.4. Sources of error in the comparison include small amount of coupled power, discretization of the computation domain, and slight variation between simulated and experimental dimensions of microcavities.



(a) Microsphere



(b) Microtoroid

Fig. 5.3 Modeling results at 1550nm. Tunneling distance of a fundamental TE mode as a function of the microcavity geometries. Inset of Fig. 5.3(b) shows the cross section of a microtoroidal cavity.

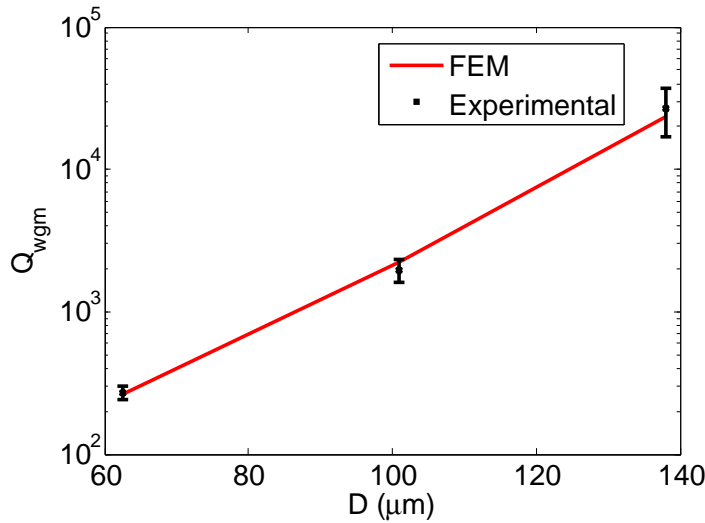


Fig. 5.4 Comparison between the modeling and the experimental results. WGM Quality factors of fundamental TM mode for various silica microtoroidal cavity diameters immersed in ethanol. Minor diameter d of each cavity is slightly different and is around $5\mu m \pm 1\mu m$. The experimental quality factors are determined by Lorentz curve fitting of the resonant peaks ($Q = \lambda/\Delta\lambda$) where $\lambda \approx 1530nm$.

5.2.3 Computational speed and numerical accuracy

For the results presented in Figs. 5.1-5.4, we have used the quadratic Lagrange elements of triangular shape with average element size (longest edge) of $0.3\mu m$ and the number of degrees of freedom of order 10^5 . As an example, a microtoroidal cavity model (Computation domain size: $25\mu m \times 16\mu m$, $D = 30\mu m$, $d = 5\mu m$) with the aforementioned statistics took only $35s$ to find the first 20 eigenvalues on a quad core 64 bit operating system PC.

To check numerical accuracy of the model, we have run a convergence test. Figure 5.5 shows the plot of relative error ($E_r = (Q_{FEM} - Q_{exact})/Q_{exact}$) as a function of the degrees of freedom (DOF) of our model. The DOF is related to the number of mesh elements, and the basis functions used in the FEM solver. Convergence of the solution is of order 2 which is expected for the Galerkin method for quadratic Lagrange elements [110]. It can be seen in the Fig. 5.5 that for small DOF, convergence rate is slower than the expected; the reason for this is the poor approximation of the curved boundary of the cavity by the coarsely meshed triangular elements.

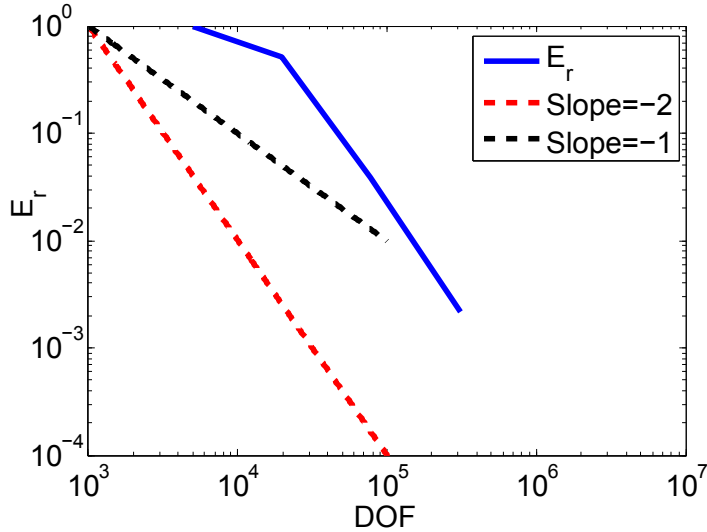


Fig. 5.5 Convergence plot for the quality factor determination of a microsphere.

5.3 Discussion and application to PS-CRDS microcavity sensor

The results presented in Section 5.2 show that our finite element model is both physically and numerically accurate. The quality factors for all the modes (fundamental and higher order modes) are also obtained by one single simulation rather than multiple simulations, which was the case for the original Oxborrow model. Moreover, no prior knowledge of any of the mode frequencies is required to obtain the quality factors. The model also gives fast results and without any fitting algorithms.

It should be noted that we have neglected dispersion for estimating the quality factors and tunneling distances. Whilst dispersion must be considered for very high Q applications where an equidistant modal spectrum is required [111], it has negligible effect for biosensing applications.

We have also applied our model to the PS-CRDS microtoroidal cavity sensor [3] in order to determine the optimum parameters for an application of refractometric sensing. In such a scheme, the microcavity is immersed into water and a small refractive index change (δn) is introduced. This change in refractive index will influence the Q_{total} of the cavity and can easily be measured via PS-CRDS microtoroidal cavity sensor [3]. Figure 5.6 shows the modeling results for change in Q_{total} of the cavity as a function of D . It can be clearly seen that to achieve maximum sensitivity there exists an optimum geometry for both $\lambda = 633nm$

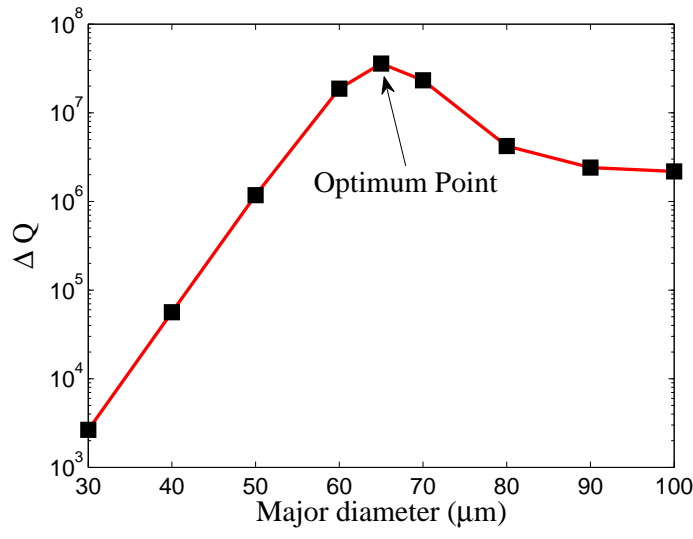
(Optimum D is $65\mu m$ at $Q = 2.95 \times 10^8$ and $\Delta Q = 3.58 \times 10^7$) and $\lambda = 1530nm$ (Optimum D is $90\mu m$ at $Q = 7.67 \times 10^4$ and $\Delta Q = 4.10 \times 10^3$). Due to high water absorption at $1530nm$, ΔQ is lower than the one at $633nm$. Since Q_{total} varies with the wavelength, the optimum geometry will be different for each of the wavelength. It should be noted that although here we show existence of an optimum geometry for refractometric sensors but the same optimization approach can be applied to various applications including adsorption of a monolayer on microcavities and sensing of proteins.

In order to understand that why an optimum geometry exists for a ΔQ measurement, we have plotted the individual terms of Eq. (5.22) as a function of the cavity geometry (Fig. 5.7). We have assumed $Q_{coupling} = 0$ which is a reasonable assumption as experimentally, contribution of $Q_{coupling}$ can be minimized by taking measurements at multiple input power levels [112]. Figure 5.7 shows that the optimum region exists close to the point of inflection of the Q_{total} curve. Results in Fig. 5.7 show that as diameter increases, the WGM is better confined within the microcavity (see Fig. 5.1(a)) and so Q_{wgm} is less influenced by the external environment, with the result that the total quality factor is limited by silica absorption. It should be noted that if small amount of coupling loss is considered then the optimum geometry will slightly shift towards larger diameters.

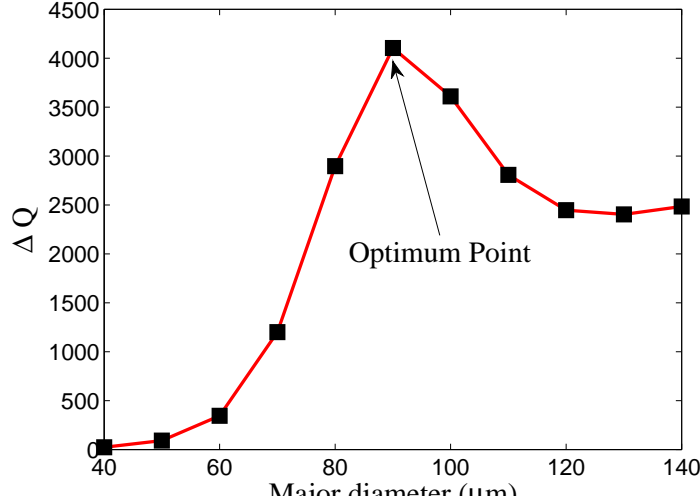
Currently the standard experimental approach to determine the total quality factor of a microcavity is either by cavity ring down spectroscopy or Lorentzian fitting of a resonant peak. However, tunneling distance is also related to WGM radiative quality factor i.e. large tunneling distance means high Q_{wgm} and vice versa. This suggests that with model provided here coupled with the experimental procedure outlined in [92], one can also extract Q_{wgm} even when Q_{total} is greater than 10^8 . Such a measurement can possibly open up the way to a new sensing method for microcavity sensors.

We have formulated an empirical expression (Eq. (5.21)) for the tunneling distance of the fundamental modes of microtoroids. This expression is inspired by the analytical expression for the tunneling distances of microspheres by treating the microtoroid as a sphere of diameter ($D + d$). This formulation is not surprising as these equations are true only for fundamental modes which lie along the equatorial region of a microcavity. However, this treatment will not be true for higher order modes (non equatorial modes) as the curvature for a microsphere of diameter $D + d$ will be quite different from a microtoroid with D and d as its dimensions (see Fig.5.3(b)).

In summary, our finite element model, without any approximation in its master

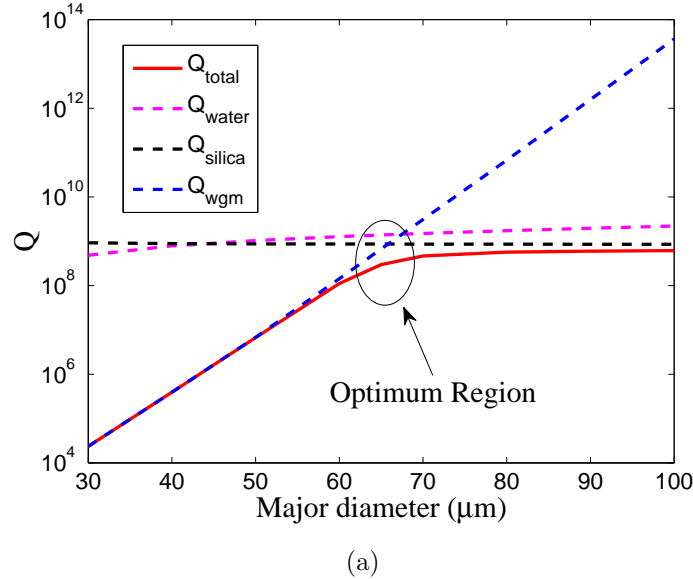


(a)

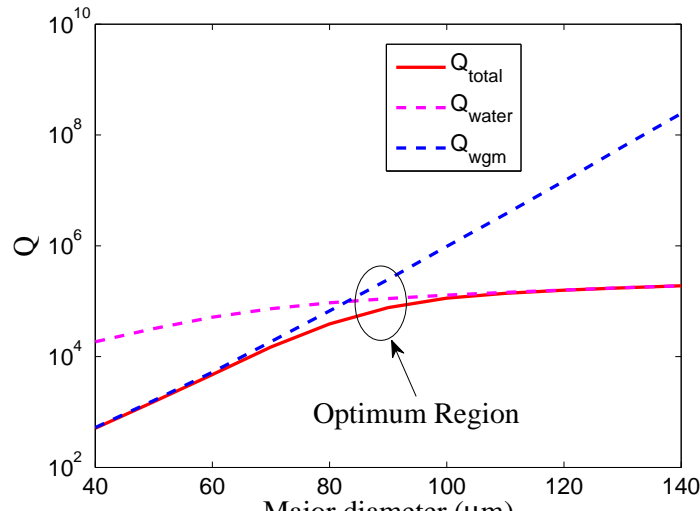


(b)

Fig. 5.6 Modeling results show the existence of an optimum geometry . Change in quality factor (ΔQ) of fundamental TM mode as a function of major diameter (D) of a microtoroidal cavity (minor diameter(d) = $6\mu\text{m}$) immersed in water. ΔQ shows the difference between Q_{total} for water and that measured when small refractive index change ($\delta n = 10^{-3}$) is introduced into the water. (a)Modeling results for $\lambda = 633\text{nm}$ (b)Modeling results for $\lambda = 1530\text{nm}$.



(a)



(b)

Fig. 5.7 Modeling results. Various quality factors (Eq. (5.22)) for fundamental TM mode involved in a microtoroidal cavity immersed in water as a function of D ($d = 6\mu\text{m}$). In the optimum region the Q_{wgm} is close to Q_{total} . (a) Modeling results at $\lambda = 633\text{nm}$. (b) Modeling results at $\lambda = 1530\text{nm}$. $Q_{\text{silica}} \approx 10^{11}$ (Silica has very low absorption at 1530nm) and is omitted in the figure to reduce the range in y-axis.

equation and coupled with a PML, not only gives accurate quality factors and tunneling distances, but can also determine the other important parameters (e.g. mode volumes) accurately for a wide range of applications based on axisymmetric microcavities such as biosensing, non-linear processes, and lasers.

5.4 Conclusions

We present an improved finite element model by utilizing perfectly matched layers. Our model is able to calculate quality factors of axisymmetric microcavities accurately and by single execution of the model whereas in the previous model the quality factor of a microcavity is estimated by running the model multiple times with different boundary conditions and with less accuracy as compared to our model. Moreover, our model can provide the quality factor of many modes in single execution while in the previous model knowledge of the mode frequency is required to calculate its quality factor and consequently the quality factor of only one mode can be estimated at one time. To the best of our knowledge, the microcavity geometry has never been optimized for a sensing application. Here, with help of the improved model (which is validated analytically, experimentally, and numerically) we show that an optimum geometry exists for a sensor whose sensing metric is change in the quality factor. We have also presented an accurate tunneling distance simulation for the axisymmetric cavities and formulated an empirical expression for tunneling distance of microtoroidal cavities. Since the tunneling distance has been experimentally measured for microcavities, we also suggest that this experimental setup in conjunction with our model can possibly open up a new sensing modality.

(For benefit of the microcavity community, our model is available for free download at [113]).

Chapter 6

Optimum parameters for achieving maximum signal to noise ratio in microcavity sensors: signal and noise analysis

Over the last few years, optical microcavities have been utilized in a wide range of biological and chemical sensing applications, ranging from the detection of cytokines in serum to heavy water detection. Typically, the sensing experiments involve measuring a change, in either the resonant wavelength, $\Delta\lambda$, or the quality factor, ΔQ , of the cavity, in response to a refractive index or optical absorption change [114, 21]. One motivation for pursuing the microcavity based sensors over alternative devices is their high quality factors (Q) or long photon lifetimes at well-defined resonant wavelengths. Additionally, because it is currently believed that when using the wavelength shift approach, the narrow linewidth inherent in higher Q devices enables smaller sensing events to be resolved; research has focused on maximizing the Q of the cavity [49]. However, without considering various noise mechanisms present in a microcavity sensor, it has been suggested, via simulations, that the noise in the wavelength measurements ($\Delta\lambda$) depends upon the Q of a microcavity [46, 47]. Therefore, we believe that the Q of a microcavity influences not only the signal, i.e., changes in the resonant wavelength, $\Delta\lambda$, or the quality factor, ΔQ , but also the noise in both of the signals. Because the signal to noise ratio (SNR) governs the overall performance of a

sensor system, the balance between the signal and the noise should be the focus of any optimization process.

One way for improving the signal to noise ratio (SNR) is to increase the magnitude of the signal. For the wavelength shift measurement approach, enhancement of the signal has been achieved by replacing the passive microcavity with a microlaser [34] or by using plasmonics in microcavities [36]. On the other hand, methods to increase the magnitude of the signal in the Q measurement technique have not yet been demonstrated. To increase the SNR by decreasing the noise, researchers have utilized interferometric techniques [39] for the wavelength measurements, and phase shift-cavity ring down spectroscopy [3] for the Q measurements. Here, without implementing the alternative schemes for either the signal enhancement or the noise reduction, we show that a microcavity sensor can achieve an optimum SNR by simply optimizing its dimensions and Q. Interestingly, the optimum Q is not the highest possible Q of the cavity.

It is important to note that, for a sensing application, there are various methods of measuring a change in Q or in wavelength. For example, the Q of a microcavity can be determined by either a linewidth measurement [17] or by using phase shift-cavity ring down spectroscopy [3]. Similarly, the wavelength can be tracked by either continuously scanning the laser across the resonance and tracking the minimum [11], or fixing the laser at a single frequency and monitoring the change in transmission [13]. In the present work, we focus on the linewidth change and the peak tracking approaches for the Q and the wavelength measurements, respectively. However, given the wide range of possible equipment configurations and techniques, all experimental methods are defined to enable the models to be generalized, not only to other device geometries, but also other testing methodologies.

Here, we use a microtoroidal cavity as a refractometric sensor. By performing a thorough signal and noise analysis for the sensor, we show that the optimum parameters exist for achieving a maximum SNR in microcavity sensors. We now describe the rest of the chapter. For measurements of the wavelength and the Q shifts due to a refractive index change in the sensor, we perform the signal analysis of the sensor by providing the modeling results in Section 6.1.1 followed by the experimental results in Section 6.1.2. In Section 6.2.1, we identify various noise sources in the sensor. In Section 6.2.2, we present the noise analysis of the sensor by providing the modeling and the experimental results for the wavelength shift measurements. In Section 6.2.3, we conduct the noise analysis (modeling results only) of the Q shift measurements based upon the Lorentz fit of the resonant peak.

In Section 6.2.4, we carry out the noise analysis of the Q shift measurements based upon the PS-CRDS. The signal to noise ratio results (modeling and experimental at 765nm) for the wavelength shift and the Q shift (Lorentz fit) measurements are presented in Section 6.3. Finally, we conclude the chapter in Section 6.4.

6.1 Signal analysis

In this section, we provide the modeling and the experimental results for the sensing signals, change in the wavelength, $\Delta\lambda$, and change in the quality factor, ΔQ , of a refractometric sensor based upon a microtoroidal cavity.

6.1.1 Modeling results

The simulations for the signals ($\Delta\lambda, \Delta Q$) are based upon the finite element model of a microtoroidal cavity immersed in distilled (DI) water [54] (Chapter 5). The constants, such as the refractive index of silica, water and the absorption of silica, water at 765nm, used in the simulations are either experimentally determined or taken from the published literature [115]. The change in wavelength, $\Delta\lambda$, and the change in quality factor, ΔQ , are determined for the fundamental TM mode of the cavity. The signals ($\Delta\lambda, \Delta Q$) are the cavity response to a refractive index (RI) change of 5×10^{-4} introduced into the DI water. These changes are recorded as a function of the Q of the cavity in the DI water (i.e., the Q, before introducing the RI change). The Q is varied by changing the major diameter (D) of the cavity while keeping the minor diameter constant ($d = 6\mu m$) [116]. The modeling results are shown in Fig. 6.1a, and Fig. 6.1c. From the results, it can be seen that the signal, $\Delta\lambda$, decreases with increase in the Q of the cavity. On the other hand, the signal, ΔQ , increases with increase in the Q of the cavity until it reaches a maximum point, at which it starts decreasing. The primary reason for this behavior, is that the overall Q of the cavity is limited by the absorption of the medium after a critical cavity size (here around major diameter of $75\mu m$) [54].

6.1.2 Experimental results

To experimentally verify the simulation results for the signals, a series of microtoroidal cavities with major diameters ranging from $67\mu m$ to $121\mu m$, and minor diameters of approximately $6\mu m$ are fabricated using the standard process [18]. The testing setup (similar

to the one presented in Section 2.4) consists of a tunable laser (Newport, TLB 6700, 765nm), that is coupled to the fundamental mode of the cavity via a tapered optical fiber. To enable high precision wavelength tracking, the laser is modulated linearly in wavelength using an external function generator (NI-PCI 5402). The resonant peak is recorded in the undercoupled regime using a photodetector (Thorlabs PDA36a) and an oscilloscope card (NI-PCI 5114). The minimum of the peak represents the resonant wavelength whereas the Q is determined by applying a nonlinear fitting algorithm to the peak (Lorentz fit, OriginLab).

Refractometric sensing is performed using a salt solution to trigger a RI change in the outside environment (DI water). The salt solution is prepared by mixing 1g of NaCl in 1L of DI water. At this concentration, this solution provides a change of RI of approximately $+5 \times 10^{-4}$ RIU from the DI water [117]. Briefly, to perform a experiment, the microtoroid is immersed in a flowcell (similar to [3]) containing the DI water. The initial resonant wavelength and the Q of the cavity are determined. The salt solution is then injected by a syringe pump at $100\mu L/min$. While the change in the resonant wavelength, $\Delta\lambda$, is tracked and recorded continuously, the change in quality factor, ΔQ is measured at the end of the experiment.

The experimental results are shown in Fig. 6.1b, and Fig. 6.1d. It is clear that they follow the same trend as the modeling results shown in Fig. 6.1a, and Fig. 6.1c. However, to achieve the same range of the quality factors as in the modeling results, it is necessary to use slightly different diameters. Moreover, the precise values for the sensing signals also differ from the modeling results. These differences can be attributed to various factors, e.g., the intrinsic Q degrades (one order of magnitude is possible) due to water adsorption on the cavity surface from the atmosphere after their fabrication [116](not captured in the simulations), the experimental results are for the loaded Q in the undercoupled regime whereas the modeling results are for the intrinsic Q of the cavity, the variation due to different minor diameters of the fabricated cavities used in the experiments, approximate estimate of the RI change introduced by the salt solution, taper jitter (a random process) affects the coupling and hence affects values of the desired measurements, and possible impurities on the cavity or in the salt solution can also degrade the Q of the cavity.

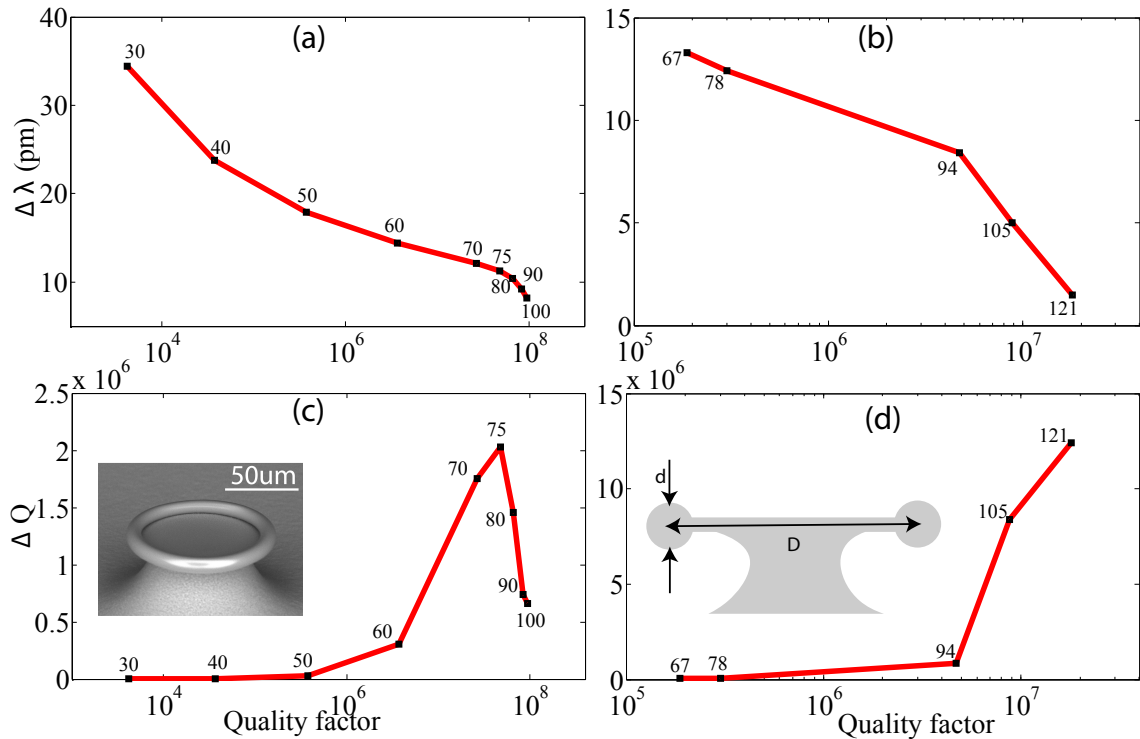


Fig. 6.1 Signal results at 765nm. (a), and (c) show the modeling results. (b), and (d) show the experimental results. The inset of (c) is a micrograph of a microtoroidal cavity and the inset of (d) shows its cross-section. The signals, $\Delta\lambda$, and ΔQ , in response to a RI change (5×10^{-4}), as a function of quality factor (intrinsic for modeling and loaded for experiments) of the cavity in the DI water. The resonant wavelength shifts towards red and the quality factor decreases with the increase of RI. The number at each data point represents the major diameter (D) of the cavity in microns. For the modeling results, minor diameter (d) is fixed at $6\mu\text{m}$, while for the experimental results, d is $6 \pm 1\mu\text{m}$.

6.2 Noise analysis

A proper noise analysis is an important aspect of any sensor. Apart from a few instances of brief analysis [46, 47], for the wavelength shift measurements only, a thorough treatment of noise in microcavity sensors has not been conducted to date. In this section, we provide a comprehensive noise analysis of (i) the resonant wavelength measurements based upon tracking of position of the minimum of a resonant peak, (ii) the quality factor measurements based upon the Lorentzian fit to a resonant peak, and (iii) the quality factor measurements based upon the PS-CRDS.

6.2.1 Noise sources

A variety of noise sources are present in the aforementioned measurements. They are shown in Fig. 6.2.

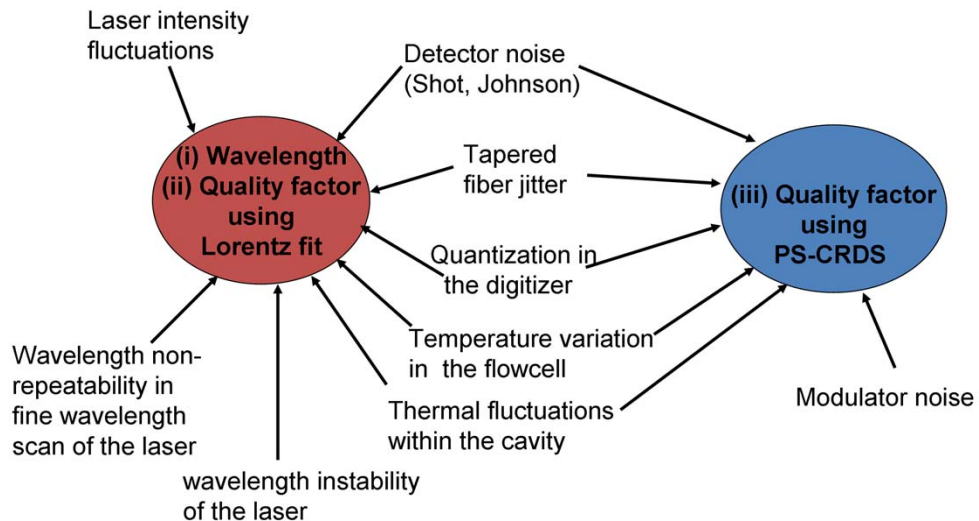


Fig. 6.2 Noise sources in the three measurement approaches.

We now briefly describe each of these noise sources.

i. *Relative intensity noise (RIN):*

RIN is defined as the relative intensity variation per unit bandwidth [118]. Due to RIN, the output intensity of a laser always shows variations. Various sources are responsible for these variations including ambient temperature fluctuations, acoustic vibrations,

and spontaneous emission in a lasing mode. The mean-squared noise current in a detector output due to the RIN of an input laser is given by Eq. (6.1) [118],

$$\overline{i_{RIN}^2} = \frac{(q\eta P)^2(RIN)B}{(h\nu)^2}, \quad (6.1)$$

where q is the charge of electron, η is the detector quantum efficiency, P is the average incident power, B is the detector bandwidth, h is the Planck's constant, and ν is the frequency of the incident wave.

Since the RIN of a laser induces intensity fluctuations in a resonant peak, the wavelength and the quality factor measurements based upon the resonant peak have noise due to this mechanism.

On the other hand, the quality factor measurements by using the PS-CRDS is insensitive to intensity fluctuations when implemented by the phase sensitive detection (PSD) technique [63](Also see Chapter 3, and Section 6.2.4).

ii. Wavelength instability of the laser:

A CW tunable diode laser always suffers from its wavelength instability. There can be various reasons for this instability including injection current fluctuations, ambient temperature and air pressure variations, acoustic noise, and mechanical vibrations.

iii. Wavelength non-repeatability in fine wavelength scan of the laser:

As explained in Chapter 2(Section 2.4) that in order to resolve a high Q resonant peak, an external function generator is required to induce a continuous wavelength modulation (the coarse tunability of the laser is a step function) of the laser over a smaller wavelength range. The function generator voltage provides an input to a piezo, attached to a tuning element (mirror or grating) [119], of the laser. The inherent hysteresis of the piezo and the function generator noise induces a non-repeatable behavior of the fine wavelength scan.

The above two noise mechanisms (ii and iii) directly affect a position of the minimum of a resonant peak and are present in the wavelength and the quality factor measurements based upon the resonant peak. On the other hand, as the implementation of the PS-CRDS is explained in Chapter 4 that although the phase shift is measured at the minimum of a resonant peak however, this measurement is independent of the

peak's minimum location. We reason as follows.

Suppose that we are performing the Q measurements with the experimental setup presented in Chapter 4. We always record the phase shift at the location of the resonant peak minimum in our experiments. Suppose that during the data recording, the minimum's location of the resonant peak shifts due to the wavelength instability noise mechanism. We will then record the phase shift at the “new” resonant peak minimum. (Recall that the equations presented in Chapter 3 are derived for a resonant wavelength and are independent of such a shift.) Since the phase shift (i.e., Q) tells us about the loss of a microcavity it will be minimally effected by the shift. Therefore, we can conclude that the PS-CRDS measurements are minimally effected by a shift in the peak's minimum location and hence are independent of the laser wavelength instability noise. We now provide a numerical example: Suppose $Q = \lambda/\Delta\lambda = 1530 \times 10^{-9}/10^{-12} = 1.53 \times 10^6$. With the wavelength noise, say the resonant peak minimum shifts by 10pm then the change in the Q is equal to 10, which is a negligible effect in the Q of 1.53×10^6 . On the other hand, the 10pm noise in the wavelength shift measurements can not be ignored.

iv. Modulator noise:

This noise mechanism is present in only PS-CRDS measurements. Modulation can introduce frequency chirping in the signal. However, in the electro-optic modulators this frequency chirping can be minimized. The modulator also produces higher order harmonics. These higher order harmonics can be minimized by carefully biasing the modulator. In the PSD detection, a lock-in amplifier extracts the phase information from the dc part of the signal [65] so the effect of the higher order harmonics is further minimized.

The following noise mechanisms are present in all the types of measurements:

v. Shot Noise:

A photodiode produces a current (charged carriers) proportional to an incident optical power. However, this current always has random fluctuations (shot noise) which occurs when the charged carriers have random generation and flow in the diode [118]. The mean-squared Shot noise current in a detector output is given by Eq. (6.2) [118],

$$\overline{i_s^2} = \frac{3q^2\eta PB}{h\nu}. \quad (6.2)$$

vi. Johnson Noise:

The voltage across a load resistance always has fluctuations. These fluctuations (Johnson noise) occur due to the random thermal motion of the charge carriers. The mean-squared noise current in detector output due to the Johnson noise is given by Eq. (6.3) [118],

$$\overline{i_s^2} = \frac{4kTB}{R_l}, \quad (6.3)$$

where k is the Boltzman constant, R_l is the load resistance, and T is the resistance temperature.

v. Tapered fiber jitter:

There is always a random motion associated with a tapered optical fiber, consequently, the gap between a microcavity and the taper varies randomly. The gap variation affects the coupling randomly which in turn affects the Q and the recording of the position of the resonant peak minimum. As a result noise is added to the final measurement. This noise depends upon the quality of the taper and can be minimized by removing the sag in the taper as much as possible without breaking it. This noise can be completely avoided by conducting the measurements with the taper in contact with the microcavity but at the same time the touching of the two degrades the overall Q of the microcavity. Therefore, there is always a tradeoff between avoiding this noise source and achieving a high Q of a microcavity. However, resonators with integrated waveguides such as microring resonators are immune to taper jitter.

vii. Quantization noise due to a digitizer:

Quantization is a process of mapping the values of a continuous waveform to a set of discrete levels. In other words, a value of the original analog waveform is represented by an approximate value in a digital format and thus adding the noise known as the quantization noise in the waveform recording. The discrete levels are determined by the number of bits of a digitizer. The quantization noise is given by Eq.(6.4) [120],

$$V_q = \frac{V_{sig}}{2^{bt}\sqrt{3}}, \quad (6.4)$$

where V_{sig} represents the input voltage to the scope, and bt represents the number of bits of the digitizer.

In our case, the quantization occurs from the detector to the digital oscilloscope for the measurements based upon a resonant peak and from the detector to the digital lock-in amplifier for the PS-CRDS measurements.

viii. *Thermal fluctuations within the cavity:*

Due to a higher Q and a smaller mode volume of microcavities, thermally induced nonlinearities can occur in them [121]. These nonlinearities can not only induce a shift in the resonant wavelength but can also distort the shape of the resonant peak. For sensing purposes, this noise mechanism is highly undesirable. However, this noise mechanism can be minimized by operating the microcavity at low power levels [121].

It is also possible to experimentally determine whether thermal fluctuations are influencing the measured results. In Chapter 4, we show that in an experiment we have a forward scanning peak, FSP, and a backward scanning peak, BSP. The thermally induced nonlinearities cause the FSP to expand and the BSP to contract [121]. If we obtain similar measurements from both of the FSP and the BSP (as obtained in Chapter 4) then this indicates that this noise mechanism is minimized.

ix. *Temperature variations in the flowcell:*

Any environmental temperature variations cause the temperature of a liquid in a flowcell to fluctuate. The liquid temperature fluctuations affect its refractive index and as a result both of the resonant wavelength and the quality factor measurements have a noise term. This noise term can be minimized by using a temperature controller, such as a TEC in the flowcell. Usually the measurements for the sensing signals are made within seconds, e.g., in this chapter, or within few minutes, e.g. in Chapter 4, hence this noise mechanism is not a dominant one for the applications considered in the present work. However, to demonstrate the sensing of smaller (or single) entities this noise mechanism has to be addressed adequately.

6.2.2 Noise in the wavelength measurements

In this section, we determine the noise in the wavelength measurements, both theoretically and experimentally. It is important to note that in the present work, low laser powers

are coupled into the cavity. Therefore, the thermal fluctuations within the resonator are minimized [121], allowing the noise due to this mechanism to be ignored. The noise due to the taper jitter (σ_{TJ}), the laser fine wavelength scan (σ_{FWS}), and the temperature fluctuations (σ_{TF}) of the flow cell are not theoretically calculated, and we comment on them, when discussing the experimental results.

Noise Modeling: By using specifications of the components used in our testing set-up, we estimate the voltages due to the quantization noise, RIN, detector Shot and Johnson noise (see Section 6.2.1). The wavelength instability is assumed to be of order of one line width ($1fm$) of the laser [37]. We use these noise voltages as input to the Monte Carlo simulations where we generate one thousand random copies of each noise corresponding to the estimated standard deviations (i.e., previously mentioned estimated voltages). These noise voltages are then superimposed on the Lorentzian resonant peak of the desired Q (i.e., generating one thousand Lorentzian peaks with the superimposed noise).

To estimate the total wavelength noise, σ_λ , at each Q , we first determine the minimum of each resonant peak superimposed with the noise, i.e., generating one thousand estimates of the resonant wavelength. We then fit one thousand minima to the normal probability density function (pdf), whose standard deviation gives σ_λ .

Experiments: Experimentally, the wavelength noise, at a given Q value, is measured by recording the minimum of the resonant peak continuously for 3 min. The recorded minima are then fitted to the Gaussian distribution to find the wavelength noise, σ_λ . To reduce the effect of the taper jitter, the measurements are made with the taper in contact with the cavity. Additionally, to maximize the Q of the cavity, the noise measurements are performed in air. The wavelength shift noise, σ_λ , results are shown in Fig. 6.3(a–c).

Based on the MC simulations, the wavelength shift noise is inversely related to the Q of the cavity (Fig. 6.3(a)). It can also be seen in Fig. 6.3(b), if the initial assumption of a $1fm$ wavelength instability noise is increased to $19fm$, the agreement between the model and the experimental data improves significantly. The experimental results can be fit to an equation of the form

$$\sigma_\lambda(fm) = \sigma_L + a_1 Q^{-b_1}, \quad (6.5)$$

where $\sigma_L = 19fm$, $a_1 = 2.31 \times 10^8$, and $b_1 = 1.116$. The results indicate that for a cavity with a $Q > 10^6$, the wavelength instability of the laser becomes the dominant noise

mechanism, and the noise due to the fine wavelength scan, a type of wavelength instability noise, is possibly in the range of 19 fm .

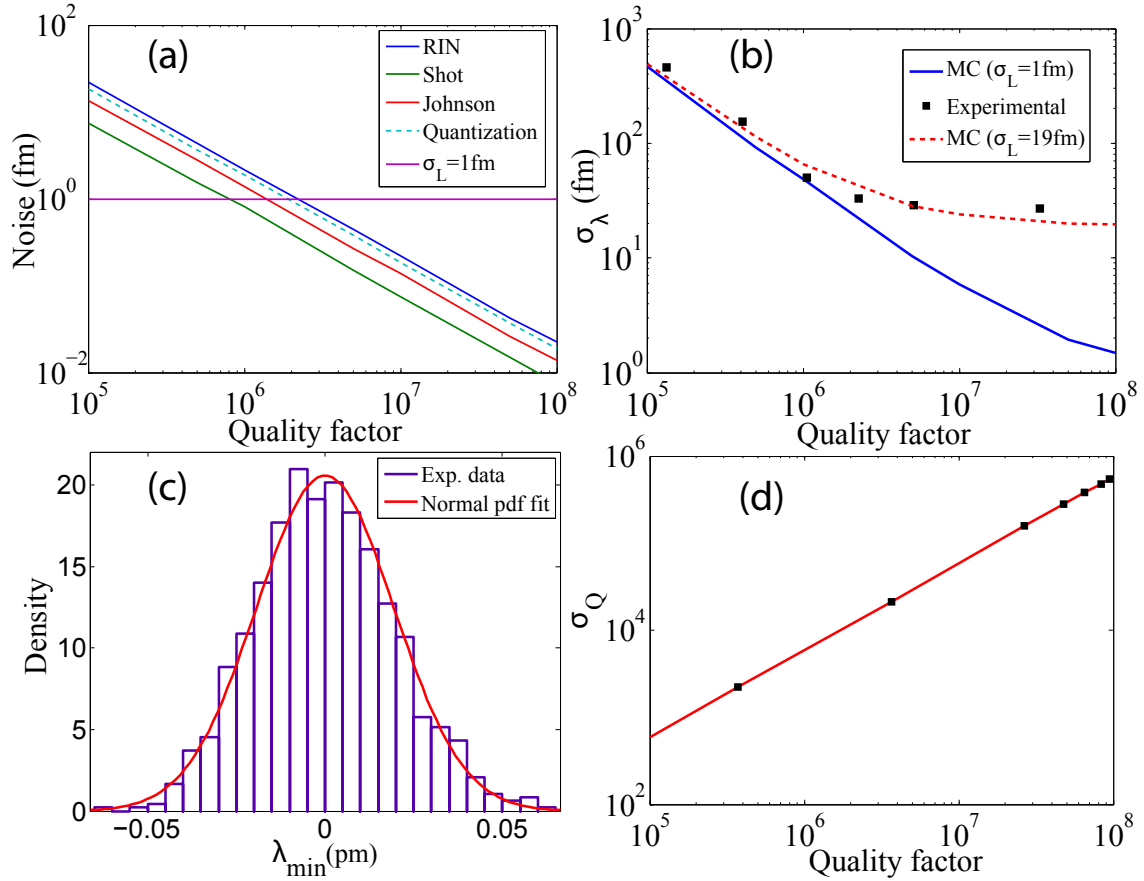


Fig. 6.3 (a)Monte Carlo simulations (MC) of individual noise sources. σ_L -Laser wavelength instability. (b)Total wavelength noise, σ_λ .(c)A representative normal probability density function (pdf) fit of the experimental noise data. The sum of the areas of the rectangles is equal to one.(d)Total quality factor noise, σ_Q .

6.2.3 Noise in the Q measurements (based upon the Lorentz fit)

Due to the experimental challenges, e.g., non linear curve fitting of the Lorentzian peak (a slow process) and related signal processing, we estimate the noise in the quality factor measurements only theoretically. To estimate this noise we perform the Lorentz fit, by using the OriginLab software, of the one thousand noise imposed Lorentzian peaks generated by

the previously mentioned Monte Carlo simulations. The quality factor is determined from the each fit, followed by the normal pdf fit to the one thousand estimated quality factors. The standard deviation of the fit gives the noise in the quality factor measurements, σ_Q . The results are shown in Fig. 6.3d. It should be noted that although σ_Q is estimated from Monte Carlo simulations only, the Monte Carlo simulations of wavelength noise display an excellent agreement with the experimentally measured wavelength noise. This supports the use of Monte Carlo simulations to estimate quality factor noise.

A fit to the modeled noise data for the quality factor measurements results in Eq. (6.6):

$$\sigma_Q = a_2 Q^{b_2}. \quad (6.6)$$

In our case, $a_2 = 0.01083$, and $b_2 = 0.9658$.

It should be noted, that the numbers, for both of the σ_λ , and the σ_Q , are for the components used, and coupling conditions (input power: $100\mu W$, 5%-10% coupling), in our test setup. It is possible that for the different components and conditions, the numbers may vary, but overall trend of the noise dependance on the Q of a cavity should stay the same as reported here.

6.2.4 Noise in the Q measurements (based upon the PS-CRDS)

In this section, we determine the noise in the Q measurements based upon the PS-CRDS. We assume that the phase shift is measured by the phase sensitive detection (PSD) technique which is implemented by an external lock-in amplifier.

Before beginning the actual analysis, we first define the *Propagation of Error*, a concept widely used in the error analysis of physical measurements [122].

If we have a quantity z which is a function of measured quantities x and y , i.e., $z = f(x, y)$ then the standard deviation (noise) of the z , σ_z , is given by

$$\sigma_z = \sqrt{\left(\frac{\partial f}{\partial x}\right)^2 \sigma_x^2 + \left(\frac{\partial f}{\partial y}\right)^2 \sigma_y^2}, \quad (6.7)$$

where σ_x and σ_y are random and independent noise contributions from the x and the y respectively. We use Eq. (6.7) for our noise determination.

Recalling our main equation (Section 3.4.3), representing the PS-CRDS signal at

the fiber output,

$$I_{wg} = |E_{wg}|^2 \cos^2(\omega_m t + \theta) = I_{wg} \left(\frac{1}{2} + \frac{\cos(2\omega_m t + 2\theta)}{2} \right). \quad (6.8)$$

In a lock-in amplifier, an input signal is multiplied by two quadrature reference signals, $\cos \omega t$, and $\sin \omega t$, which we call as the in-phase and the out-of-phase components, respectively (For detailed implementation of the lock-in, see manuals of SR830, Stanford Research Systems, or HF2LI, Zurich instruments (used in this thesis)). Multiplying the in-phase component to the PS-CRDS signal (Eq. (6.8)):

$$I_{IP} = I_{wg} \left(\frac{1}{2} + \frac{\cos(2\omega_m t + 2\theta)}{2} \right) \cos 2\omega t, \quad (6.9)$$

$$I_{IP} = \frac{I_{wg}}{2} \cos 2\omega t + \frac{I_{wg}}{4} \cos(4\omega_m t + 2\theta) + \frac{I_{wg}}{4} \cos 2\theta. \quad (6.10)$$

The lock-in amplifier has a built in low pass filter to block all of the AC signals so we are left with

$$I_{IP} = \frac{I_{wg}}{4} \cos 2\theta. \quad (6.11)$$

Similarly multiplying Eq. (6.8) with the out-of-phase component gives

$$I_{OP} = \frac{I_{wg}}{4} \sin 2\theta. \quad (6.12)$$

Therefore, the phase shift can be found in an intensity independent way by taking the ratio of I_{OP} and I_{IP} , i.e.,

$$\frac{\sin 2\theta}{\cos 2\theta} = \frac{I_{OP}}{I_{IP}}. \quad (6.13)$$

Assuming that both I_{OP} and I_{IP} have the same and the independent noise sources lumped in a single parameter, σ_N , then the propagation of error results in Eq. (6.14)

$$\sigma_{2\theta} = \sqrt{\left(\frac{\partial \frac{\sin 2\theta}{\cos 2\theta}}{\partial \sin 2\theta} \right)^2 \sigma_N^2 + \left(\frac{\partial \frac{\sin 2\theta}{\cos 2\theta}}{\partial \cos 2\theta} \right)^2 \sigma_N^2}, \quad (6.14)$$

where

$$\sigma_N = \sqrt{\sum_{i=1}^{i=N} \sigma_{Ni}^2}, \quad (6.15)$$

i.e., σ_N represents sum of all the independent noise sources in the setup. Solving Eq. (6.14) results in

$$\sigma_{2\theta} = \sigma_N \sqrt{\frac{(\cos^2 2\theta + \sin^2 2\theta)}{\cos^4 2\theta}}. \quad (6.16)$$

On simplification,

$$\sigma_{2\theta} = \frac{\sigma_N}{\cos^2 2\theta}, \quad (6.17)$$

i.e., in contrast to the Q measurement based upon a resonant peak, the noise in the PS-CRDS measurements has a weak dependance on the quality factor (Recall, $Q = f(\theta)$, Chapter 3). In sensing experiments, typically $\theta < 20^\circ$ so the noise is mainly dependant on σ_N . Furthermore, the noise is independent of the intensity of the input beam, i.e., no contribution of the RIN.

Determination of σ_N

The theoretical estimation of σ_N is challenging however, experimentally it can be determined from all of the instruments present in the setup. Our setup is shown in Fig. 6.4.

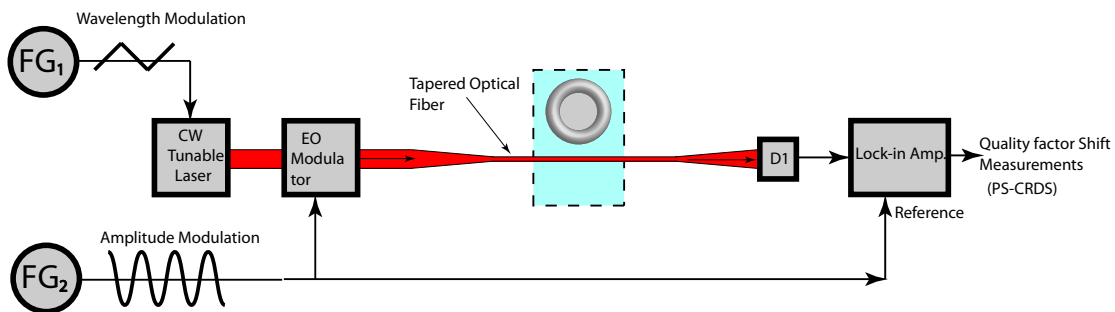


Fig. 6.4 Setup for determination of the noise, σ_N , in the PS-CRDS measurements.

It consists of a 1530nm tunable laser (Tunics T100R, Yenista Optics) as an input source for a tapered optical fiber. The laser is modulated in wavelength via function generator, FG₁. The laser is amplitude modulated via another function generator, FG₂ and an

electro-optic modulator (OC-192, JDSU). The change in quality factor, ΔQ , is recorded by a combination of a photodetector, D_2 and a lock-in amplifier (Zurich Instruments HF2LI). By moving the tapered fiber far away from the microcavity (i.e., no coupling) and continuously recording the phase (w.r.t. a reference) of the tapered fiber output signal, we can determine the noise, σ_N , in the PS-CRDS measurements. This measurement can be taken as coupling in the microcavity of a *zero* quality factor, i.e., the denominator of Eq. (6.17) is 1.

The experimental noise data is presented in Fig. 6.5 which shows that $\sigma_\theta = 4.10 \times 10^{-4}$ deg. It should be noted that this is the best result we have achieved so far, as on different days we find variation in this number. We believe that this variation is due to change in lab environmental conditions (e.g., temperature, humidity), acoustic vibrations, and quality of the connecting cables. However, we find that this number is always less than 2×10^{-3} deg.

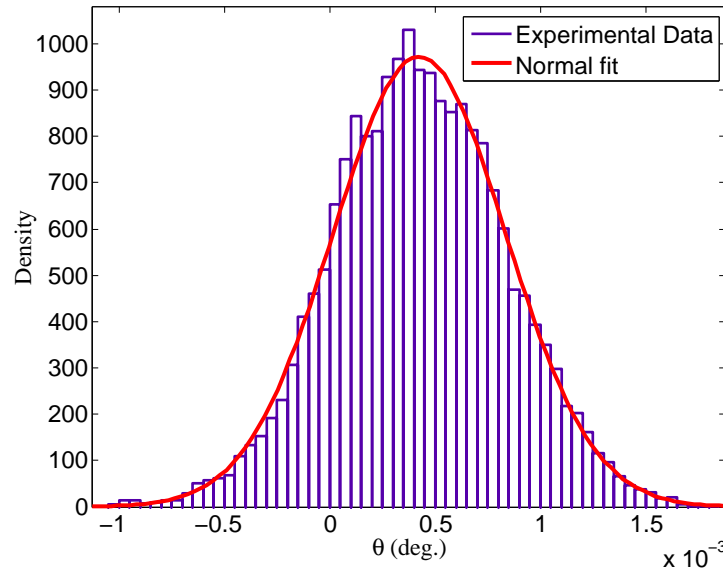


Fig. 6.5 The experimental noise data ($\sigma_\theta = 4.10 \times 10^{-4}$ deg.) for the phase shift (θ) of the waveguide signal w.r.t to the reference signal (FG₂).

Determination of the overall noise, $\sigma_{PS-CRDS}$, in the Q measurements

After determining σ_N we can now determine the noise, $\sigma_{PS-CRDS}$, in the Q measurements based upon PS-CRDS. For a desired quality factor in the 10% undercoupled regime, we

determine the phase shift, θ , of the waveguide signal by using the coupled mode equations presented in Chapter 3. We then use this phase shift, θ , in conjunction with Eq. (6.17) to evaluate the noise, $\sigma_{PS-CRDS}$, at a desired quality factor. The results are shown in Fig. 6.6. For comparison, we also provide the results of the Q measurements based upon the Lorentz fit of the resonant peak and for the same instruments as used in the PS-CRDS setup. It can be clearly seen that the noise in the Q for the PS-CRDS measurement is significantly lower than that of the noise in the Q measurement based upon the Lorentz fit of the resonant peak.

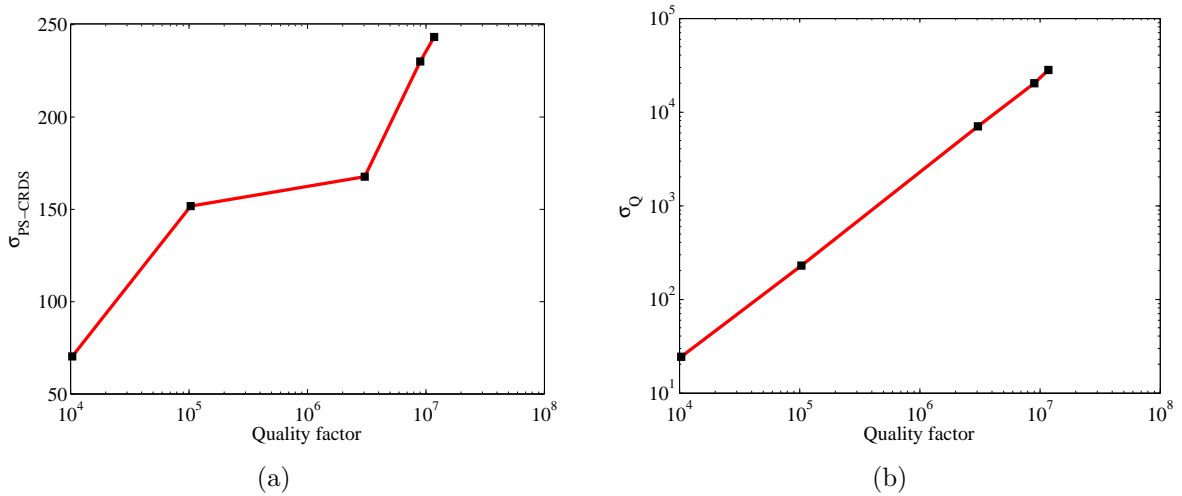


Fig. 6.6 Determination of the noise in the Q for the same instruments
 (a) Noise in the Q by using the PS-CRDS, evaluated by a combination of the experiments and the coupled mode equations (Chapter 3). (b) Noise in the Q by using a combination of the Monte Carlo simulations and the Lorentz fit (via OriginLab software.) of the resonant peak.

PS-CRDS is independent of RIN: Experimental proof

We previously show theoretically that the PS-CRDS measurements are independent of the laser intensity noise (RIN). Now we show experimentally that the noise in the PS-CRDS measurements does not depend upon the RIN. The setup for conducting such a measurement is shown in Fig. 6.7. The RIN noise is inserted into the setup by using a noise generator (Agilent 33250A). The noise from the noise generator is added to the modulation signal which is generated internally by the lock-in amplifier (Zurich Instruments HF2LI).

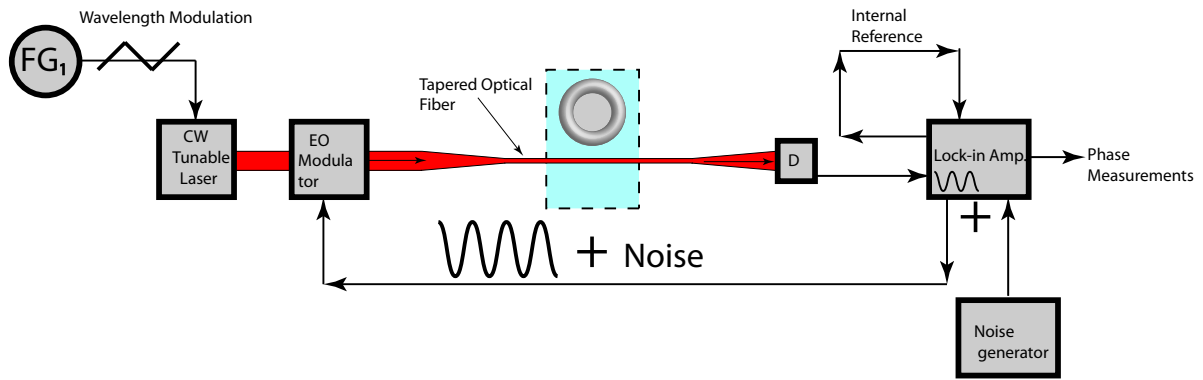


Fig. 6.7 Setup for showing that the PS-CRDS measurements are independent of the RIN

The reference for the phase shift measurements is also generated internally by the lock-in amplifier. The results are shown in Fig. 6.8. They clearly indicate that the PS-CRDS measurements are independent of the RIN.

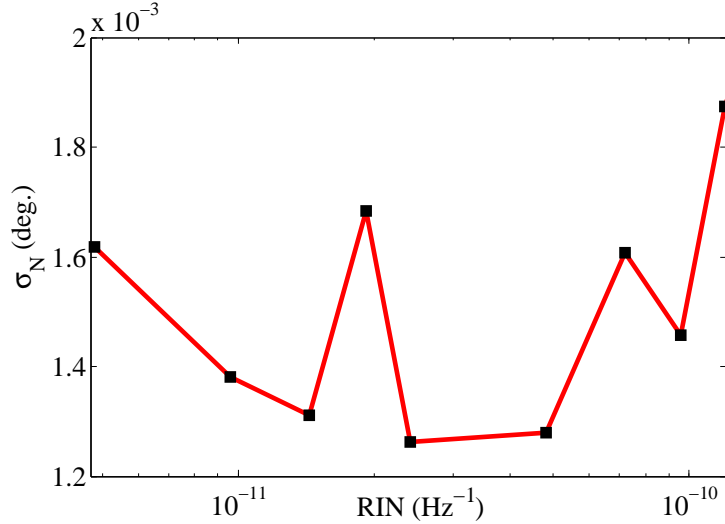


Fig. 6.8 Results show that the RIN does not contribute to the noise in the PS-CRDS measurements. Typical RIN of the lasers is $10^{-12} - 10^{-15} \text{ Hz}^{1/2}$

6.3 Signal to Noise Ratio

In this section, we provide the SNR results for the wavelength shift and the Q measurements based upon the Lorentz fit of the resonant peak. We do not present the results for the PS-

CRDS measurements due to the unavailability of the PS-CRDS experimental setup at 765nm to us. However, based upon the analysis of the last section, we can anticipate that the SNR results for the PS-CRDS measurements will be significantly better than that of the Q measurements based upon the Lorentz fit of the resonant peak. It should also be noted that in our experiments the final measurement is being done either by an electrical oscilloscope or by a lock-in amplifier therefore, SNR being examined is electrical. The noise sources, even the optical ones, are finally mapped to detected current via expressions presented in Section 6.2.1. The SNR results are shown in Figs. 6.9- 6.10.

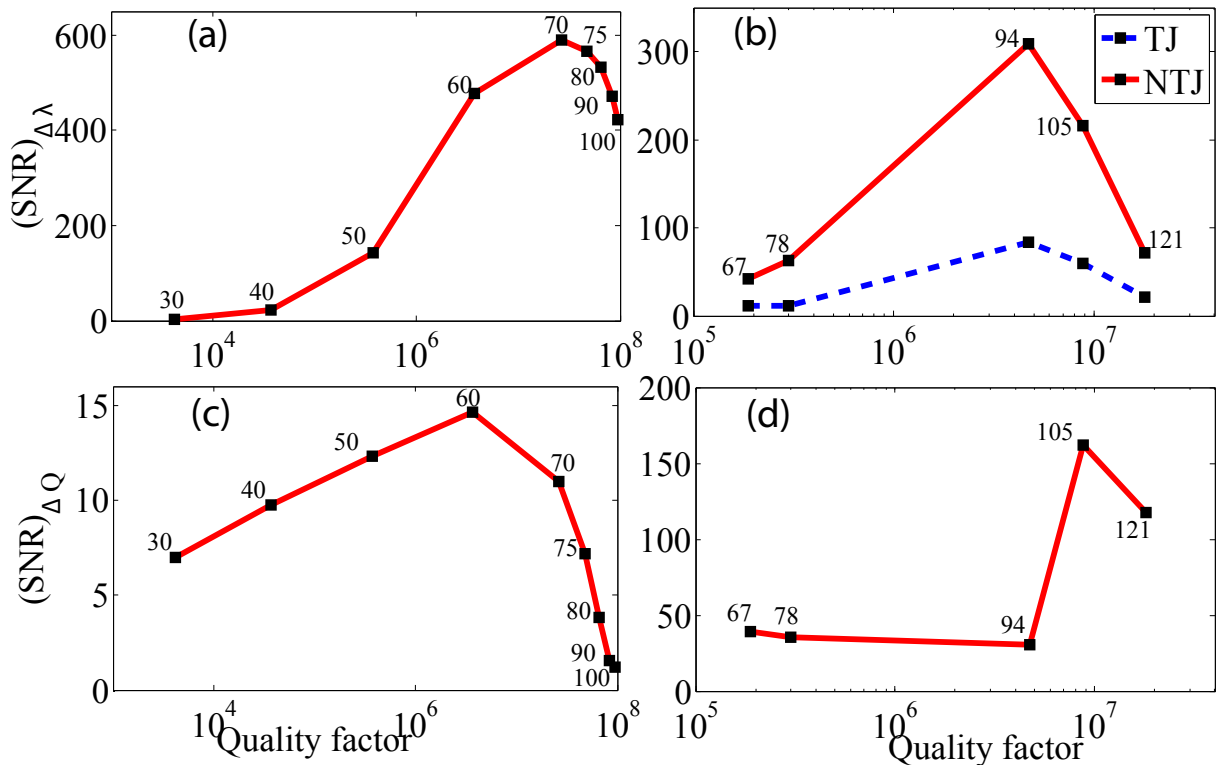


Fig. 6.9 Signal to Noise ratio results at 765nm. TJ- Noise due to the taper jitter included (noise data taken in water with the signal data when the cavity and the taper not in contact). NTJ- Noise due to the taper jitter not included (noise data taken in air with the cavity and the taper touching). (a), and (c) show the modeling results. (b), and (d) show the experimental results. In (d) the noise in Q is generated by Monte Carlo simulations at the experimental Q. The number at each data point represents the major diameter (D) of the cavity in microns.

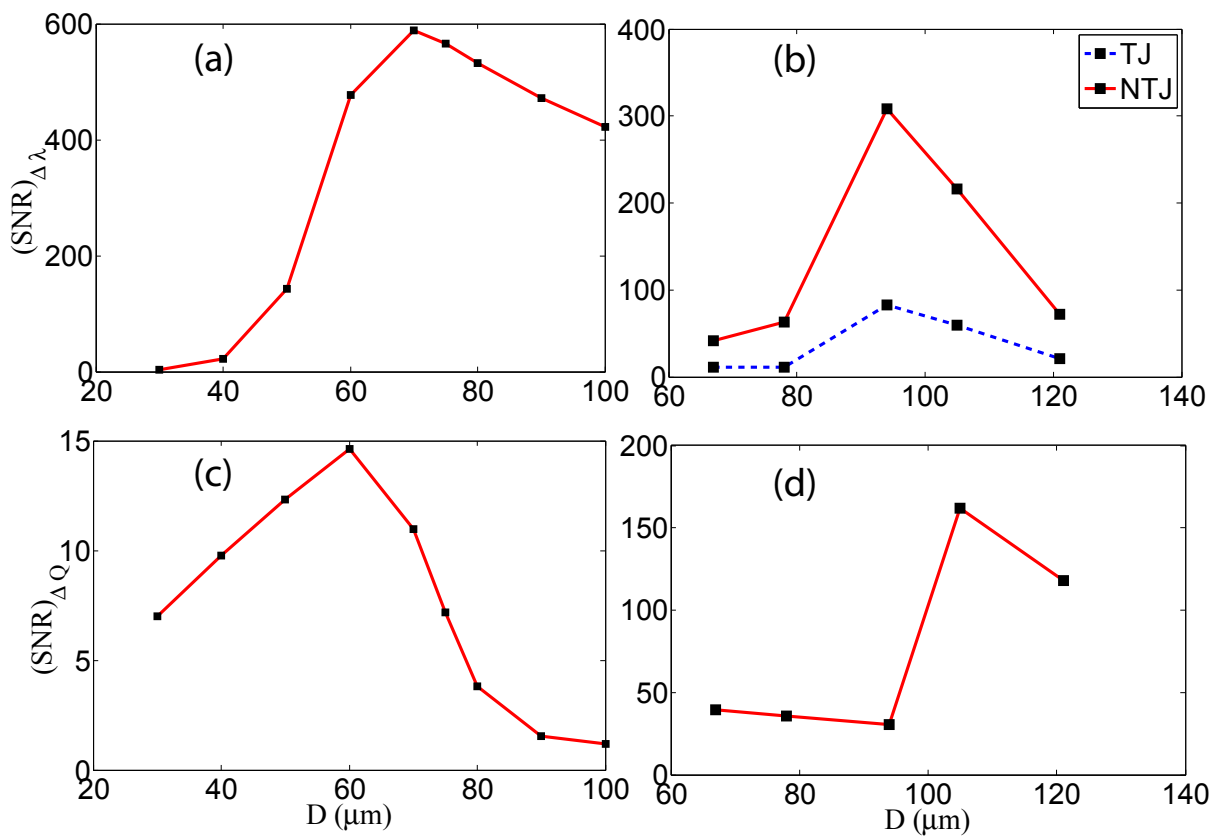


Fig. 6.10 Same data of Fig. 6.9 as a function of major diameter, D, of microtoroidal cavities. (a), and (c) are modeling results. (b), and (d) are experimental results.

In Figs. 6.9b and 6.10b, for the dashed curve, the experimental noise is measured in the DI water, immediately after recording the change in the sensing signal ($\Delta\lambda$). This measured noise represent all of the previously listed sources including, σ_{TJ} , σ_{FWS} , and σ_{TF} . However, we believe that taper jitter is the dominant noise in this measurement. For the solid curve (Figs. 6.9b and 6.10b), the noise data of the experiments performed in air has been used.

The results show that both of the modeling and the experiments follow the same trend and have a distinct region of maximum SNR. It can also be clearly seen that the maximum SNR for both types of measurements ($\Delta\lambda, \Delta Q$) is at a value of Q , which is not the highest one in either the modeling or the experimental results. However, due to the factors mentioned previously, the numbers differ in the modeling and the experimental results. In other words, experimentally, one has to look over the balance between the quality factor and the microcavity geometry to achieve the optimal performance of the sensor. The modeling results will aid in this optimization process. Furthermore, the optimized SNR can also complement the previously mentioned signal enhancement and the noise reduction approaches; further improvement of the sensing modality is possible.

6.4 Conclusions

We provide a comprehensive signal and noise analysis of the refractometric sensor based upon the microtoroidal cavity. We show that the noise in the Q measurement based upon the PS-CRDS is significantly lower than that of the noise in the Q measurement based upon the Lorentz fit of the resonant peak. After doing the signal and the noise analysis, we demonstrate that, operating a microcavity sensor at its highest possible Q factor does not mean an optimal sensor performance for both of the wavelength shift and the quality factor shift measurements. In a sensing experiment, instead of picking the dimensions of a cavity to maximize the Q , one should design a cavity with a Q to achieve the maximum signal to noise ratio. We believe that the present work will provide a starting point for designing a wide range of sensitive microcavity sensors with improved SNR values.

Chapter 7

Towards more accurate microcavity sensors: maximum likelihood estimation applied to combination of quality factor and wavelength shifts

¹In the pursuit of improving point-of-care applications researchers have demonstrated various forms of label-free and real-time optical sensors [114]. Among them, optical microcavities present highly sensitive diagnostic platforms for various sensing applications, e.g., detection of DNA, bacteria, virus and binding kinetics [5]. In these applications, it has been shown that a sensing event can be estimated by measuring a change in the resonant wavelength ($\Delta\lambda$) of the microcavity. However, the sensing event also induces a change in quality factor (ΔQ) of the cavity. In some sensing applications, the quality factor has been measured by applying Lorentzian fitting algorithms to the resonant dip of the microcavity [10, 73, 17]. The challenge with such non-linear methods is that they are not suitable for real-time implementation and sensitive sensing applications, primarily because the underlying approach is not only slow but may also require additional signal processing steps. Other approaches for measuring the quality factor in microcavities include Cavity Ring Down Spectroscopy (CRDS) [18], and one of its variants, Phase Shift-Cavity Ring Down

¹This chapter has been published in M. I. Cheema, U. A. Khan, A. M. Armani, and A. G. Kirk, “Towards more accurate microcavity sensors: maximum likelihood estimation applied to a combination of quality factor and wavelength shifts”, Optics Express 21, 22817-22828 (2013)

Spectroscopy (PS-CRDS) [68]. Recently, we have demonstrated a real-time biosensor in which both the resonant wavelength and the quality factor have been tracked as the function of a biosensing event [3]. In this scheme, we have used PS-CRDS to extract the quality factor. This technique minimizes the effect of noise on the measurement as compared to the non-linear fitting approach [3].

The existing work on the estimation of the sensing events is restricted to using the signal-to-noise ratio of only one parameter (either the change in wavelength, $\Delta\lambda$, or the change in the quality factor, ΔQ as a function of the sensing event) [5]. In [3], we have shown that although both of these parameters have different signal-to-noise ratios, they carry information about the same sensing event. This observation suggests that the performance of the sensor will be improved by developing a modality in which the sensing event is estimated by utilizing the information from both of these measurements. In this paper, we show a novel concept in which the gap between the statistical estimation approaches and the microcavity sensors is bridged by estimating a sensing event with a combination of the change in the wavelength and the quality factor measurements.

In this chapter, we consider *estimation* of the refractive index change. Here, the estimation refers to inferring the value of the refractive index change when the refractive index change is embedded in noisy measurements. In other words, the estimation is a process to extract a value efficiently from a noisy measurement by utilizing the probability distribution of the noise variables. Here, we show that the estimated value (of the refractive index change) is statistically more accurate when the two measurements, the wavelength shift and the quality factor shift, are combined together. Clearly, once the related values are separated from the noise (in a statistical fashion) and combined together to provide an improved estimated value of the refractive index change, the next step is to determine if the estimated refractive index change is large enough to claim that a biosensing event has occurred. This latter step where this comparison is made is referred to as *detection*. Here, we perform the comparison by employing a commercial sensor.

The rest of the chapter is organized as follows. In Section 7.1, we present the estimator model for both uncorrelated and correlated noise in $\Delta\lambda$ and ΔQ , followed by a brief discussion of the estimator. In Section 7.2, we present the experimental setup, results, and a brief discussion of the experimental noise. In Section 7.3, we describe the modeling results in conjunction with the estimator model and show the existence of three measurement regimes for estimation purposes. In Section 7.4, we discuss the extension of

the estimator model to the non-linear sensor response, and further propose a sensing metric to compare the performance of large class of sensors. Finally, Section 7.5 concludes the paper.

7.1 Estimation model of a sensing event

In this section, we present the mathematical modeling of our sensing system. A conceptual picture of an estimation process is shown in Fig. 7.1.

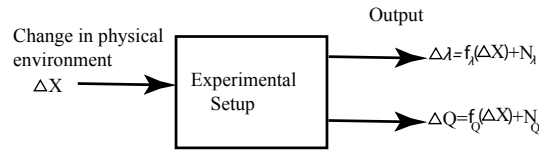


Fig. 7.1 The change in wavelength ($\Delta\lambda$) and quality factor (ΔQ) is induced by a sensing event. Each measurement has an experimental noise, i.e., N_λ , and N_Q . The estimator estimates ΔX from the outputs (measurements) of the system.

Mathematically, we may describe the above system as:

$$\Delta\lambda = f_\lambda(\Delta X) + N_\lambda, \quad (7.1)$$

$$\Delta Q = f_Q(\Delta X) + N_Q, \quad (7.2)$$

i.e., the change in X (ΔX , the sensing event) induces changes in the wavelength ($\Delta\lambda$) and the quality factor (ΔQ) with corresponding noise, N_λ and N_Q , in each of the measurements, respectively. Because the device physics is lumped into functions f_λ and f_Q , Eqs. (7.1)–(7.2) are valid for various experimental applications including bulk refractive index sensing and affinity based molecule sensing. Assuming that the sensor response is linear (valid for small ΔX), and ignoring any absorption due to the sensing event, we can simplify Eqs. (7.1)–(7.2) as follows:

$$\Delta\lambda = m_\lambda \Delta X + N_\lambda, \quad (7.3)$$

$$\Delta Q = m_Q \Delta X + N_Q, \quad (7.4)$$

where m_λ and m_Q represent the slopes of the corresponding linear response, and are de-

terminated from the calibration data. Note here that the restriction of the above setup to a linear model will be relaxed later in Section 7.4, where we present a non-linear sensor model and adjust the subsequent estimator.

The objective is to estimate the sensing event, $\widehat{\Delta X}$, from the measured change in wavelength, $\Delta\lambda$, and change in quality factor, ΔQ , while taking into account the experimental noise. Therefore, rewriting Eqs. (7.3)–(7.4) in the matrix form, we get:

$$\mathbf{y} = \Delta X \mathbf{m} + \mathbf{N}, \quad (7.5)$$

where

$$\mathbf{y} = \begin{bmatrix} \Delta\lambda \\ \Delta Q \end{bmatrix}, \quad \mathbf{m} = \begin{bmatrix} m_\lambda \\ m_Q \end{bmatrix}, \quad \mathbf{N} = \begin{bmatrix} N_\lambda \\ N_Q \end{bmatrix}. \quad (7.6)$$

We assume that the noise variables, N_λ , and N_Q , follow the normal (Gaussian) distribution:

$$N_\lambda \sim \mathcal{N}[\mu_\lambda, \sigma_\lambda^2] = \frac{1}{\sigma_\lambda \sqrt{2\pi}} \exp\left(-\frac{1}{2} \left(\frac{\Delta\lambda - \mu_\lambda}{\sigma_\lambda}\right)^2\right), \quad (7.7)$$

$$N_Q \sim \mathcal{N}[\mu_Q, \sigma_Q^2] = \frac{1}{\sigma_Q \sqrt{2\pi}} \exp\left(-\frac{1}{2} \left(\frac{\Delta Q - \mu_Q}{\sigma_Q}\right)^2\right), \quad (7.8)$$

where σ and μ represent the standard deviation and mean for the corresponding modality as denoted by the subscript. Since the noise variables (N_λ, N_Q) are assumed as Gaussian, the probability distributions of the change in wavelength, $\Delta\lambda$, and the change in quality factor, ΔQ , are also Gaussian, and are given by:

$$P(\Delta\lambda) = \mathcal{N}[\Delta X m_\lambda + \mu_\lambda, \sigma_\lambda^2], \quad (7.9)$$

$$P(\Delta Q) = \mathcal{N}[\Delta X m_Q + \mu_Q, \sigma_Q^2]. \quad (7.10)$$

Depending upon the experimental setup, the two noise variables, N_λ and N_Q , can be either uncorrelated or correlated. For example, simultaneous measurements of $\Delta\lambda$ and ΔQ and/or use of the same detector for each of them will result in correlated noise [3]. However, sequential measurements of $\Delta\lambda$ and ΔQ and with a separate detector for each of them will result in uncorrelated noise. In the following, we provide the maximum likelihood estimate of the sensing event, ΔX , for both uncorrelated and correlated noise sources.

7.1.1 Maximum likelihood estimation: Uncorrelated noise sources

In this section, we assume that the noise variables, N_λ and N_Q , are uncorrelated. The probability density function of \mathbf{y} (Eq. (7.5)), parameterized by the sensing event, ΔX , is a multivariate normal with mean \mathbf{m}_y and covariance matrix, R :

$$f_{\Delta X}(\mathbf{y}) = \frac{1}{2\pi \cdot \det(R)^{\frac{1}{2}}} \exp\left(-\frac{1}{2}(\mathbf{y} - \mathbf{m}_y)^\top R^{-1}(\mathbf{y} - \mathbf{m}_y)\right), \quad (7.11)$$

where \det represents determinant of a matrix,

$$\mathbf{m}_y = \begin{bmatrix} \Delta X m_\lambda + \mu_\lambda \\ \Delta X m_Q + \mu_Q \end{bmatrix}, \quad R = \begin{bmatrix} \sigma_\lambda^2 & 0 \\ 0 & \sigma_Q^2 \end{bmatrix}. \quad (7.12)$$

It is straightforward to show that Eq. (7.11) further reduces to

$$f_{\Delta X}(\mathbf{y}) = \mathcal{N}[\Delta X m_\lambda + \mu_\lambda, \sigma_\lambda^2] \mathcal{N}[\Delta X m_Q + \mu_Q, \sigma_Q^2], \quad (7.13)$$

i.e., the product of the two individual densities when the noises variables are uncorrelated. In order to derive the maximum likelihood estimate, we take the natural logarithm of both sides of Eq. (7.13),

$$\ln f_{\Delta X}(\mathbf{y}) = \ln \frac{1}{\sigma_\lambda \sigma_Q (2\pi)} - \frac{(\Delta\lambda - \Delta X m_\lambda - \mu_\lambda)^2}{2\sigma_\lambda^2} - \frac{(\Delta Q - \Delta X m_Q - \mu_Q)^2}{2\sigma_Q^2}. \quad (7.14)$$

According to the maximum likelihood principle [123], the optimal estimate for the sensing event, ΔX , (denoted by $\widehat{\Delta X}$) can be found by

$$\frac{\partial}{\partial \Delta X} \ln f_{\Delta X}(\mathbf{y}) = 0. \quad (7.15)$$

It can be verified that the application of Eq. (7.15) to Eq. (7.14) results in:

$$\widehat{\Delta X} = \frac{\left(\frac{\sigma_Q}{m_Q}\right)^2 \left(\frac{\Delta\lambda - \mu_\lambda}{m_\lambda}\right) + \left(\frac{\sigma_\lambda}{m_\lambda}\right)^2 \left(\frac{\Delta Q - \mu_Q}{m_Q}\right)}{\left(\frac{\sigma_\lambda}{m_\lambda}\right)^2 + \left(\frac{\sigma_Q}{m_Q}\right)^2}. \quad (7.16)$$

7.1.2 Maximum likelihood estimation: Correlated noise sources

We now derive the maximum likelihood estimate of the sensing event, ΔX , when the noise variables, N_λ and N_Q , are correlated. To this end, let $\sigma_{\lambda Q}$ be the covariance among the two noise variables then the covariance matrix of \mathbf{y} is represented as

$$R = \begin{bmatrix} \sigma_\lambda^2 & \sigma_{\lambda Q} \\ \sigma_{\lambda Q} & \sigma_Q^2 \end{bmatrix}. \quad (7.17)$$

Using the same procedure as described in the previous section, we obtain

$$\widehat{\Delta X} = \frac{\left(\frac{\sigma_Q}{m_Q}\right)^2 \left(\frac{\Delta\lambda - \mu_\lambda}{m_\lambda}\right) + \left(\frac{\sigma_\lambda}{m_\lambda}\right)^2 \left(\frac{\Delta Q - \mu_Q}{m_Q}\right) + \frac{\sigma_{\lambda Q}}{m_\lambda m_Q} \left(\frac{\Delta\lambda - \mu_\lambda}{m_\lambda} + \frac{\Delta Q - \mu_Q}{m_Q}\right)}{\left(\frac{\sigma_\lambda}{m_\lambda}\right)^2 + \left(\frac{\sigma_Q}{m_Q}\right)^2 + \frac{\sigma_{\lambda Q}}{m_\lambda m_Q}}. \quad (7.18)$$

It can be immediately verified that when the covariance, $\sigma_{\lambda Q}$, is zero, i.e., as in the case of uncorrelated noise, Eq. (7.18) reduces to Eq. (7.16). In a sensing experiment with correlated noise, $\sigma_{\lambda Q}$ can easily be evaluated by performing the numerical cross correlation of the measured noise (i.e., N_λ, N_Q).

7.1.3 Discussion of the estimator

The estimator in Eq. (7.16) and Eq. (7.18) provides the optimal estimate by considering both the underlying physics ($m_\lambda, m_Q, \Delta\lambda, \Delta Q$) and the noise variables (N_λ, N_Q) in each measurement. According to the estimator, the optimal estimate for the sensing event is a combination of the two measurements as long as noise in either of the measurements is neither zero nor infinite. In other words, the model provides a best estimate for the sensing event irrespective of the detection limit or signal to noise ratio of any measurement. The estimator also suggests the existence of three distinct measurement regimes in a microcavity sensor. In particular, if $\sigma_\lambda/m_\lambda > \sigma_Q/m_Q$ (i.e., change in wavelength, $\Delta\lambda$, is more noisy or less sensitive), then more weight is assigned to the ΔQ measurement for improved estimation, and vice versa. For the case of $\sigma_\lambda/m_\lambda = \sigma_Q/m_Q$, the estimator assigns equal weights to the two measurements. These distinct regimes are explored in more detail by running finite element simulations for a microcavity in conjunction with the Eq. (7.16), in

Section 7.3.

7.2 Estimation: Experimental results

In this section, we present the application of the estimator developed in the previous section by providing the experimental results for refractometric sensing. Although experiments can be performed for both uncorrelated (Eq. (7.16)) and correlated (Eq. (7.18)) noise sources, we opt for the uncorrelated case for simplicity.

The change in wavelength measurements, $\Delta\lambda$, are conducted by using the conventional method of tracking the minimum of the resonant peak [11]. The change in quality factor measurements, ΔQ , are conducted by using PS-CRDS [3]. The experimental setup and the measurement procedure is similar to the one used in [3] with a few modifications: (i) To uncorrelate the noise variables, N_λ , and N_Q , measurements of $\Delta\lambda$ and ΔQ are performed sequentially (within less than 10 seconds) on two separate detectors. This allows us to use Eq.(7.16); however in the case of simultaneous measurements of $\Delta\lambda$, and ΔQ and/or a single detector we must use Eq. (7.18) because the noise will be correlated; (ii) The PS-CRDS measurements have been made by using the phase sensitive detection (PSD) technique. The PSD technique is implemented in lock-in amplifiers and is advantageous in terms of high noise immunity e.g., in the present work, the phase shift of the waveguide signal (w.r.t a reference signal) can be measured down to 10^{-4} degrees, whereas, in our previous work [3] it was 0.15 degrees.

The experimental setup is shown in Fig. 7.2. A 1530nm tunable laser (Tunics T100R, Yenista Optics) is used to couple light in a microtoroidal cavity [18] via tapered optical fiber. The laser is modulated in wavelength via FG₁ (HP 8116A function generator, triangular waveform, 7V_{pp}, 100Hz for the $\Delta\lambda$ measurements, 100mHz for the ΔQ measurements) and an external port (FSC) of the laser. The laser is amplitude modulated via FG₂ (Agilent 33250A function generator, sinusoid waveform,, 200mV_{pp}, 40MHz), and an electro-optic modulator (OC-192, JDSU). The change in wavelength, $\Delta\lambda$, is recorded by a combination of a photodetector Det₁ (PDA10CS, Thorlabs), and an oscilloscope (Agilent DSO3034). The change in quality factor, ΔQ , is recorded by a combination of a photodetector Det₂ (HP 11982), and a lock-in amplifier (Zurich Instruments HF2LI).

The microtoroidal cavity (major diameter $140\mu m$, minor diameter $6\mu m$) [18] is immersed in heavy water (D_2O); because D_2O has lower optical loss at 1530nm than H_2O ,

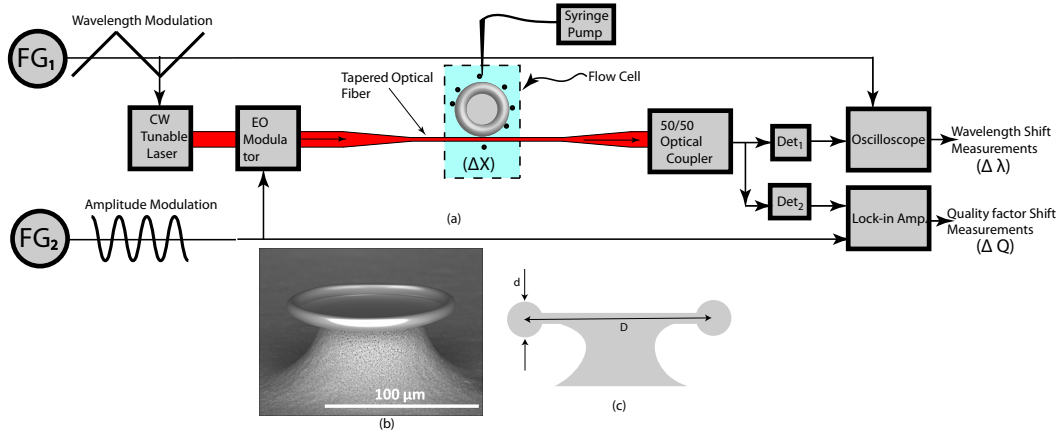


Fig. 7.2 (a) Experimental setup. FG-Function Generation, Det-Detector. Flow cell is same as the one used in [3] (b)Scanning electron microscope image of a typical microtoroidal cavity (c) Cross section of the microtoroidal cavity showing its dimensions: Major diameter, D , and minor diameter, d .

the microcavity is able to maintain a high quality factor [112]. Although 1530nm is not a preferred sensing wavelength, however, many of the components described above, such as the EO modulator and the 50/50 coupler, have been optimized for operation in the near-IR and are more commonly available in this wavelength range. As such, for the initial demonstration and verification of the estimator, it is critical to balance instrumentation availability and wavelength selection.

The refractive index change (i.e., the sensing event ΔX) is introduced by mixing salt in the heavy water. As a control experiment, the refractive index change is first measured by a commercial Surface Plasmon Resonance (SPR) system (GenOptics, France). The known ΔX is then used to measure the response of the cavity in terms of a change in wavelength, $\Delta\lambda$, and the change in quality factor, ΔQ . Both results are shown in Fig. 7.3. These results act as calibration curves for the sensor. From the results, slopes of the curves can be extracted: $m_\lambda = 53.6 \text{ nm/RIU}$ and $m_Q = 4.34 \times 10^6 \text{ RIU}^{-1}$. The linearity of the $\Delta\lambda$ measurements for similar range of refractive index change have also been previously reported in [124].

The noise in each measurement also follows the normal distribution as assumed in Section 7.1. A representative noise distribution for the phase shift measurement in the waveguide signal is shown in Fig. 7.4. This noise, N_Q , is measured by moving the tapered fiber away from the cavity and continuously recording the phase shift of the waveguide

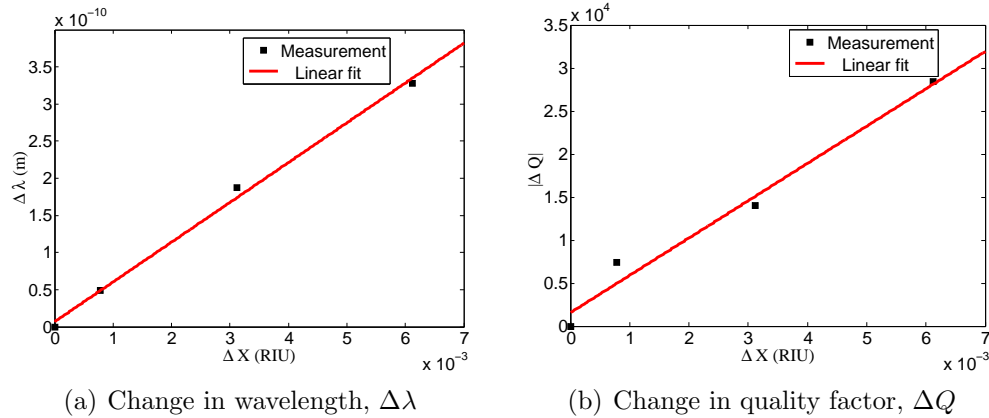


Fig. 7.3 Experimental results. $\Delta\lambda$ is positive (i.e. λ shifts towards red) and ΔQ is negative (i.e. Q decreases) as ΔX increases. This behavior is consistent with the fundamental microcavity theory and is verified by simulations.

signal w.r.t a reference signal (FG_2). From the noise data, standard deviation, σ_Q , of the noise in ΔQ calculation is 30 for the quality factor of 5×10^4 [125]. A similar distribution is obtained for the wavelength measurement, which gives standard deviation, σ_λ , of the noise in $\Delta\lambda$ measurement of 46 fm . The noise, N_λ , is measured with the tapered fiber in contact with the cavity and continuously recording the position of the minimum of the resonant peak. The numerically evaluated correlation coefficient of the two noise variables, N_λ and N_Q , is 1.163×10^{-3} i.e. the two noise sources have negligible correlation.

It should be noted that in the above noise measurements, the noise due to fluctuations in the coupling between the cavity and the tapered waveguide, also known as taper jitter, is avoided. Therefore, ideally the experiments need to be performed in a similar manner. However, if the taper and resonator are in contact, the cavity Q is extremely low ($< 10^3$) in our experiments. Hence, we have performed the measurements by maintaining the gap between the cavity and the tapered fiber. Consequently, the noise due to the taper jitter is present in our measurements and can also be seen in the linear fit to the data in Fig. 7.3 ($\sigma_\lambda = 6.76\text{ pm}$, $\sigma_Q = 1572$).

The application of the estimator is demonstrated by recording the response ($\Delta\lambda = 91.91\text{ pm}$, $\Delta Q = 1.24 \times 10^4$) of the cavity for another refractive index change, ΔX , which is not included in Fig. 7.3. The results, obtained by using data (m_λ , m_Q , σ_λ , σ_Q) of Fig. 7.3, are shown in the Table 7.1. The value of ΔX is also measured from the commercial SPR

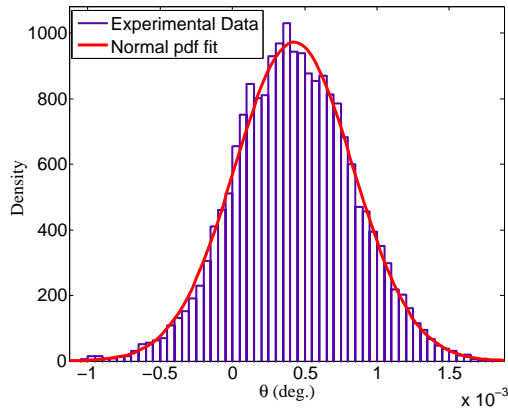


Fig. 7.4 A normal probability distribution fit (pdf) to the experimental noise data ($\sigma_\theta = 4.10 \times 10^{-4}$ deg.) for phase shift (θ) of the waveguide signal w.r.t to the reference signal (FG_2). The sum of the areas of the rectangles is equal to one. From the noise data, the noise (σ_Q) in ΔQ calculation is 30 for the quality factor of 5×10^4 . The noise (σ_λ) in $\Delta\lambda$ measurement is $46 fm$. See Section 7.2 for further details and discussion.

system and is found to be 1.95×10^{-3} .

Table 7.1 Estimation Results. From the commercial SPR system (GenOptics, France), $\Delta X = 1.95 \times 10^{-3}$ RIU.

	Assume $\sigma_\lambda = 0$	Assume $\sigma_Q = 0$	Estimator (Eq. (7.16))
$\widehat{\Delta X}$ (RIU)	1.714×10^{-3}	2.857×10^{-3}	1.838×10^{-3}
Percent Error	12.1 %	46%	5.6%

It is clear from the Table 7.1 that a combination of the two measurements provides a more accurate estimate of a sensing event than using any of the two measurements ($\Delta\lambda, \Delta Q$) alone. The high error in the quality factor measurements is attributed to the tapered fiber jitter. We anticipate that the error in the two measurements can be reduced significantly, i.e., accuracy of the estimator further improves, by conducting the measurements with the taper in contact with the cavity. In summary, the results indicate a successful proof-of-concept of utilizing the proposed estimator for sensing applications.

7.3 Distinct estimation regimes: Modeling results

In this section, we present the application of the estimator (Eq. (7.16)) by providing the modeling results for refractometric sensing. In particular, we show the existence of three distinct measurement regimes for the purposes of estimation. Appropriate modifications can be easily incorporated for the correlated noise variables in the context of Eq. (7.18).

We use a finite element model (FEM) [54] to model the microtoroidal cavities [18] immersed in heavy water at 1530nm . The FEM model is used to calculate the change in the wavelength, $\Delta\lambda$, and the change in quality factor, ΔQ , as a function of the intrinsic quality factor of the fundamental TM mode of the cavity, in response to the refractive index change ΔX ($10^{-4} - 10^{-3}$) in the outside medium (heavy water). The slopes (m_λ, m_Q) of the curves are then obtained for each quality factor. In simulations, the quality factor is varied by changing the major diameter of the cavity, holding the minor diameter constant ($6\mu\text{m}$).

The standard deviation, σ_λ of the wavelength noise, N_λ , is theoretically calculated by running Monte Carlo simulations at each quality factor used in the FEM model [125]. On the other hand, the standard deviation, σ_Q , of the quality factor noise, N_Q , is theoretically calculated by running simulations based upon the coupled mode theory of a resonator coupled with a waveguide [125]. We use the specifications (e.g., relative intensity of the laser, detector bandwidth and quantum efficiency, number of bits of the digitizer) of the components used in our experimental setup in these simulations. In short, the standard deviation, σ_λ , and the slope, m_λ , of the wavelength measurements decrease with the increase in quality factor [125], whereas for the quality factor measurements, the standard deviation, σ_Q , increases with the increase in the quality factor [125] and the slope, m_λ , has a maximum value at a particular quality factor [54].

The modeling results are shown in Fig. 7.5. These results clearly indicate the existence of three distinct regimes, as mentioned in Section 7.1.3. The modeling results provide insight into the different parameters which can be used to optimize a microcavity measurement system; for example, the balance between the microcavity geometry, its quality factor and the noise (N_λ, N_Q) in the measurement system.

It should be noted that the curves obtained in Fig. 7.5 are based upon the specifications of the equipment used in our experimental setup. It is also possible that for a different testing set-up, the two curves ($\sigma_\lambda/m_\lambda, \sigma_Q/m_Q$) may never intersect, resulting in

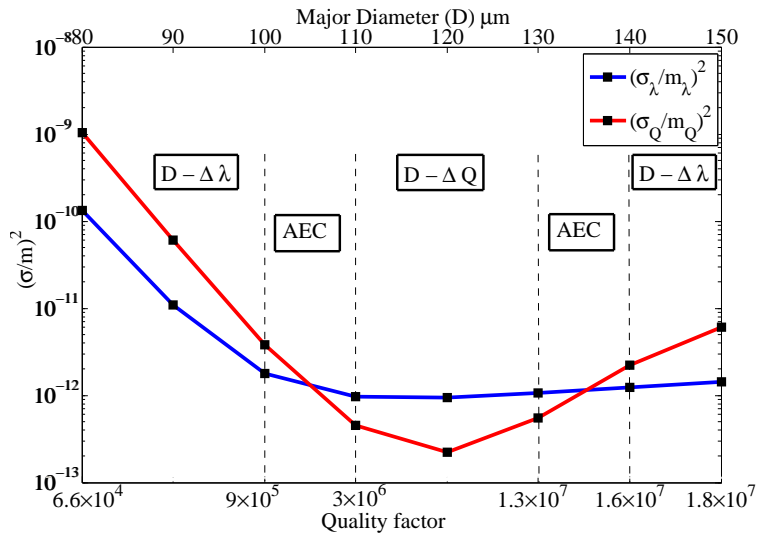


Fig. 7.5 Modeling Results. D- $\Delta\lambda$: $\Delta\lambda$ is dominant contributor in the estimator. D- ΔQ : ΔQ is dominant contributor in the estimator. AEC: Approximately equal contribution from the two measurements. For details of the simulation and other symbols, see Section 7.1 and Section 7.3.

a single regime. However, even in this case, the estimator (Eq. 7.16) will still give more accurate result as compared to using one of the measurements (but the contribution from the more noisy measurement will be lower).

7.4 Discussion

We now provide a few remarks and some discussion on the procedure.

- (i) We use microtoroidal cavities at 1530nm and employ PS-CRDS for change in quality factor, ΔQ , measurement. However, the analysis can be generalized to any wavelength. In fact, use of visible wavelengths will improve the sensitivity of the sensor due to negligible liquid absorption. Moreover, the current analysis is also valid when Full Width Half Maximum (FWHM) measurements are used to calculate the quality factor, Q ($Q = \lambda/\delta\lambda$, where $\delta\lambda$ is FWHM of the resonant peak), rather than PS-CRDS. However, σ_Q will be higher for FWHM measurements as compared to the PS-CRDS system [3, 125], and the setup will be more challenging for conducting real-time measurements. Furthermore, the present work is also applicable when other

peak tracking approaches are employed for wavelength shift measurements such as the interferometric technique presented in [39].

- (ii) The use of calibration curves to determine the slope of the linear response of the change in wavelength (m_λ) and the quality factor (m_Q) of microtoroidal cavities is not necessary for all cavity geometries. For example, analytical expressions for microsphere cavities have been thoroughly established enabling the calculation of these values [124, 45, 126].
- (iii) The proposed approach assumes linearity of the change in wavelength, $\Delta\lambda$, and the change in quality factor, ΔQ , for small change ΔX (i.e., sensing event). This assumption may not be valid for large range of ΔX [45]. The analysis presented in Section 7.1 can be extended to the case of general dependance of the change in wavelength, $\Delta\lambda$ and the change in quality factor, ΔQ , on the sensing event, ΔX . Application of the maximum likelihood principle to the general nonlinear model, Eq. (7.1) and Eq. (7.2), results in the following equation (assuming uncorrelated noise variables, N_λ , N_Q , and after setting the natural logarithm to 0):

$$\frac{(\Delta\lambda - f_\lambda(\Delta X) - \mu_\lambda) f'_\lambda(\Delta X)}{\sigma_\lambda^2} + \frac{(\Delta Q - f_Q(\Delta X) - \mu_Q) f'_Q(\Delta X)}{\sigma_Q^2} = 0, \quad (7.19)$$

where $f'(\Delta X)$ represents the derivative of f w.r.t ΔX . Solution of Eq. (7.19) for ΔX gives the optimal estimate, $\widehat{\Delta X}$, for the sensing event.

The simulations confirm that as ΔX (refractive index change in heavy water) increases, quadratic or cubic dependance of the change in wavelength, $\Delta\lambda$, and the change in quality factor, ΔQ , on ΔX lead to the fitting noise that is less than the experimental noise. For example, assuming a quadratic dependance of $\Delta\lambda$, and ΔQ in the following form:

$$\Delta\lambda = m_{\lambda N}\Delta X^2 + m_{\lambda L}\Delta X + N_\lambda = f_\lambda(\Delta X) + N_\lambda, \quad (7.20)$$

$$\Delta Q = m_{Q N}\Delta X^2 + m_{Q L}\Delta X + N_Q = f_Q(\Delta X) + N_Q, \quad (7.21)$$

where $m_{\lambda N}$, $m_{\lambda L}$, $m_{Q N}$, and $m_{Q L}$ are constants then solution of Eq. (7.19) provides the best estimate for the sensing event.

- (iv) The development of a common metric to enable the comparison of different types of label-free sensors can involve various elements [46, 47]. The present work is also applicable to compare the performance of not only microcavity sensors but a large class of sensors (either optical or non-optical). It is shown in Appendix A that a sensing metric for comparing any linear sensor may be given by

$$SM = \frac{m(\Delta A - \mu)}{\sigma^2}, \quad (7.22)$$

where m is the slope of linear response of the sensor, ΔA is the measured quantity (e.g., change in quality factor in microcavity sensor or change in incidence angle/wavelength in surface plasmon sensors [127]), the variables (μ, σ) are the mean and standard deviation of normal noise distribution. Although Eq. (7.22) is applicable to the linear sensors, the sensing metric, SM , can also be derived for non-linear sensors. The result presented in Eq. (7.22) assumes that the response of the sensor is the same regardless of the location of a sensing event on the sensor surface. Depending upon the sensing application and the sensor platform, this assumption is not always true. For example, in case of microcavity sensors, detection can only occur when a molecule binds within the evanescent field of the device, which occupies a very small portion of the sensor surface [45]. For the case of smaller (or single) sensing entities, the response of the microcavity sensor can range from a maximum (sensing event happens at the equator for the fundamental mode) value to zero (sensing event occurs where the evanescent field is absent). Therefore, a correction to Eq. (7.22) is necessary.

We define the corrected sensing metric as follows:

$$SM_c = \frac{m(\Delta A - \mu)}{\sigma^2} \gamma, \quad (7.23)$$

where γ is a unit less quantity with values between 0 – 1 and depends upon the sensor geometry and underlying physics. For example, in case of microcavity sensors for bulk refractive index change applications, $\gamma = 1$. For the case of sensing of single or smaller sensing entities, γ can be estimated from simulations [54] by taking the ratio of modal overlap with the cavity surface, where the binding event occurs, and total surface area of the cavity. For microspheres, γ can be calculated analytically for a binding of a single protein at a random location of the sphere [126]. It should be noted, regardless

of the sensing application or the sensor platform, that if microfluidics ensure that the sensing event always occur at the place of maximum sensor response, then γ will also be maximum. For example, the liquid core optical ring resonators [20] have high γ as compared to the conventional microspheres or microtoroidal cavities, but at the same time they suffer from the low quality factor. In short, for achieving optimal performance of a sensor, we may have to consider multiple factors such as m , ΔA , γ (i.e., the device physics and the geometry), and μ , σ (i.e., the system noise parameters).

7.5 Conclusions

A microcavity sensor can provide information about a sensing event from two sources, i.e., the resonant wavelength and the quality factor. Instead of discarding one of the information sources, we present a simple, yet statistically optimal, method for combining the two information sources in order to improve the estimation accuracy of the underlying sensing event. The optimal estimate is based on the maximum likelihood principle. We show application of the estimator by conducting proof-of-concept experiments for a refractometric sensor based on the microtoroidal cavity. We further provide insight into the estimation process by running FEM simulations in conjunction with the estimator. Finally, we postulate a sensing metric that is valuable for comparing multiple types of sensors. We believe that the present work has potential for use in a wide-range of applications employing microcavity sensors.

Chapter 8

Conclusions

In this thesis, we demonstrate novel approaches for improving the performance of WGM microcavity sensors. All of these approaches, except for the FEM, are independent of the WGM microcavity geometry used in a sensing application, whereas the FEM applies to any axisymmetric microcavity. Most of our demonstrated work including the FEM, the signal and the noise analysis, and the estimator will find applications in all of the demonstrated approaches for determining the parameters of a microcavity in a sensing application.

We now revisit each of our demonstrated techniques or analysis by highlighting its significance individually.

- **PS-CRDS expressions:** By using the coupled mode theory, we develop the PS-CRDS expressions for accurately determining the ring down time of a microcavity coupled with a waveguide. These relations are developed for the transmission mode of the cavity-waveguide system. Our work shows a significant improvement over previous studies [68], where the researchers not only used an approximate four mirror model for the microcavity-waveguide system but also their derived expression, in the transmission mode, gives the phase shift of the waveguide signal and not the cavity signal. Moreover, our developed expressions are not only useful for microcavity sensors but they may also provide a good foundation for studying other applications of microcavities, such as modulators [128].
- **PS-CRDS microcavity sensor:** We demonstrate a novel technique for simultaneously tracking of the resonant wavelength and the quality factor as a function of the sensing event for a microtoroidal cavity sensor. In this technique, measurement

of the quality factor is based upon the PS-CRDS and is not only immune to the laser intensity noise but also has the minimum wavelength instability noise. Both of these noise mechanisms are present in the previously demonstrated approaches for measurement of a microcavity parameter in a sensing application. Our work is the first demonstration of using the PS-CRDS (or any of the variants of the CRDS) in conjunction with microcavities for liquid phase applications. Moreover, the demonstrated technique is also useful to characterize microcavities in air with high noise immunity.

Currently, chemists employ the CRDS and many of its variants to free space cavities primarily for gas phase applications. However, the free space systems are usually large, bulky and face many challenges in addressing liquid phase applications. Chemists may find the demonstrated PS-CRDS microcavity technique as an alternative which not only provides a miniaturized and a sensitive solution but may also address spectrum of applications ranging from the absorption spectroscopy of gases to the liquid chromatography.

- **Accurate FEM model:** We develop an accurate finite element model for axisymmetric microcavities. The model is an improved version of the previously demonstrated model that lacks the capability of determining the accurate quality factor of a microcavity. Our model proves to be an invaluable tool for conducting the signal analysis of the microcavity sensors. With the model, we are able to accurately calculate various microcavity parameters including the resonant wavelength, the quality factor, the mode volume, and the tunneling distance. Determination of these parameters is not only useful for a sensing application but also in other applications, such as non-linear optics of microcavities.
- **Optimum SNR for microcavity sensors:** We conduct a comprehensive signal analysis of those refractometric microcavity sensors that utilize the resonant wavelength tracking and the Q tracking as their measurement approach. We demonstrate, by employing the FEM and experiments¹, that the signal decreases as the Q of a microcavity increases in the wavelength tracking approach, whereas in the Q tracking approach, as the Q of a microcavity increases the signal increases up to a particular

¹Q tracking experiments are based upon the Lorentz fit to a resonant peak and not the PS-CRDS

Q value after which it starts decreasing.

Noise analysis is one the most important components of any sensor. We conduct a comprehensive noise analysis of those microcavity sensors which employ the resonant wavelength tracking, Q tracking based upon a Lorentz fit and the PS-CRDS as their measurement approaches. We identify various noise sources that affect each measurement approach. We show, by simulations and experiments, that the noise in the wavelength tracking approach decreases as the Q of a cavity increases, whereas the noise increases as the Q of a cavity increases in the Q tracking based upon a Lorentz fit approach. The noise in Q tracking based upon the PS-CRDS has a weak dependance on the Q of a cavity and is significantly lower than that of the Lorentz fit approach (Fig.6.6). We also show, by theory and experiments, that PS-CRDS measurements are immune to RIN.

We then determine the SNR of those refractometric microcavity sensors that utilize the resonant wavelength tracking and the Q tracking based upon the Lorentz fit as their measurement approach. We show that for a given cavity size there is an optimum value for the quality factor which maximizes the SNR. Interestingly, the Q corresponding to the optimal SNR is not the highest Q of the microcavity. This result is contrary to a perception in the microcavity literature that a microcavity with a higher Q value will display a better sensing performance.

We want to re-emphasize that a signal and a noise analysis of any sensor must be a starting point for utilizing a sensor in a particular application. Clearly there are a variety of factors that may cause the experimental Q of a microcavity differ from the value determined by calculation (see Section 6.1 for details). However, we also examine the various noise sources individually (Fig. 6.3), as a function of the Q , by basing the noise analysis on the specifications of the components used in the experimental setup. Depending upon the operating Q of a cavity, this can give an indication to researchers as to which particular noise source will dominate. We believe that, regardless of the measurement approach, the SNR work in this thesis can act as a good initial start for achieving a better sensing performance from a microcavity.

- **More accurate estimation of a sensing event:** We develop an innovative way of improving the accuracy of microcavity sensors by borrowing concepts from the field of statistical signal processing and apply them in the field of microcavity sens-

ing. The development of this technique is motivated from the fact that generally a sensing event influences both of the resonant wavelength and the quality factor of a microcavity. Since the signal and the noise due to both of these parameters are different, a model is required to optimally extract the information about the sensing event from the two parameters. The solution to the model is provided by statistical signal processing approaches. We also experimentally demonstrate that the model provides a more accurate estimate of the sensing event than that of the single parameter measurement approach. By using a combination of the estimator model, the FEM and noise analysis based upon the instruments used in the experimental setup, we show that the estimation process has three distinct regimes as a function of the Q of a microcavity (Fig.7.5). Depending upon the operating Q of the cavity in experiments, this result can provide a guideline to researchers for optimizing the overall estimation process. We also extend the estimator model to develop a metric which can compare the performance of a wide range of sensors. The sensor metric can also provide an excellent starting point for determining and comparing fundamental limits of optical sensors. However, particularly for microcavity sensors, the author believes that it is harder to comment on the fundamental limit as variety of factors including microfluidics, surface chemistry, microcavity Q along with geometry, sensing approach, system noise, and specifications of instruments used in experiments need to be considered thoroughly.

Although microrings suffer from the low Q as compared to microspheres or microtoroids, but they provide a multiplexed, an integrated microfluidics and an integrated waveguide platform [16]. One can envision the multiplexed microring platform as a sensor, whose all channels are sensing a same event. The estimator model is applicable to that sensing platform and may provide an indirect way of improving the performance of microring sensors by considering the signal and the noise of all the channels for estimation of the sensing event.

Based upon the work done in this thesis, one may explore many future avenues. Some of these are:

- *Sensing of single protein or molecule by utilizing the PS-CRDS with a microcavity that has parameters optimized to provide maximum SNR, and using the estimation process.* However, two major issues need to be addressed before pursuing this project.

Firstly, we need to have a microfluidics system that can ensure delivery of a single protein or molecule to the portion of the microcavity sensor where the cavity mode is present. An experiment investigating single protein detection means that one needs to inject the single protein in the flowcell rather than injecting many proteins. As we believe that detection of one protein out of many is not a true single protein detection experiment. Secondly, an efficient surface chemistry protocol is highly desired for a stable and a specific binding event.

- *Replacing the tunable laser with a broadband source.* We believe that there are two major challenges which may hinder the development of a commercially viable product based on microcavity sensors. Firstly, instead of a tapered fiber, an integrated sensing platform in terms of a waveguide² and a high Q microcavity is required. A new fabrication method has recently been demonstrated that appears capable of implementing an integrated microcavity sensor platform. In this fabrication method, researchers replace CO₂ reflow process of fabricating microtoroidal cavities by a chemical etching step [19]. They also show fabrication of the waveguide separately by the same chemical etching process [22]. Secondly, the tunable laser source needs to be replaced by a broadband source, such as a LED, in the sensor. This may be possible by applying the Fourier Transform (FT) Spectroscopy in conjunction with the PS-CRDS microcavity sensor powered by a LED. The idea has already been employed successfully in free space cavities [129]. The work in this thesis, particularly Chapter 3–4, can provide an excellent starting point to realize a microcavity sensor which is not only sensitive and noise immune but is also a laser free. However, one may need to overcome some of the challenges such as efficient and sufficient injection of light from a broadband source into a single mode waveguide.
- *Separating a simultaneous refractive index change and an absorption change induced by a sensing event.* In a sensing application, a simultaneous change in both of the loss and the refractive index collectively impact the quality factor and the resonant wavelength of microcavities. By using the FEM, we can develop empirical expressions of the quality factor and the resonant wavelength as a function of the loss and the refractive index changes for microtoroidal cavities. The relationships in conjunction

²Although, microrings have an integrated waveguide but they suffer from a low signal due to a low Q

with the PS-CRDS sensor may provide a route to an individual identification of the loss and the refractive index changes.

We now provide our contributions to the field in a graphical manner (Fig. 8.1) by connecting all of the pieces of work conducted in this thesis.

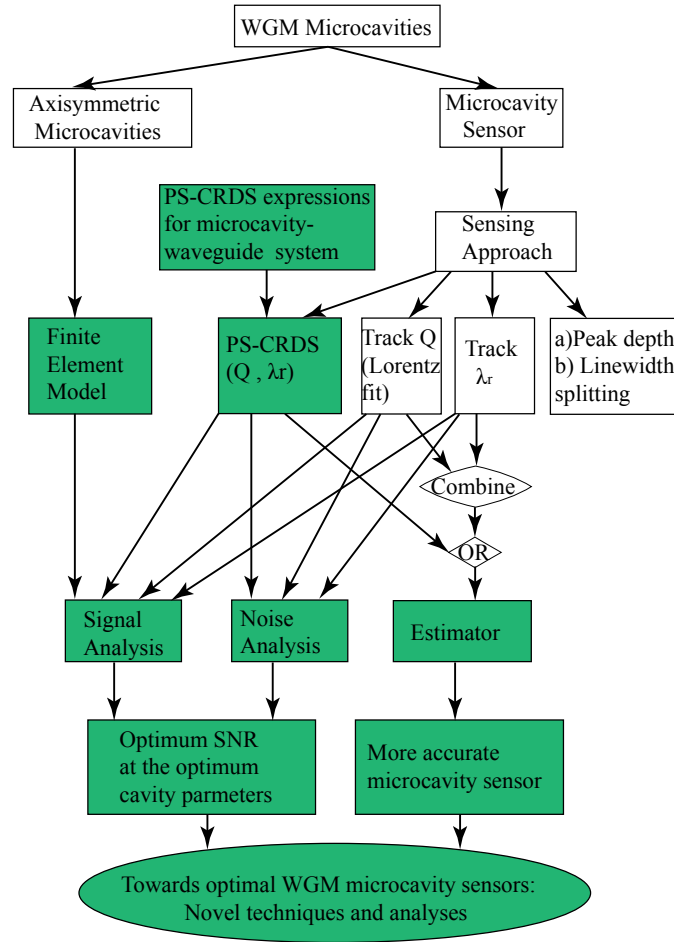


Fig. 8.1 Contributions are shown in green.

In summary, microcavity sensors have a great potential as highly sensitive detectors for very low concentrations of proteins and other molecules. Clearly their commercial implementation requires much progress in microfluidics, fabrication, integration and surface chemistry, topics which are all beyond the scope of this thesis. However, we have shown here that it is possible to improve the performance of these sensors by optimizing the sensor

design, by employing the PS-CRDS method and by combining multiple sensing metrics to obtain a better estimate of the signal.

Appendix A

Sensing metric

Suppose that we have n different sensors which produce a change in their output (ΔA) in response to the same sensing event (ΔX). We estimate ΔX by combining the results from all of the sensors while considering the corresponding noise. In this way, the sensor with maximum weight in the estimation process performs better and leads us to the sensing metric. Assuming that the response of each sensor is linear, we can write:

$$\Delta A_1 = m_1 \Delta X + N_1, \quad (\text{A.1})$$

⋮

$$\Delta A_n = m_n \Delta X + N_n, \quad (\text{A.2})$$

where N_n are the experimental noise (assuming normal distribution) measured in the response of a sensor corresponding to the sensing event (ΔX) and m_n is the slope of each sensor's linear response. Application of the maximum likelihood principle to the above system of equations results in the following equation:

$$\widehat{\Delta X} = \frac{1}{Z} \left(\underbrace{\frac{m_1(\Delta A_1 - \mu_1)}{\sigma_1^2}}_{\text{Sensor 1}} + \underbrace{\frac{m_2(\Delta A_2 - \mu_2)}{\sigma_2^2}}_{\text{Sensor 2}} + \cdots + \underbrace{\frac{m_n(\Delta A_n - \mu_n)}{\sigma_n^2}}_{\text{Sensor } n} \right), \quad (\text{A.3})$$

where

$$Z = \sum_{i=1}^{i=n} \frac{m_i^2}{\sigma_i^2}. \quad (\text{A.4})$$

In Eq. (A.3), $1/Z$ is multiplied to all of the terms. Therefore, the individual terms on the right hand side of Eq. (A.3) labeled as Sensor 1, Sensor 2, Sensor 3 dictate which term receives a higher weight, justifying the sensing metric proposed in Eq. (7.22).

References

- [1] S. Arnold, M. Noto, and F. Vollmer, “Consequences of extreme photon confinement in micro- cavities: I. ultra-sensitive detection of perturbations by bio-molecules,” in “Frontiers of Optical Spectroscopy,” , vol. 168 of *NATO Science Series II: Mathematics, Physics and Chemistry*, B. Bartolo and O. Forte, eds. (Springer Netherlands, 2005), pp. 337–357.
- [2] M. Oxborrow, “Traceable 2-D finite-element simulation of the whispering-gallery modes of axisymmetric electromagnetic resonators,” IEEE Transactions on Microwave Theory and Techniques **55**, 1209–1218 (2007).
- [3] M. I. Cheema, S. Mehrabani, A. A. Hayat, Y.-A. Peter, A. M. Armani, and A. G. Kirk, “Simultaneous measurement of quality factor and wavelength shift by phase shift microcavity ring down spectroscopy,” Opt. Express **20**, 9090–9098 (2012).
- [4] A. Armani, “Single molecule detection using optical microcavities,” in “Photonic Microresonator Research and Applications,” , vol. 156 of *Springer Series in Optical Sciences*, I. Chremmos, O. Schwellb, and N. Uzunoglu, eds. (Springer US, 2010), pp. 253–273.
- [5] F. Vollmer and L. Yang, “Label-free detection with high-Q microcavities: a review of biosensing mechanisms for integrated devices,” Nanophotonics pp. 267–291 (2012).
- [6] A. P. F. Turner, “Biosensors: sense and sensibility,” Chem. Soc. Rev. **42**, 3184–3196 (2013).
- [7] X. Fan, I. M. White, S. I. Shopoua, H. Zhu, J. D. Suter, and Y. Sun, “Sensitive optical biosensors for unlabeled targets: A review,” Analytica Chimica Acta **620**, 8–26 (2008).
- [8] H. K. Hunt, C. Soteropoulos, and A. M. Armani, “Bioconjugation strategies for microtoroidal optical resonators,” Sensors **10**, 9317–9336 (2010).
- [9] V. S. Ilchenko and L. Maleki, “Novel whispering-gallery resonators for lasers, modulators, and sensors,” in “Proc. SPIE,” (2001), pp. 120–130.

- [10] L. Maleki and V. S. Ilchenko, "Techniques and devices for sensing a sample by using a whispering gallery mode resonator, us patent 6,490,039," (2002).
- [11] F. Vollmer, D. Braun, A. Libchaber, M. Khoshima, I. Teraoka, and S. Arnold, "Protein detection by optical shift of a resonant microcavity," *Applied Physics Letters* **80**, 4057–4059 (2002).
- [12] F. Vollmer, S. Arnold, D. Braun, I. Teraoka, and A. Libchaber, "Multiplexed dna quantification by spectroscopic shift of two microsphere cavities," *Biophys. J. (USA)* **85**, 1974 – 9 (Sept. 2003).
- [13] C.-Y. Chao and L. J. Guo, "Biochemical sensors based on polymer microrings with sharp asymmetrical resonance," *Applied Physics Letters* **83**, 1527–1529 (2003).
- [14] A. Yalcin, K. Popat, J. Aldridge, T. Desai, J. Hryniewicz, N. Chbouki, B. Little, O. King, V. Van, S. Chu, D. Gill, M. Anthes-Washburn, and M. Unlu, "Optical sensing of biomolecules using microring resonators," *IEEE Journal of selected Topics in Quantum Electronics* **12**, 148–155 (2006).
- [15] C. Chao, W. Fung, and L. Guo, "Polymer microring resonators for biochemical sensing applications," *IEEE journal of selected topics in Quantum Electronics* **12**, 134–142 (2006).
- [16] M. Iqbal, M. Gleeson, B. Spaugh, F. Tybor, W. Gunn, M. Hochberg, T. Baehr-Jones, R. Bailey, and L. Gunn, "Label-free biosensor arrays based on silicon ring resonators and high-speed optical scanning instrumentation," *Selected Topics in Quantum Electronics, IEEE Journal of* **16**, 654–661 (2010).
- [17] A. M. Armani and K. J. Vahala, "Heavy water detection using ultra-high-q microcavities," *Opt. Lett.* **31**, 1896–1898 (2006).
- [18] D. K. Armani, T. J. Kippenberg, S. M. Spillane, and K. J. Vahala, "Ultra-high-Q toroid microcavity on a chip," *Nature* **421** (2003).
- [19] H. Lee, T. Chen, J. Li, K. Y. Yang, S. Jeon, O. Painter, and K. J. Vahala, "Chemically etched ultrahigh-q wedge-resonator on a silicon chip," *Nature Photonics* **6**, 369–373 (2012).
- [20] I. White, H. Oveys, and X. Fan, "Liquid-core optical ring-resonator sensors," *Optics Letters* **31**, 1319–1321 (2006).
- [21] M. S. Luchansky and R. C. Bailey, "High-q optical sensors for chemical and biological analysis," *Analytical Chemistry* **84**, 793–821 (2012).

- [22] H. Lee, T. Chen, J. Li, O. Painter, and K. J. Vahala, "Ultra-low-loss optical delay line on a silicon chip," *Nature Communications* **3**, 867– (2012).
- [23] M. Gorodetsky and V. Ilchenko, "High-q optical whispering-gallery microresonators - precession approach for spherical mode analysis and emission patterns with prism couplers," *Optics Communications* **113**, 133–143 (1994).
- [24] A. Serpenguzel, S. Arnold, and G. Griffel, "Excitation of resonances of microspheres on an optical-fiber," *Optics Letters* **20**, 654–656 (1995).
- [25] N. Dubreuil, J. Knight, D. Leventhal, V. Sandoghdar, J. Hare, and V. Lefevre, "Eroded monomode optical-fiber for whispering-gallery mode excitation in fused-silica microspheres," *Optics Letters* **20**, 813–815 (1995).
- [26] V. Ilchenko, X. Yao, and L. Maleki, "Pigtailing the high-Q microsphere cavity: a simple fiber coupler for optical whispering-gallery modes," *Optics Letters* **24**, 723–725 (1999).
- [27] B. Little, J. Laine, D. Lim, H. Haus, L. Kimerling, and S. Chu, "Pedestal antiresonant reflecting waveguides for robust coupling to microsphere resonators and for microphotonic circuits," *Optics Letters* **25**, 73–75 (2000).
- [28] C. E. Soteropoulos, H. K. Hunt, and A. M. Armani, "Determination of binding kinetics using whispering gallery mode microcavities," *Applied Physics Letters* **99**, 103703 (2011).
- [29] V. R. Dantham, S. Holler, V. Kolchenko, Z. Wan, and S. Arnold, "Taking whispering gallery-mode single virus detection and sizing to the limit," *Applied Physics Letters* **101**, 043704 (2012).
- [30] R. Boyd and J. Heebner, "Sensitive disk resonator photonic biosensor," *Applied Optics* **40**, 5742–5747 (2001).
- [31] A. T. Rosenberger, "Analysis of whispering-gallery microcavity-enhanced chemical absorption sensors," *Opt. Express* **15**, 12959–12964 (2007).
- [32] J. Zhu, S. K. Ozdemir, Y.-F. Xiao, L. Li, L. He, D.-R. Chen, and L. Yang, "On-chip single nanoparticle detection and sizing by mode splitting in an ultrahigh-q microresonator," *Nature Photonics* **4**, 46–49 (2009).
- [33] O. Gaathon, J. Culic-Viskota, M. Mihnev, I. Teraoka, and S. Arnold, "Enhancing sensitivity of a whispering gallery mode biosensor by subwavelength confinement," *Applied Physics Letters* **89**, 223901 – 1 (2006/11/27).

- [34] J. Yang and L. Guo, "Optical sensors based on active microcavities," *Selected Topics in Quantum Electronics, IEEE Journal of* **12**, 143–147 (2006).
- [35] L. He, ahin Kaya zdemir, J. Zhu, W. Kim, and L. Yang, "Detecting single viruses and nanoparticles using whispering gallery microlasers," *Nature Nanotechnology* **6**, 428–432 (2011).
- [36] M. A. Santiago-Cordoba, S. V. Boriskina, F. Vollmer, and M. C. Demirel, "Nanoparticle-based protein detection by optical shift of a resonant microcavity," *Applied Physics Letters* **99**, 073701 (2011).
- [37] J. D. Swaim, J. Knittel, and W. P. Bowen, "Detection limits in whispering gallery biosensors with plasmonic enhancement," *Appl. Phys. Lett.* **99**, 243109 (2011).
- [38] J. Knittel, T. G. McRae, K. H. Lee, and W. P. Bowen, "Interferometric detection of mode splitting for whispering gallery mode biosensors," *Applied Physics Letters* **97**, 123704 (2010).
- [39] T. Lu, H. Lee, T. Chen, S. Herchak, J.-H. Kim, S. E. Fraser, R. C. Flagan, and K. Vahala, "High sensitivity nanoparticle detection using optical microcavities," *Proceedings of the National Academy of Sciences* (2011).
- [40] A. M. Armani, R. P. Kulkarni, S. E. Fraser, R. C. Flagan, and K. J. Vahala, "Label-free, single-molecule detection with optical microcavities," *Science* **317**, 783–787 (2007).
- [41] S. Arnold, S. Shopova, and S. Holler, "Whispering gallery mode bio-sensor for label-free detection of single molecules: Thermo-optic vs. reactive mechanism," *Optics Express* **18**, 281 – 287 (2010).
- [42] X. Lopez-Yglesias, J. M. Gamba, and R. C. Flagan, "The physics of extreme sensitivity in whispering gallery mode optical biosensors," *Journal of Applied Physics* **111**, 084701 (2012).
- [43] F. Vollmer, S. Arnold, and D. Keng, "Single virus detection from the reactive shift of a whispering-gallery mode," *Proceedings of the National Academy of Sciences* **105**, 20701–20704 (2008).
- [44] V. R. Dantham, S. Holler, C. Barbre, D. Keng, V. Kolchenko, and S. Arnold, "Label-free detection of single protein using a nanoplasmonic-photonic hybrid microcavity," *Nano Letters* **0**, null (0).
- [45] A. Oraevsky, "Whispering-gallery waves," *Quantum Electronics* **32**, 377–400 (2002).

- [46] I. M. White and X. Fan, "On the performance quantification of resonant refractive index sensors," *Opt. Express* **16**, 1020–1028 (2008).
- [47] J. Hu, X. Sun, A. Agarwal, and L. C. Kimerling, "Design guidelines for optical resonator biochemical sensors," *J. Opt. Soc. Am. B* **26**, 1032–1041 (2009).
- [48] F. Vollmer and S. Arnold, "Whispering-gallery-mode biosensing: label-free detection down to single molecules," *Nature Methods* **5**, 591–596 (2008).
- [49] T. Yoshie, L. Tang, and S.-Y. Su, "Optical microcavity: Sensing down to single molecules and atoms," *Sensors* **11**, 1972–1991 (2011).
- [50] M. I. Cheema and A. G. Kirk, "Application of ring down measurement approach to micro-cavities for bio-sensing applications," in "Proc. SPIE 7888, 788808," (2011).
- [51] M. I. Cheema, S. Mehrabani, A. A. Hayat, Y.-A. Peter, A. M. Armani, and A. G. Kirk, "Experimental demonstration of application of ring-down measurement approach to microcavities for biosensing," in "Proc. SPIE BIOS 82120B-82120B-6," (2012).
- [52] M. I. Cheema and A. G. Kirk, "Mathematical treatment of a cavity coupled with a waveguide for the phase shift-cavity ring down spectroscopy measurements," (*Journal paper under preparation*, 2013).
- [53] M. I. Cheema and A. G. Kirk, "Implementation of the perfectly matched layer to determine the quality factor of axisymmetric resonators in COMSOL," in "COMSOL conference, Boston (2010)," (2010).
- [54] M. I. Cheema and A. G. Kirk, "Accurate determination of the quality factor and tunneling distance of axisymmetric resonators for biosensing applications," *Opt. Express* **21**, 8724–8735 (2013).
- [55] M. I. Cheema, U. A. Khan, A. M. Armani, and A. G. Kirk, "Application of phase shift ring down spectroscopy to microcavities for biosensing," in "Proc. SPIE BIOS 859401-859401-6," (2013).
- [56] M. I. Cheema, C. Shi, A. M. Armani, and A. G. Kirk, "Optimizing the signal to noise ratio of microcavity sensors," (*Submitted to a journal*, 2013).
- [57] M. I. Cheema, U. A. Khan, A. M. Armani, and A. G. Kirk, "Towards more accurate microcavity sensors: maximum likelihood estimation applied to a combination of quality factor and wavelength shifts," (*Submitted to a journal*, 2013).
- [58] B. Little, J. P. Laine, and H. Haus, "Analytic theory of coupling from tapered fibers and half-blocks into microsphere resonators," *Lightwave Technology, Journal of* **17**, 704–715 (1999).

- [59] B. Min, "Ultrahigh-q microtoroid on-chip resonators for low threshold microlasers," Ph.D. thesis, CALTECH (2006).
- [60] B. Min, L. Yang, and K. Vahala, "Perturbative analytic theory of an ultrahigh- q toroidal microcavity," Phys. Rev. A **76**, 013823 (2007).
- [61] Rayleigh, L, "The problem of the whispering gallery," Philosophical Magazine **20**, 1001–1004 (1910).
- [62] J. D. Jackson, *Classical Electrodynamics* (John Wiley, 1998), 3rd ed.
- [63] R. Engeln, G. VonHelden, G. Berden, and G. Meijer, "Phase shift cavity ring down absorption spectroscopy," Chemical Physics Letters **262**, 105–109 (1996).
- [64] E. G. Berden and R. Engeln, *Cavity Ring-Down Spectroscopy: Techniques and Applications* (Wiley, 2009).
- [65] "About Lock-In Amplifiers," <http://www.thinksrs.com/downloads/PDFs/ApplicationNotes/AboutLIAs.pdf>. Accessed: June 15, 2013.
- [66] T. Kippenberg, "Nonlinear optics in ultra-high-q whispering-gallery optical microcavities," Ph.D. thesis, CALTECH (2004).
- [67] J. P. Rezac, "Properties and applications of whispering gallery mode resonances in fused silica microspheres," Ph.D. thesis, Oklahoma State University (2002).
- [68] J. Barnes, B. Carver, J. M. Fraser, G. Gagliardi, H. P. Loock, Z. Tian, M. W. B. Wilson, S. Yam, and O. Yastrubshak, "Loss determination in microsphere resonators by phase-shift cavity ring-down measurements," Optics Express **16**, 13158–13167 (2008).
- [69] H. A. Haus, *Waves and fields in Optoelectronics* (Prentice-Hall Inc., 1984).
- [70] S. M. Spillane, T. J. Kippenberg, O. J. Painter, and K. J. Vahala, "Ideality in a fiber-taper-coupled microresonator system for application to cavity quantum electrodynamics," Phys. Rev. Lett. **91**, 043902 (2003).
- [71] S. Spillane, "Fiber-coupled ultra-high-q microresonators for nonlinear and quantum optics," Ph.D. thesis, CALTECH (2004).
- [72] A. L. Washburn and R. C. Bailey, "Photonics-on-a-chip: recent advances in integrated waveguides as enabling detection elements for real-world, lab-on-a-chip biosensing applications," The Analyst **136**, 227 (2011).
- [73] J. L. Nadeau, V. S. Ilchenko, D. Kossakovski, G. H. Bearman, and L. Maleki, "High- q whispering-gallery mode sensor in liquids," Proc. SPIE **4629**, 172–180 (2002).

- [74] D. Anderson, J. Frisch, and C. Masser, “Mirror reflectometer based on optical cavity decay time,” *Applied Optics* **23**, 1238–1245 (1984).
- [75] A. Okeefe and D. Deacon, “Cavity ring-down optical spectrometer for absorption-measurements using pulsed laser sources,” *Review of Scientific Instruments* **59**, 2544–2551 (1988).
- [76] K. K. Lehmann and H. Huang, *Frontiers of Molecular Spectroscopy* (Elsevier, 2009), chap. Optimal Signal Processing in Cavity Ring-Down Spectroscopy, pp. 623–658.
- [77] J. M. Herbelin, J. A. McKay, M. A. Kwok, R. H. Ueunten, D. S. Urevig, D. J. Spencer, and D. J. Benard, “Sensitive measurement of photon lifetime and true reflectances in an optical cavity by a phase-shift method,” *Appl. Opt.* **19**, 144–147 (1980).
- [78] L. van der Sneppen, “Liquid-phase cavity ring-down spectroscopy for improved analytical detection sensitivity,” Ph.D. thesis, Vrije University, Amsterdam (2008).
- [79] T. Peter and L. Kevin, *Optical Biosensors: Today and Tomorrow* (Elsevier B.V, 2008), chap. Cavity ring Down biosensing, pp. 403–418.
- [80] P. Tarsa, A. Wist, P. Rabinowitz, and K. Lehmann, “Single-cell detection by cavity ring-down spectroscopy,” *Applied Physics Letters* **85**, 4523–4525 (2004).
- [81] Z. Tong, A. Wright, T. McCormick, R. Li, R. D. Oleschuk, and H.-P. Loock, “Phase-shift fiber-loop ring-down spectroscopy,” *Analytical Chemistry* **76**, 6594–6599 (2004). PMID: 15538782.
- [82] R. W. P. Drever, J. L. Hall, F. V. Kowalski, J. Hough, G. M. Ford, A. J. Munley, and H. Ward, “Laser phase and frequency stabilization using an optical resonator,” *Applied Physics B Photophysics And Laser Chemistry* **31**, 97–105 (1983).
- [83] A. Schliesser and T. J. Kippenberg, *Advances in Atomic Molecular and Optical Physics* (Elsevier Inc., 2010), vol. 58, chap. Chapter 5 Cavity Optomechanics with Whispering-Gallery Mode Optical Micro-Resonators, pp. 207–323.
- [84] J. C. Knight, G. Cheung, F. Jacques, and T. A. Birks, “Phase-matched excitation of whispering-gallery-mode resonances by a fiber taper,” *Opt. Lett.* **22**, 1129–1131 (1997).
- [85] V. S. Ilchenko and M. L. Gorodetskii, “Thermal nonlinear effects in optical whispering gallery microresonators,” *Laser Physics* **2**, 1004–1009 (1992).
- [86] S. Zhao and W. M. Reichert, “Influence of biotin lipid surface density and accessibility on avidin binding to the tip of an optical fiber sensor,” *Langmuir* **8**, 2785–2791 (1992).

- [87] K. L. Snyder and R. N. Zare, "Cavity ring-down spectroscopy as a detector for liquid chromatography," *Analytical Chemistry* **75**, 3086–3091 (2003).
- [88] B. Bahnev, L. van der Sneeppen, A. E. Wiskerke, F. Ariese, C. Gooijer, and W. Ubachs, "Miniaturized cavity ring-down detection in a liquid flow cell," *Analytical Chemistry* **77**, 1188–1191 (2005).
- [89] C. Spielmann, R. Szipöcs, A. Stingl, and F. Krausz, "Tunneling of optical pulses through photonic band gaps," *Phys. Rev. Lett.* **73**, 2308–2311 (1994).
- [90] P. Pereyra, "Closed formulas for tunneling time in superlattices," *Phys. Rev. Lett.* **84**, 1772–1775 (2000).
- [91] V. A. Podolskiy and E. E. Narimanov, "Chaos-assisted tunneling in dielectric microcavities," *Opt. Lett.* **30**, 474–476 (2005).
- [92] M. Tomes, K. J. Vahala, and T. Carmon, "Direct imaging of tunneling from a potential well," *Opt. Express* **17**, 19160–19165 (2009).
- [93] O. Chinellato, P. Arbenz, M. Streiff, and A. Witzig, "Computation of optical modes in axisymmetric open cavity resonators," *Future Generation Computer Systems* **21**, 1263 – 1274 (2005).
- [94] M. Karl, B. Kettner, S. Burger, F. Schmidt, H. Kalt, and M. Hetterich, "Dependencies of micro-pillar cavity quality factors calculated with finite element methods," *Opt. Express* **17**, 1144–1158 (2009).
- [95] M. Koshiba, K. Hayata, and M. Suzuki, "Improved finite-element formulation in terms of the magnetic field vector for dielectric waveguides," *Microwave Theory and Techniques, IEEE Transactions on* **33**, 227–233 (1985).
- [96] R. Osegueda, J. Pierluissi, L. Gil, A. Revilla, G. Villalva, G. Dick, D. Santiago, and R. Wang, "Azimuthally-dependent finite element solution to the cylindrical resonator," in "10th annual review of progress in applied computational electromagnetics, conference proceedings, vol 1," , Terzuoli, A, ed., Appl Comp Electromagnet Soc (1994 A C E S Conference, , 1994), pp. 159–170. .
- [97] M. Soltani, Q. Li, S. Yegnanarayanan, and A. Adibi, "Toward ultimate miniaturization of high q silicon traveling-wave microresonators," *Opt. Express* **18**, 19541–19557 (2010).
- [98] <https://sites.google.com/site/axisymmetricmarkoxborrow/home>. Accessed: June 27, 2013.

- [99] M. Oxborrow, J. D. Breeze, and N. M. Alford, “Room-temperature solid-state maser,” *Nature* **488**, 353–356 (2012).
- [100] C. Shi, H. S. Choi, and A. M. Armani, “Optical microcavities with a thiol-functionalized gold nanoparticle polymer thin film coating,” *Applied Physics Letters* **100**, 013305 (2012).
- [101] Y.-F. Xiao, C.-L. Zou, B.-B. Li, Y. Li, C.-H. Dong, Z.-F. Han, and Q. Gong, “High- q exterior whispering-gallery modes in a metal-coated microresonator,” *Phys. Rev. Lett.* **105**, 153902 (2010).
- [102] A. Arbabi, Y. M. Kang, and L. L. Goddard, “Analysis and Design of a Microring Inline Single Wavelength Reflector,” in “FIO,” (2010).
- [103] F. Teixeira and W. Chew, “Systematic derivation of anisotropic pml absorbing media in cylindrical and spherical coordinates,” *Microwave and Guided Wave Letters, IEEE* **7**, 371–373 (1997).
- [104] V. Datsyuk, “Some characteristics of resonant electromagnetic modes in a dielectric sphere,” *Applied Physics B* **54**, 184–187 (1992).
- [105] L. A. Weinstein, *Open Resonators and Open Waveguides* (The Golem Press, Boulder, Colorado, USA, 1969).
- [106] J. R. Buck and H. J. Kimble, “Optimal sizes of dielectric microspheres for cavity qed with strong coupling,” *Phys. Rev. A* **67**, 033806 (2003).
- [107] B. R. Johnson, “Theory of morphology-dependent resonances: shape resonances and width formulas,” *J. Opt. Soc. Am. A* **10**, 343–352 (1993).
- [108] S. Scheurich, S. Belle, R. Hellmann, S. So, I. Sparrow, and G. Emmerson, “Application of a silica-on-silicon planar optical waveguide Bragg grating sensor for organic liquid compound detection,” in “Proc. SPIE 7356,” (2009).
- [109] M. Gallignani, S. Garrigues, and M. de la Guardia, “Direct determination of ethanol in all types of alcoholic beverages by near-infrared derivative spectrometry,” *Analyst* **118**, 1167–1173 (1993).
- [110] A. Quarteroni and A. Valli, *Numerical Approximation of Partial Differential Equations* (Springer, 1997).
- [111] V. S. Ilchenko, A. A. Savchenkov, A. B. Matsko, and L. Maleki, “Dispersion compensation in whispering-gallery modes,” *J. Opt. Soc. Am. A* **20**, 157–162 (2003).

- [112] A. Armani, D. Armani, B. Min, K. Vahala, and S. Spillane, “Ultra-high-Q microcavity operation in H₂O and D₂O,” *Applied Physics Letters* **87** (2005).
- [113] “Our COMSOL model,” http://www.ece.mcgill.ca/~mcheem2/cheema_res.html. Accessed: June 27, 2013.
- [114] H. K. Hunt and A. M. Armani, “Label-free biological and chemical sensors,” *Nanoscale* **2**, 1544–1559 (2010).
- [115] D. Pinnow, T. Rich, Ostermay.FW, and Didomeni.M, “Fundamental optical attenuation limits in liquid and glassy state with application to fiber optical waveguide materials,” *Applied Physics Letters* **22**, 527–529 (1973).
- [116] M. L. Gorodetsky, A. A. Savchenkov, and V. S. Ilchenko, “Ultimate q of optical microsphere resonators,” *Opt. Lett.* **21**, 453–455 (1996).
- [117] W. M. Haynes, *CRC Handbook of Chemistry and Physics* (2012), 93rd ed.
- [118] A. Yariv, *Optical Electronics in Modern Communications* (Oxford University Press, 1999), 5th ed.
- [119] “Newport, TLB-6700 laser,” http://assets.newport.com/webDocuments-EN/images/TLB6700_User_Manual.pdf. Accessed: May 31, 2013.
- [120] B. P. Lathi, *Modern Digital and Analog Communication Systems* (Oxford University Press, 1998), 3rd ed.
- [121] T. Carmon, L. Yang, and K. Vahala, “Dynamical thermal behavior and thermal self-stability of microcavities,” *Opt. Express* **12**, 4742–4750 (2004).
- [122] J. R. Taylor, *An Introduction to Error Analysis: The Study of Uncertainties in Physical Measurements* (University Science Books, 1996).
- [123] L. L. Scharf, *Statistical Signal Processing: Detection, Estimation, and Time Series Analysis* (Addison-Wesley, 1991).
- [124] N. Hanumegowda, C. Stica, B. Patel, I. White, and X. Fan, “Refractometric sensors based on microsphere resonators,” *Applied Physics Letters* **87** (2005).
- [125] M. I. Cheema, “Application of cavity ring down spectroscopy to microcavities for biosensing,” Ph.D. thesis, McGill University (2013). (To be published).
- [126] S. Arnold, M. Khoshshima, I. Teraoka, S. Holler, and F. Vollmer, “Shift of whispering-gallery modes in microspheres by protein adsorption,” *Opt. Lett.* **28**, 272–274 (2003).

- [127] J. Homola, I. Koudela, and S. S. Yee, "Surface plasmon resonance sensors based on diffraction gratings and prism couplers: sensitivity comparison," *Sensors and Actuators B: Chemical* **54**, 16 – 24 (1999).
- [128] W. D. Sacher and J. K. S. Poon, "Dynamics of microring resonator modulators," *Opt. Express* **16**, 15741–15753 (2008).
- [129] E. Hamers, D. Schram, and R. Engeln, "Fourier transform phase shift cavity ring down spectroscopy," *Chemical Physics Letters* **365**, 237 – 243 (2002).